論文 / 著書情報
Article / Book Information

題目(和文)	Nd、Pr、DyおよびTb削減のためのNd-Fe-B焼結磁石における粒界相の微細構造設計
Title(English)	Microstructural design of grain boundary phases in Nd-Fe-B sintered magnets for Nd, Pr, Dy and Tb reduction
著者(和文)	榎戸靖
Author(English)	Yasushi Enokido
出典(和文)	学位:博士(工学), 学位授与機関:東京工業大学, 報告番号:甲第11987号, 授与年月日:2021年3月26日, 学位の種別:課程博士, 審査員:北本 仁孝,細田 秀樹,曽根 正人,三宮 工,進士 忠彦,杉本 諭
Citation(English)	Degree:Doctor (Engineering), Conferring organization: Tokyo Institute of Technology, Report number:甲第11987号, Conferred date:2021/3/26, Degree Type:Course doctor, Examiner:,,,,,
学位種別(和文)	博士論文
Type(English)	Doctoral Thesis

Microstructural design of grain boundary phases in Nd-Fe-B sintered magnets for Nd, Pr, Dy and Tb reduction

Yasushi ENOKIDO

Supervised by

Professor Yoshitaka KITAMOTO

Department of Materials Science and Engineering

School of Materials and Chemical Technology

Tokyo Institute of Technology

March 2021

Contents

Chapter 1 General introduction

1.1 Nd-Fe-B magnet industry

This section describes the origins of the Nd-Fe-B magnet industry. The path to the discovery of Nd-Fe-B magnets and the Nd-Fe-B sintered magnet industry that emerged from it are described.

1.1.1 Discovery of Nd-Fe-B magnet

The existence of magnets is said to have been known since the time of ancient Greece. During the Age of Discovery, which began around the 13th century, the importance of compasses increased in Western Europe as well, where they were used in large numbers. The scientific analysis of these compasses was carried out by William Gilbert in England around the 15th century. Magnetite was used as the magnet for these magnets, which were never very powerful.

At the beginning of the 20th century, research into the synthesis and application of magnets was undertaken. In 1917, Kotaro Honda of Tohoku University invented KS steel (Fe-Co-W-Cr). Following this, Tokushichi Mishima of the University of Tokyo invented MK steel (Fe-Ni-Al) with high coercivity in 1932, and in 1934, Kotaro Honda invented NKS steel by adding Co-Ti to MK steel. Furthermore, in 1938, General Electric Company developed an alnico magnet with Cu added to NKS steel. On the other hand, in 1930, at the Tokyo Institute of Technology, Takeshi Takei and Yogoro Kato invented ferrite magnets [1], which were completely different from the conventional metal magnets and were made from oxides.

In the 1960s, the $SmCo_5$ magnet was developed in the U.S. on the background of research on the electron arrangement and spin magnetic moment such as Hund's law. Here, rare earth elements with a magnetic moment of 4f unpaired electrons came to be used in the magnets and they are called rare earth magnets. This was the beginning of permanent magnets using the force of single ion anisotropy possessed by rare earth elements, which will be described later, and also the beginning of mass use of rare earth elements.

In 1974, Yoshio Tawara et al. [2] developed Sm_2Co_{17} magnets with higher coercivity, which were widely used in motors and other applications due to their high coercivity, and magnet manufacturers accelerated the development of Sm_2Co_{17} magnets to achieve higher characteristics [3]. In such a situation, TDK corporation discovered high coercivity by Zr addition, and the high performance of SmCo magnets reached its peak [4].

In the early 1980s, powerful magnets with the same composition were created in different places: one as a magnet powder and another as a sintered magnet.

The former was developed by John Croat and his colleagues at General Motors Company in the USA [5], [6]. The former was an isotropic magnetic powder made of pulverized ribbons made by the melt-spin method. This magnet powder is mixed with a resin and used as a so-called bond magnet. The other was developed by Masato Sagawa et al. in Japan and was an anisotropic sintered magnet [7]–[10]. Both of them were based on the composition of $Nd_2Fe_{14}B$. In particular, the magnetic properties of the sintered magnet exceeded those of Sm_2Co_{17}, which revolutionized the world of permanent magnets. These magnets are called neodymium magnets or Nd-Fe-B magnets, and no bulk magnet has ever been developed to date that exceeds these two types of magnets. The history of the discovery of magnets and their improved magnetic properties of commercial magnet product is shown in Figure 1-1.

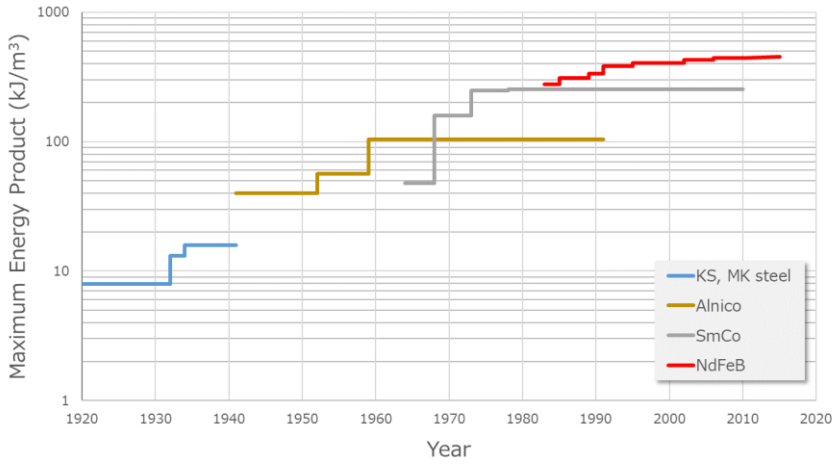

Figure 1-1 The history of the discovery of magnets and their improved magnetic properties.

Nd-Fe-B magnets have been widely used since the 1990s as voice coil motors (VCM) for hard disk drives (HDD) and motors, and their use in energy-saving home appliances accelerated from the late 1990s to the 2000s, with automotive applications such as electric power steering (EPS) expanding in the mid-2000s. Especially since 2010, its use in motor and generator applications for xEVs, which means a generic term of HEV (hybrid electric vehicle), BEV (battery electric vehicle), PHEV (plug-in hybrid electric vehicle) and FCEV (fuel cell electric vehicle), has been increasing rapidly. Furthermore, in the recent trend of autonomous driving of automobiles, the equipment which has been hydraulically controlled until now is being changed to be electrically controlled. This has increased the use of Nd-Fe-B magnets. Nd-Fe-B magnets are indispensable in our daily lives and support the social infrastructure.

1.1.2 Sintered Nd-Fe-B magnet

The current global production of Nd-Fe-B sintered magnets is thought to exceed 100,000 ton, with production increasing every year, partly due to the rapid increase in demand for xEV applications. Under these circumstances, high efficiency is required in the manufacturing method of Nd-Fe-B magnets. A method for manufacturing Nd-Fe-B sintered magnets is described below. The manufacturing process differs from one manufacturer to another and is not necessarily the same, the typical process flow is shown Figure 1-2 as a flowchart.

Figure 1-2 Typical Nd-Fe-B magnet manufacturing process.

Alloy

The first step is to prepare an alloy with approximately the same composition as the final magnet product. Raw metals were heated in a crucible to make metal melting. In general, the composition of Nd-Fe-B magnets is Nd-richer than the stoichiometric composition of $Nd_2Fe_{14}B$, and a small amount of Cu and other elements such as Co, Al, and Zn are added. This is because the formation of Nd-Fe or Nd-Fe-Cu, which has a lower melting point than $Nd_2Fe_{14}B$, enables liquid

phase sintering and provides a high-density sintered body at a relatively low temperature. These Nd-Fe or Nd-Fe-Cu phases are called Nd-rich or R-rich phase. In addition, as described later, the R-rich grain boundary phase has a great influence on the coercivity development of the magnet.

In the past, bookmolding and other methods were used to fabricate alloys, however nowadays the strip-cast (SC) method is mainly used [11]. A SC alloy of several hundred μm in thickness is produced by pouring molten raw material solution through a rotating copper roll. When the melt comes into contact with the copper rolls, it begins to solidify and becomes an alloy with dendrite crystal growth on the roll surface. A typical cross-sectional picture of the SC alloy is shown in Figure 1-3. The bottom surface of the figure is the roll contact surface. The gray area in the figure is the dendrite crystal of $Nd_2Fe_{14}B$ and the white area is the so-called R-rich phase, i.e., the phase based on Nd-Fe.

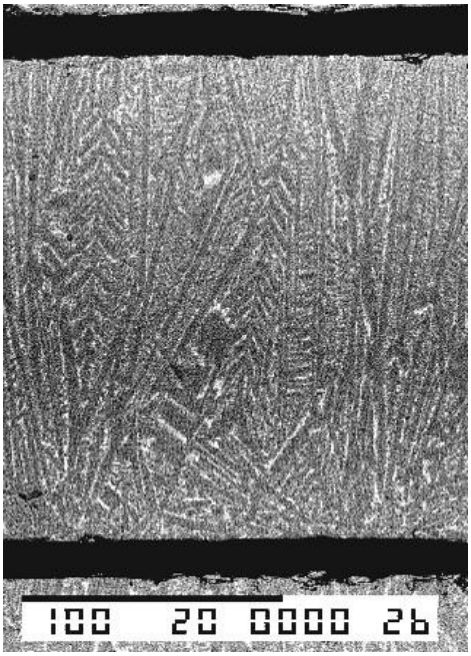

Figure 1-3 Cross section of typical SC alloy.

Pulverization

The alloy is ground to a fine powder by two-step milling. The purpose of pulverization is to extract the anisotropic powder. For this purpose, it is necessary to mill to the same size as or even smaller than the diameter of dendrite crystals.

The first process is crushing by hydrogen absorption, because rare earth elements including Nd are highly hydrogen-absorbing; therefore, the Nd-rich phase absorbs more hydrogen and expands than the $Nd_2Fe_{14}B$ phase and cracks are introduced. This results in a hard and brittle state for a metal. This process is called rough milling.

The second process is dry milling, called jet milling. The powder is introduced into the jet stream and the grinding proceeds by the collision of powder with each other. The milled powder is classified by a classifying rotor to obtain a fine powder with a small particle size distribution. In this process, a small amount of lubricant is added to prevent the powder from being fused with each other by collision [12]. This lubricant has the effect of promoting the rotation of each particle when the magnetic field is aligned in pressing process, but it is also a source of residual carbon which is an impurity. The size of magnet powder used in the mass production of magnets is approximately 3-5 μm. These grinding processes are carried out in an inert gas atmosphere. This is because rare earth elements are highly active and easily oxidized. Oxidation results in the formation of neodymium oxide, which reduces the relative amount of $Nd_2Fe_{14}B$ phase that can be formed, leading to a decrease in magnetization. This process is called fine milling.

Press-Molding

A magnetic field molding method is used to form magnets. This is done by forming fine particles, each of which is anisotropic, in the same direction to produce

an anisotropic magnet with strong magnetization in one direction. For this purpose, a die is filled with fine powder and pressed under uniaxial pressure with a magnetic field applied. After molding, an appropriate reverse magnetic field is applied to the molded product before it is punched out of the die to remove the magnetization of the molded compacts. If this reverse magnetic field is not applied, the molded compacts, which are magnetized, will collide violently with each other and be broken.

In general, there are two types of magnetic field molding methods depending on the direction of the magnetic field applied [10]. One is to apply the magnetic field in the same direction as the uniaxial pressing direction, which is called as axial pressing, and the other is to apply it perpendicularly, which is called as transverse pressing. When the magnetic field is applied in the same direction, the orientation of the powder is easily disturbed by the pressure, and the magnetization tends to decrease. For this reason, perpendicular magnetization is usually applied to form high-performance magnets. However, depending on the shape of the magnet and the desired orientation direction, the application of parallel magnetization may be applied.

Heat-treating

The molded magnets are fired by a continuous or batch furnace. Sintering in a vacuum is commonly used to achieve high density, and the material is heat treated at 1000-1100°C for several hours and then quenched. It is then subjected to a two-step annealing process, which increases the coercivity of the magnet. The heat treatment temperatures are 800-900°C and 500-600°C, respectively.

Grinding and surface treatment

In general, all magnets are machined and polished. For example, in motors, magnets are used in close contact with the rotor core, and reducing the gap is important for effective use of the magnetic flux. A combination of wire cutting, blade cutting, surface grinding, and curved surface grinding techniques are used to process and polish the magnets to obtain the desired shape. The required dimensional accuracy varies from product to product, but in some cases a narrow tolerance of ± 0.05 mm is required. Since Nd-Fe-B magnets tend to rust easily under high humidity and high temperature conditions, surface treatment is sometimes applied. Surface treatment includes passivation treatment, resin coating and plating film treatment.

The ideal microstructural changes during these processes are briefly summarized in Figure 1-4. The Nd-Fe-B magnet alloy is a group of $Nd_2Fe_{14}B$ columnar crystals as illustrated in Figure 1-4 (a), and each columnar crystal is a single crystal. The R-rich phase exists between the columnar crystals. The alloy is pulverized to a size of a columnar crystal diameter to obtain a fine powder of a $Nd_2Fe_{14}B$ single crystal as illustrated in Figure 1-4 (b). The R-rich phase is attached to the fine powder. When this is molded and heat-treated, the $Nd_2Fe_{14}B$ grain is grown and densified by liquid phase sintering to obtain a polycrystalline ceramic. In this thesis, a region between two main phase grains is called a grain boundary, which is often referred to as intergranular grain boundary in the magnet community, and a region surrounded by three or more main phase grains is called a triple junction. During liquid phase sintering, the R-rich grain boundary phase was excluded at the triple junction as illustrated in Figure 1-4 (c). By subsequent annealing, the R-rich phase at triple junction is once transformed into a liquid phase and returned to the grain boundary by capillary force as illustrated in Figure 1-4 (d). As a result, it is ideal that the $Nd_2Fe_{14}B$ single crystal grains have a crystal structure separated by the R-

rich grain boundary phase. The direction of the arrow indicates the easy axis direction of magnetization of the $Nd_2Fe_{14}B$ crystal. It is important from the viewpoint of obtaining high magnetization to perform molding and heat treatment while aligning the easy magnetization axis of the primary particles and finally align the easy magnetization axis in the same direction as the sintered body.

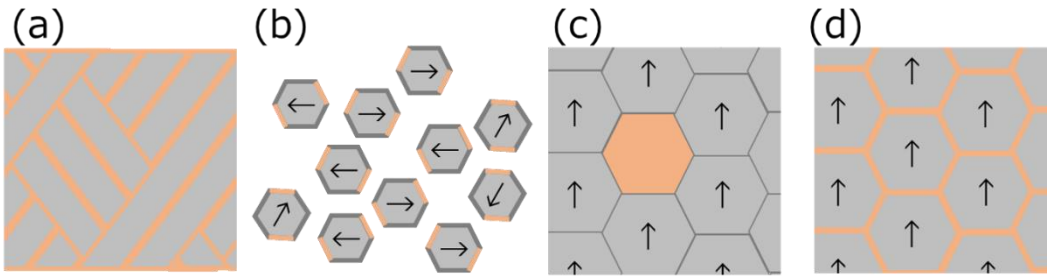

Figure 1-4 Ideal microstructure evolution process; a) dendrite structure of alloy, b) fine powder, c) liquid phase sintered body, d) sintered body after annealing.

1.2 Origin of hard magnetic properties in Nd-Fe-B magnet

The magnetic properties most required for a magnet are residual flux density (B_r) and coercivity (H_{cJ}). The relationship between the hysteresis loop and the residual flux density and coercivity of the magnet is shown in Figure 1-5. Other properties include maximum energy product, angular ratio, temperature characteristics, and initial magnetization behavior, etc. The principles of these two are briefly discussed in this section.

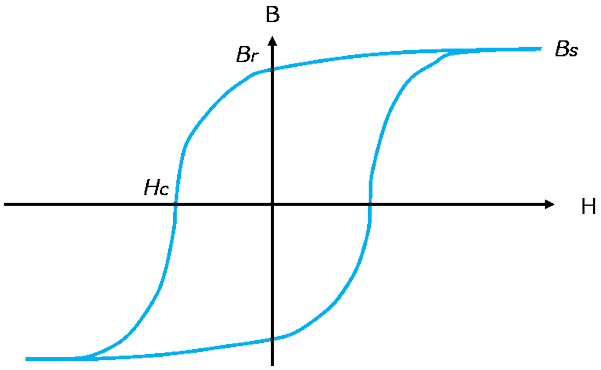

Figure 1-5 Typical hysteresis loop.

1.2.1 Magnetization

The magnetization of $Nd_2Fe_{14}B$ is determined by the sum of the magnetization of iron, a representative ferromagnetic transition metal, and Nd (very often Pr is also used) ions, a rare earth element, present in its crystal structure. The crystal structure of $Nd_2Fe_{14}B$ is shown in Figure 1-6. The magnetization of iron is due to the spin magnetic moment of 3d electron orbitals, and Nd is due to 4f electron orbitals.

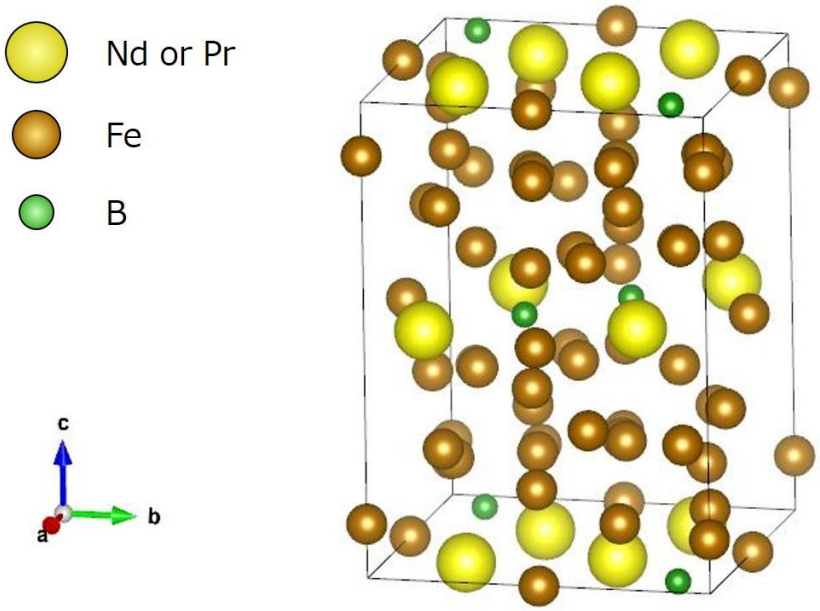

Figure 1-6 Crystal structure of $Nd_2Fe_{14}B$.

Here, many other rare earth elements can be substituted at the Nd site. The magnetization of $R_2Fe_{14}B$, where R stands for rare earth elements, has been studied using various rare earth elements [7], [9], [13], [14]. These are summarized in Table 1-1 together with other properties described later.

Table 1-1 Magnetic properties of $R_2Fe_{14}B$ with various rare earth element.

	Saturation magnetization *Is* (T)	**Curie temperature Tc (K)**	**Anisotropy constant *K* (MJ/m^3)**	**Anisotropy field H_A (MA/m)**
$Y_2Fe_{14}B$	1.42	571	1.41	1.59
$Ce_2Fe_{14}B$	1.17	422	1.76	2.39
$Pr_2Fe_{14}B$	1.56	569	6.79	6.93
$Nd_2Fe_{14}B$	1.60	586	5.36	5.33
$Sm_2Fe_{14}B$	1.52	620	plane	-
$Gd_2Fe_{14}B$	0.89	659	1.12	2.00
$Tb_2Fe_{14}B$	0.70	620	7.73	17.51
$Dy_2Fe_{14}B$	0.71	598	5.34	11.94
$Ho_2Fe_{14}B$	0.80	5733	3.03	5.97
$Er_2Fe_{14}B$	0.90	551	plane	-
$Tm_2Fe_{14}B$	0.93	549	plane	-
$Lu_2Fe_{14}B$	1.18	535	plane	-

In an actual magnet, how large the residual flux density is important. In addition, actual magnets are often polycrystalline rather than monocrystalline, and the amount of magnetization is determined by their microstructure and other factors. This can be expressed in terms of the following equation.

$$B_r = 4\pi \cdot M_S \cdot V_m \cdot \rho \cdot f$$

where M_s is the saturation magnetization, V_m is the volume ratio of the main phase to the total, ρ is the relative density, and f is the orientation. The saturation magnetization is a composition-dependent intrinsic property as shown in Table 1-1, while the others are extrinsic properties such as microstructure. In order to obtain a higher residual flux density, it is necessary not only to select rare earth elements

with a higher *Ms*, but also to increase the ratio of the main phase by decreasing grain boundary components and impurities, to increase the density by sintering sufficiently, and to maintain high orientation of each particle after sintering by orienting them sufficiently.

The microstructure of a Nd-Fe-B magnet is illustrated in Figure 1-7. The main phase represents each crystalline particle (grain) of $Nd_2Fe_{14}B$, and these particles are surrounded by a grain boundary phase called Nd-rich phase or R-rich grain boundary phase. At the triple junction, there are B-rich, oxide and carbide phases as unavoidable impurities, and pores are also present. The elimination of these impurities contributes to the improvement of Vm, and the elimination of pores contributes to the improvement of ρ. If the easy axes of magnetization of all the main phases (grains) are aligned in the same direction (f=1.0), the magnet exhibits the strongest magnetization in that direction. Such a magnet is called an anisotropic magnet. A magnet in which the easy axis of magnetization is oriented in a random direction (f=0.5) is called an isotropic magnet.

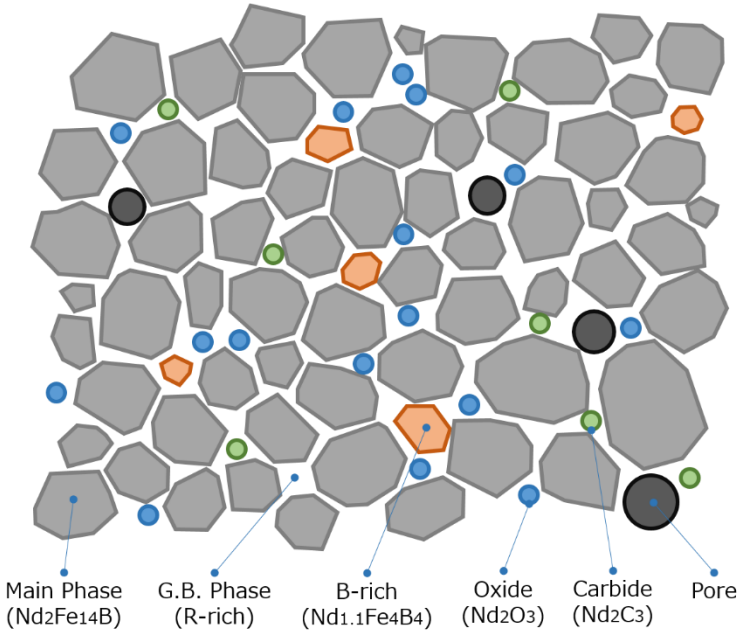

Figure 1-7 Schematic of Nd-Fe-B magnet microstructure.

The maximum residual flux density obtained in the Nd-Fe-B magnet reported is 1.555 T [15], which is about 97% of the saturation magnetization. Even in commercial magnets, magnets having a residual flux density of about 1.45 T are sold, and it is not rare that the residual flux density exceeds 90% of the saturation magnetization. In other words, the intrinsic properties of the material are almost fully exhibited, and there is little room to extrinsically improve it.

1.2.2 Coercivity

In rare earth magnets, the magnetic anisotropy of rare earth ions is the source of their coercivity [16], which is why rare earth elements have always been used in the strongest magnets since the discovery of SmCo magnets. As mentioned above, it is the electrons of the 4f-shell that are responsible for the magnetism of rare earth ions. The spatial distribution of the charge density is not a spherical

object, but rather it has a distorted shape. The shape of the 4f-shell electron density of trivalent rare earth ions is shown in Figure 1-8 [14].

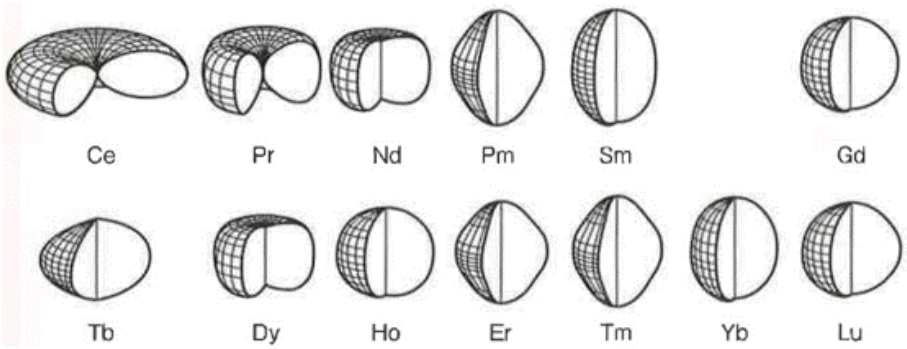

Figure 1-8 Shape of the 4f-shell electron density of trivalent rare earth ions [14].

The magnetic moment is united with the anisotropically spread electron cloud, which is the cause of the magnetic anisotropy. This is known as single ion anisotropy. This charge distribution interacts with the charges of neighboring atoms and ions in the crystal, making the orbitals of the 4f-shell electrons more likely to be oriented in a particular direction in the crystal lattice. This leads to the crystal magnetic anisotropy as a crystal. Uniaxial magnetocrystalline anisotropy is expressed by the angular dependence of the internal energy of the crystal on the direction of magnetization as follows (For simplicity, the higher order terms are ignored here.).

$$E_A = K_1 \sin^2 \theta$$

where E_A is the internal energy and K_1 is the magnetic anisotropy constant. On the other hand, the anisotropy field (H_A) is shown by the following equation.

$$H_A = 2K_1/M_S$$

where M_S is the magnetization. The anisotropy field expresses the strength of the magnetic field required to reverse the direction of magnetization, and is measured as the strength of the magnetic field that exhibits the same magnetization (saturation magnetization) when the anisotropic magnet is magnetized along the hard axis of magnetization and when it is magnetized along the easy axis of magnetization.

The coercivity is expressed as follows [14], [17].

$$H_C = \alpha \cdot H_A - N_{eff} \cdot I_S$$

Where α is a constant and N_{eff} is the effective demagnetizing coefficient including the reduction of the magnetic field due to the demagnetizing field of the magnetic particles themselves and the leakage field generated by the neighboring crystal grains. α is considered to reflect the effect of the reduction of the anisotropy field due to surface defects and the reduction of the nucleation magnetic field due to the orientation dispersion of the easy axis of magnetization [18].

H_A and I_s are intrinsic properties determined by the crystal structure and atomic species, and it is necessary to select rare earth elements with high H_A to increase the coercivity. However, it should be noted that, if a rare earth element having a high H_A in $R_2Fe_{14}B$ structure such as Nd, Pr, Tb and Dy is used, the magnetization decreases because I_s is small. Both α and N_{eff} are extrinsic coefficients that depend largely on the microstructure. That is, magnetically separating the hard magnetic grains by the non-magnetic grain boundaries is also effective for increasing H_C. Although the influence of α is particularly large, the physical meaning of this value is not yet well understood.

As shown in Appendix section, the coercivity of the magnet using only Nd as a rare earth element is approximately 800 kA/m, and only about 15% of the anisotropy field is obtained. This is thought to be because the microstructure of

the actual Nd-Fe-B sintered magnet has not been optimized to exhibit its intrinsic potential. That is, there is still room to extrinsically improve the coercivity.

1.3 Social Situation of Rare Earth Elements

The use of rare earth elements is essential for Nd-Fe-B magnets. Rare earth elements are relatively rare elements, and for this reason their prices fluctuate greatly depending on the supply-demand balance. This situation is explained below.

1.3.1 Rare earth elements used in Nd-Fe-B magnets

The coercivity of Nd-Fe-B magnets, when only neodymium is used as a rare earth element, is about 800-1050 kA/m. Depending on the shape, these magnets can only be used at this coercivity up to about 120 °C, and cannot be used for industrial equipment or automotive applications that are exposed to relatively high-temperature environments. In practical terms, magnets are used in environments where they are subjected to a reverse magnetic field, so they must have a coercivity that is not demagnetized by the reverse magnetic field. The coercivity of a Nd-Fe-B magnet has a negative temperature coefficient, which means that its coercivity is reduced under high-temperature environments. If the reverse magnetic field exceeds its coercivity level, the magnet is permanently demagnetized. For this reason, magnets used in high-temperature environments must have a high coercivity at room temperature.

In order to achieve higher coercivity, Nd is often substituted by Dy and Tb in order to obtain higher coercivity [19]. It is clear from Table 1-1 that $Dy_2Fe_{14}B$ and $Tb_2Fe_{14}B$ have a much higher anisotropy field compared to $Nd_2Fe_{14}B$ and consequently a higher coercivity.

On the other hand, they have a low magnetization and their magnetization is reduced by the substitution, since the magnetizations of Dy and Tb are antiparallel to that of Fe. Magnetic properties of actual Nd-Fe-B magnets and an illustration of their applications is shown in Figure 1-9. As shown, the residual flux density and coercivity are in a reciprocal relationship, and it is difficult to satisfy both. It is generally said that substituting 1 wt% Dy for Nd in $Nd_2Fe_{14}B$ increases the coercivity by 160 kA/m and decreases the residual magnetic flux density by 25 mT. Similarly, replacement with Tb increases the magnetic force by 280 -320 kA/m and decreases the residual magnetic flux density by 25 mT.

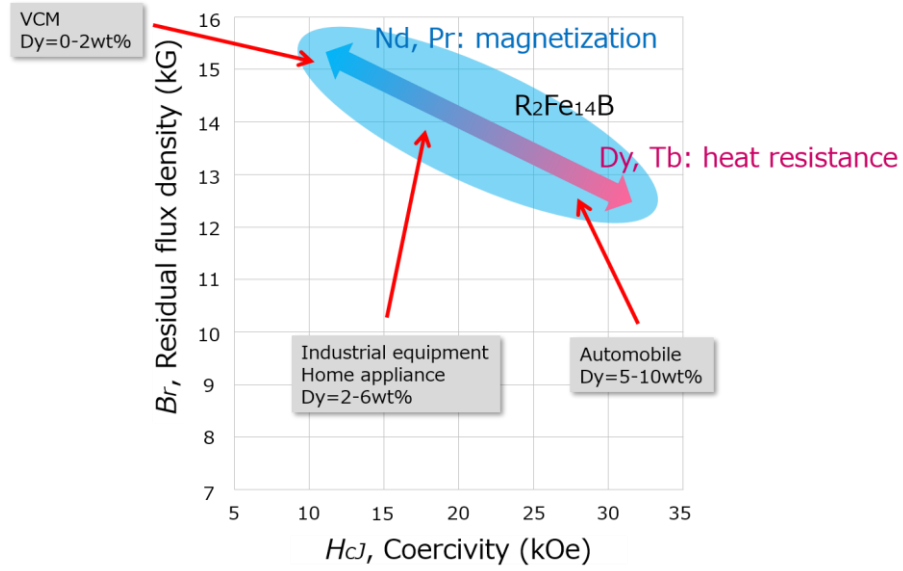

Figure 1-9 Magnetic properties of Nd-Fe-B magnets and their applications.

The degree of heat resistance required for magnets in each application depends on the motor design. In particular, in the case of driving motors and generators for automobiles, it varies depending on the type of xEV, the assumed driving speed and so on, and is also affected by the presence or absence and type of cooling system. Even in the case of an automobile, the magnets for electric power steering

(EPS) and electric parking brake (EPB) are not required to be rotated at a high speed, so there are few exothermic factors such as the influence of eddy current loss, and there are few external factors because they are not installed adjacent to the engine.

Praseodymium (Pr) is also commonly used in Nd-Fe-B magnets. As shown in Table 1-1, $Pr_2Fe_{14}B$ has a saturation magnetization and an anisotropy field close to that of $Nd_2Fe_{14}B$. Pr and Nd are located next to each other on the periodic table and their close nature makes separation and refinement a little difficult, which is one of the reasons why they are often used without separation. The mixture of Pr and Nd is called Didymium and was actually considered to be a single element until 1885. The composition of didymium varies from mine to mine, but Nd:Pr = 3:1-4:1. Therefore, $(Nd, Pr)_2Fe_{14}B$ is often referred to as $Nd_2Fe_{14}B$, and the Pr concentration is about 20-25% in the molar ratio in TRE generally. It is true that the intrinsic magnetic properties of Pr and Nd are close to each other, but there is a disadvantage that the temperature coefficient of coercivity of $Pr_2Fe_{14}B$ is negatively larger than that of $Nd_2Fe_{14}B$. Therefore, Pr is generally not used alone, and didymium is used as a mixed rare earth because it is slightly cheaper than Nd.

1.3.2 Nd-Fe-B magnets demand

The demand for Nd-Fe-B magnets has been increasing and is expected to continue to do so in the future; by 2030, demand is estimated to be at least 240,000 ton and at most 630,000 ton [20]. In 2012, the largest demand, 40%, for Nd-Fe-B magnets was for industrial motors [21]. This includes motors for home appliances and industrial machinery. Replacing induction motors and ferrite motors has significantly improved the energy efficiency of motors. Although demand for magnets for xEVs was only 2% at the time, this market has grown significantly and is expected to continue to grow. The International Energy Agency's (IEA)

estimate of the breakdown of future vehicle types, which is presented at the Energy Technology Perspectives 2012. According to this prediction, about half of all passenger cars should be electrified in some form by 2030. It shows that while overall vehicle production growth will slow down, however the vehicle electric motor production will increasingly increase. Inseparable from the electrification of the vehicle's driving force is autonomous driving. Autonomous driving should use electric control instead of hydraulic control, which has been widely used in conventional automobiles. As a result, the amount of electric motor use in automobiles, such as electric power steering (EPS) and electric parking brake (EPB), is expected to grow even faster. As a result, the demand for Nd-Fe-B magnets with high coercivity is expected to increase rapidly. Against this background, there is concern that the supply of rare earth elements will not be able to keep up with demand in the near future [22]. In particular, concerns over the supply of heavy rare earths could directly affect prices. Social and technical measures are needed to avoid this.

1.3.3 Rare earth mines and supply

Rare Earth Elements are a collective term for 17 elements including the 15 lanthanides (La, Ce, Pr, Nd, Pm, Sm, Eu, Gd, Tb, Dy, Ho, Er, Tm, Yb, Lu) plus Sc and Y. Here, Light Rare Earth Elements (LREEs) refer to elements with lanthanides lighter than Eu and Heavy Rare Earth Elements (HREEs) refer to elements with lanthanides heavier than Gd, plus Sc and Y, being lighter than lanthanides though. In most cases, rare earth ores contain many of these rare earth elements, especially light rare earth elements, in varying amounts. Rare earth elements are unevenly distributed on the earth as shown in Figure 1-10 [23].

Figure 1-10 The world's most famous rare earth deposits [23].

Initially, rare earth elements were excavated and produced in Australia, Malaysia and India and since the mid-1960s, production from the U.S. Mountain Pass has been the major source. However, from the mid-1980s, production in China began to flourish as shown in Figure 1-11 [22], especially from Bayan Obo deposit in North China, and low prices led to the closure of mines outside of China [24]–[28].

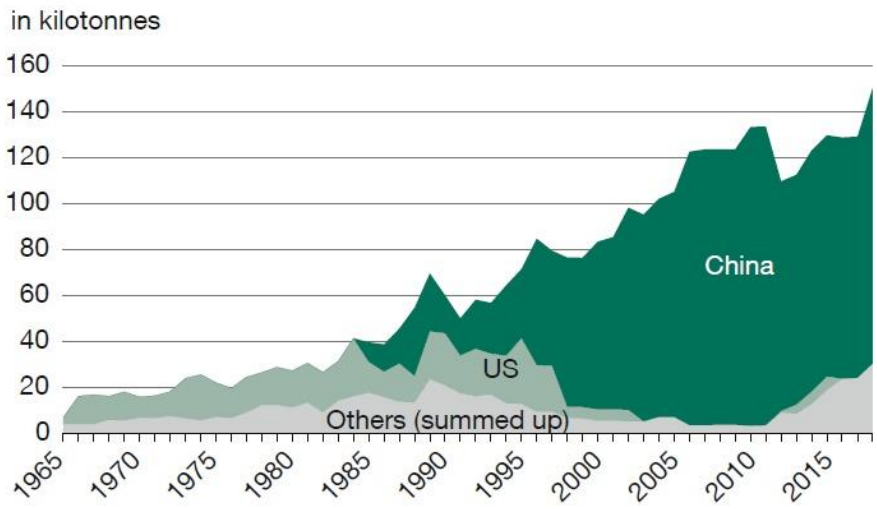

Figure 1-11 Development of production market of REEs [22].

China has less than 50% of the world's rare earth reserves, but today most of the country's output is from China [27]. Furthermore, the production of heavy rare earth elements is only limited to China [29], [30].

There are two main reasons for the bias in the production of rare earth elements in China. The first is that in many cases rare earth elements are present with thorium, radioactive material, which makes their separation difficult, and therefore their price is high, making it difficult to dispose of the residue [31]. The other is that the deposits in South China, where heavy rare earth elements are produced, are special deposits called ion-adsorption deposits. A deposit formed by weathering of rare earth-containing granite to form a clay layer, which is then deposited and densified by the rare earths adsorbed to the clay minerals. This makes the extraction of rare earth elements easier than other deposits. In a conventional deposit, the ore is classified and sorted, refined and graded, and then roasted and heated with acid to decompose the ore and convert it to soluble salts, converting and separating the coexistent iron and other elements into unwanted oxides, and then removing impurities through chemical operations to obtain a mixed rare earth salt. In the case of ion-adsorption ores, however, mixed rare earth salts are obtained by drilling a hole in the deposit, allowing the acid to seep directly into the deposit and recovering the acid flowing out of the boundary between the clay and granite [32]. It is a very simple and inexpensive process for the extraction of rare earth elements, although it is problematic in terms of environmental impact.

Rare earth mixtures made from ion-adsorbed ores must be separated and purified. This is generally done by the solvent extraction method [33]. In this method, each rare earth element is dissolved in the aqueous and organic solvent phases at different concentrations and reaches an equilibrium state. The addition of an extractant with high selectivity for each rare earth ion will enable more

efficient separation. Since a sufficient difference in concentration is not obtained in a single solvent extraction, it is necessary to repeat this process. The mixer-settler consists of multiple stages of separation tanks, and is capable of continuous separation [32]. There are environmental problems such as the extractant itself dissolving slightly in water and the fact that the degraded extractant cannot be completely incinerated, leaving a corrosive residue, which is why it is almost not used in Japan.

The use of the 17 rare-earth elements is very unbalanced. The difference between required and unrequired elements is significant. As mentioned above, many rare earth elements have similar physical and chemical properties and are mined at the same time. Because they are mined according to the elements in high demand, even if the elements in low demand are rare, they will be left over. In other words, if the rare earth elements to be mined are used in a balanced and even manner in accordance with the amount of the rare earth elements to be mined, the supply risk of rare earth elements can be avoided. Of all applications in which rare-earth elements are used, magnet use is the most in terms of volume and monetary value [34], and this proportion is expected to increase year by year [20], [21], [35]. Ohashi estimated the supply-demand balance of each rare earth element. Although it is difficult to make an accurate estimate due to the problem of illegal mining, the demand ratio to the supply in 2014 is ranked with La, Nd, Pr, Dy, Ce, and Tb in order from the highest element [24]. Though La is the highest in numerical value, Ohashi states that the actual situation is different due to the influence of excess in the treasury and illegal mining. With the development of alternative materials, the demand for Ce had been decreased because of a shift to alternative materials for glass abrasives. As a result, of all rare earth elements, the four elements used in magnets, Nd, Pr, Dy and Tb, represent the substantially

highest resource risk. The supply risk of Nd-Fe-B magnets cannot be avoided unless the four elements used in Nd-Fe-B magnets are simultaneously reduced.

1.3.4 Rare earth policy

In 1992, Deng Xiaoping, China's supreme leader, is reported to have said the following. "There is oil in the Middle East; there is rare earth in China. Rare earth resource in China represents 80% of the known global reserves. The position of rare earth to China is comparable to the role of oil to the Middle East. Rare earth has the vital important strategic significance. We have to develop rare earth industry well and exert China's strength of rare earth resource." That's what the relief, as shown in Figure 1-12, in the Baotou National Rare Earth Hi-Tech Industrial Development Zone shows.

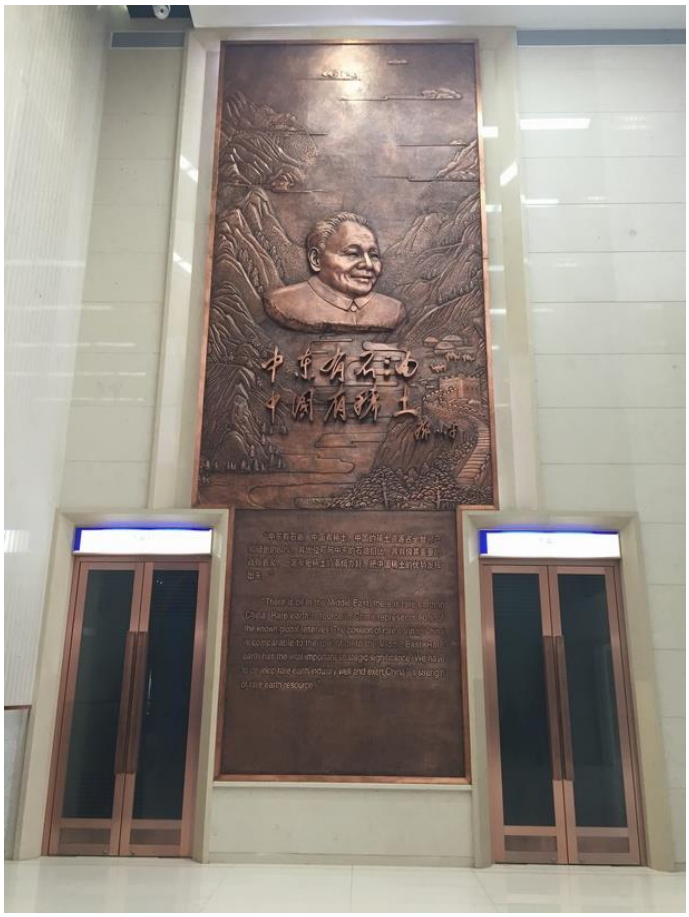

Figure 1-12 A relief of Deng Xiaoping (Photograph taken by the author).

As he said, China's development of rare earth elements has surpassed the world and has always been a strategic material. The economic importance of rare earth elements has been on the rise recently because of increasing demand and their relative scarcity. Rare earth elements are essential for many of today’s most important high-tech products and technologies.

Until now, the price of rare earth elements has been closely related to China's policy [29]. Since 1997, China has set an export license (E/L) for rare earth elements; since 2006, it has imposed export tariffs and set a domestic production control index (a resource index for total mining volume); the 2010 Senkaku Islands dispute led to a substantial embargo on rare earth elements from Japan. The unit

price of rare earth elements reached its highest point in 2011. On the other hand, due to soaring prices, there was a strong movement among end users to substitute rare earths and reduce the proportion of rare earths used, which led to a sudden contraction in demand [29], [36], [37] and a sharp spike in prices from the summer of 2011 as listed in Table 1-2. Before the Senkaku Islands dispute, there was a demand for rare-earth elements in Japan of over 30,000 tons, but after the price of rare-earth elements soared (so-called rare earth shock), the demand is said to have fallen to over 13,000 tons.

Table 1-2 Production volume (2010) and price developments for individual REE oxides [29].

	Production (2010)			Prices (USD/kg)		
	%	tonnes	2009	2011	2013	2015
Ce	42.6	5500	30	100	8	2
La	25.4	33000	38	100	20	3
Nd	17.2	22000	63	270	72	47
Pr	5.5	7200	60	225	85	67
Y	4.4	5700	50	165	26	7
Dy	0.7	910	310	1600	557	271
Eu	0.2	260	1400	3300	1102	269
Tb	0.2	260	1400	2750	925	547

A major problem for the world's rare-earth users was the wide gap in the prices of rare-earth elements within and outside China. The Chinese government had a dual-pricing policy for important rare earth elements [29]. As a result, users of rare-earth elements outside China had a higher cost burden than users inside China, and had been placed at a disadvantage in terms of competitiveness.

In 2012, Japan, the United States, and Europe asked the World Trade Organization (WTO) to settle their dispute over China's export controls. In 2015, Japan, the United States and Europe won the case, abolished the E/L and export tax, then introduced a resource tax in the name of tighter environmental regulations. Resource taxes varied by type of ore, reaching 27% for heavy rare earth elements. During this time, there have been rumors that illegal mining is continuing in China [38], and the Chinese government is reportedly working hard to crack down on it.

Thus, there have been various bargains between China's rare earth policies and increased demand from other countries. There is a huge demand for rare earth elements around the world. Whenever the price of rare earths has risen, attempts have been made to redevelop rare earth mines in other countries, but none of these seem to have been able to sufficiently compete with China's rare earth prices for technological innovation. Particularly in the case of heavy rare earths, we have no choice but to rely on ion-adsorption ores only from South China.

1.4 Motivation

Nd-Fe-B magnets show coercivity only less than 20 % (typically 15 %) of the anisotropy field [18], [39]. Rare earth elements used in Nd-Fe-B magnets are used because of their high single-ion anisotropy due to their 4f electron clouds however the effect on coercivity is extremely limited. In other words, the current Nd-Fe-B magnets do not have the coercivity that should be exhibited, and scarce and expensive rare earth elements are used wastefully. Of course, rare earth elements cannot be removed from the crystal structure of $R_2Fe_{14}B$ of the Nd-Fe-B magnet, but it can be said that elements with excessively high anisotropy are used now. This is because the extrinsic element of microstructural design and control is incomplete and the intrinsic properties are not fully extracted. This is the limitation

of current Nd-Fe-B magnets and the current situation. If microstructural design and control can provide a higher coercivity, i.e., a coercivity closer to an anisotropy field, it also means that rare earth elements with lower intrinsic properties, which are less valuable to Nd-Fe-B magnets at this moment, can be utilized.

As described in Section 1.3, among all the rare earth elements, the rare earth elements used for Nd-Fe-B magnets, i.e., Nd, Pr, Dy and Tb, practically has the highest demand/supply ratio and is in a severe supply risk. In particular, with the increase in motor use in electricity-driven automobile applications, the demand for automotive applications in all rare earth applications is also increasing significantly. This means that in the near future, it would be impossible to produce as many Nd-Fe-B magnets as necessary, and consumers will not be able to benefit from them.

The material science approach of extracting the intrinsic properties of Nd-Fe-B magnets as much as possible by the extrinsic method of microstructural design and control and improving the coercivity is consistent with the solution of the risk of rare earth elements in the present society. Then rare earth elements can be used in a balanced manner and contribute to the development of a sustainable society.

From this viewpoint, the following section summarizes what studies have been conducted to improve the coercivity of Nd-Fe-B magnets. What kinds of studies have been conducted to eliminate waste in the use of rare earth elements is also examined.

1.5 Previous works to improve coercivity

In order to solve these problems, studies have been carried out to improve the coercivity and reduce the amount of rare earth elements used in Nd-Fe-B magnets in terms of processes and materials. From a microstructural point of view, there

are two methods: controlling the structure of grains and controlling the structure of grain boundaries. The former is grain size control and core-shell structure of grains, and the latter is composition and thickness control of grain boundary phases. In addition, these microstructural controls are not only achieved by the material composition, but also greatly related to the process. A number of studies have been conducted on these issues and are summarized here.

1.5.1 Grain design

Grain size

As described in Section 1.3.1, in general, in order to improve the coercivity, Dy and Tb, which are heavy rare earth elements exhibiting a high anisotropy constant and an anisotropic magnetic field, are added. Although the anisotropy field of Nd-Fe-B magnets is extremely high (5330 kA/m) as listed in Table 1-1, their coercivity is less than 20% [18] of that (≈800-1050 kA/m). If the potential of the anisotropy field can be fully extracted, a high coercivity can be obtained without relying on heavy rare-earth elements.

One of the common methods to increase the coercivity is to reduce the crystal grain size [40]–[48]. The magnetization reversal mechanism of Nd-Fe-B sintered magnets is explained by the nucleation mechanism [17], [18], [49], [50]. If the magnetization reversal is due to the nucleation of inverted domains, the frequency probability of nucleation is correlated with the surface area of the grains [18]. That is, the nucleation frequency is inversely proportional to the logarithm of the square of the mean grain size [40], [51]. Figure 1-13 shows the relationship between the particle size of Nd-Fe-B magnet powders without HREEs and the coercivity of sintered magnet made from those [40]–[45], [47], [52].

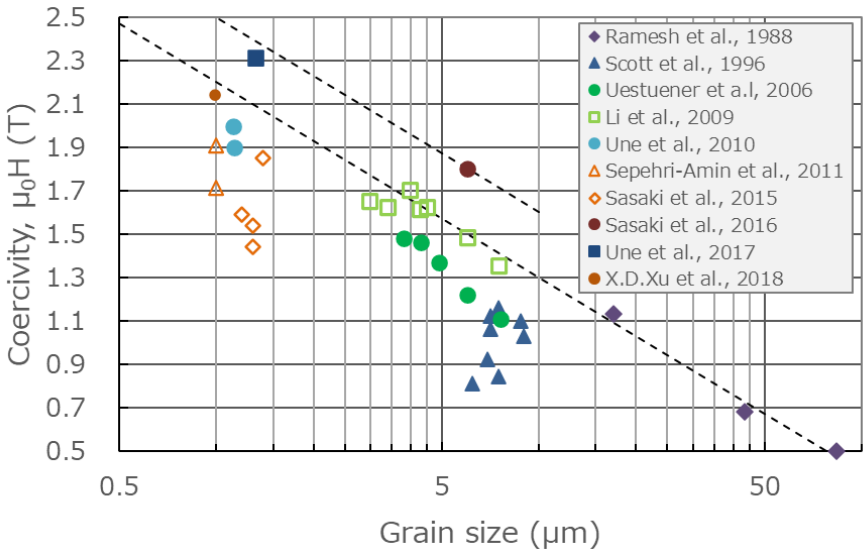

Figure 1-13 Coercivity of anisotropic Nd-Fe-B magnets plotted as a function of crystal grain size.

In the case of sintered magnets, the peak of the coercivity is around 3 μm [42], [43]. When the particle size of the milled powder is reduced, the specific surface area of the powder increases, which leads to a severe oxidation of the powder and a substantial decrease in the coercivity because of the decrease in the amount of R-rich phase at the grain boundary. For this reason, milled powder with a grain size of 3-5 μm is usually used in industry. If the particle size is less than this, generally the efficiency of milling for higher coercivity will decrease significantly. Sagawa et al. succeeded in obtaining pulverized powder of about 1 micron in particle size by using helium as carrier gas in jet-milling [44], [53], [54] since the flow rate of helium is higher than that of nitrogen, the grinding efficiency is greatly improved. However, the aforementioned reduction in grinding efficiency leads to an increase in the amount of fine powder that is undercut by the cyclone [55] and increases the amount of rare-earth elements that are wasted.

Another problem is that the initial magnetization behavior of the magnet becomes worse as the grain size is reduced. Normally, magnet products are shipped in an unmagnetized state, and after being incorporated into a motor or the like at the customer's side, they are magnetized by an external magnetic field. If the initial magnetization behavior is poor, the magnetization of the magnet does not sufficiently increase with respect to the applied magnetic field and does not reach saturation magnetization [56], [57]. The initial magnetization behavior of a magnet with small grain size shows a two-step curve of magnetization rise in response to the external magnetic field [44], [58]. It suggests that the grains in the thermally demagnetized state are in a mixed state with grains in the multi-domain state and grains in the single-domain state [10], [18]. In Nd-Fe-B magnet, the magnetization reversal is considered to occur by the nucleation of reverse domains from the grain boundaries of magnetically isolated grains [59] and this is called nucleation-type coercivity mechanism [17], [18]. The domain wall movement is relatively easy, the generation of the reverse domain requires more energy. In other words, a larger inverse magnetic field is required for the magnetization reversal of single-domain grains compared with multi-domain grains. The magnets used in motors are usually embedded in the rotor as non-magnetized state and are magnetized by applying a magnetic field from outside of rotor [56], [57]. Therefore, there is a limit to the magnetic field strength that can be applied in terms of ease of manufacturing, and magnets with poor initial magnetization characteristics are not preferred. For these reasons, it is undesirable that the sintered body has a grain size which becomes a single magnetic domain in a thermally demagnetized state.

Core-shell structure

As a technique for improving coercivity by microstructure control different from grain boundary control, production of main phase grains with core-shell structure is known [60], [61]. The demagnetization mechanism of the Nd-Fe-B magnet is explained by the nucleation mechanism [17], [18], and the magnetization reversal of the whole grain occurs by the formation of the reverse magnetic domain on the surface of the grain. Therefore, if a core-shell structure in which a rare earth element having high anisotropic field is arranged on the surface of the grain and a rare earth element having high saturation magnetization is arranged in the inside of the grain, high coercivity and residual magnetic flux density can be compatible. Based on this concept, the core-shell structure has been actively formed by the dual alloy method or the binary main phase (BMP) method [62], [63]. However, the effect was limited because both phases were originally easy to solid-solute and mixed by heat treatment.

As a way to improve it, researchers at Shin-Etsu Chemical Co., Ltd. have developed a technique called grain boundary diffusion [64], [65]. In this method, a very high coercivity was realized with a small amount of addition of heavy rare earth element by optimizing the arrangement of the elements [66]. The surface of the sintered magnet is coated with a heavy rare earth element, and this is heat-treated in the vicinity of an annealing temperature. The coating method includes a slurry coating method [65], [67]–[69] and a gas phase method [70]–[72]. Heavy rare-earth elements dissolve in the R-rich phase and diffuse into the interior of the magnet through the grain boundaries. Therefore, $R_2Fe_{14}B$ phase containing heavy rare earth elements in high concentration is formed on the particle surface. This creates a core-shell structure. The formation mechanism of the shell was initially thought to be diffusion of heavy rare earth elements into the main phase particles [72], but has come to be thought to be grain growth makes the structure [67].

However, in this method, it is difficult to avoid the cost increase due to the addition of a new process, the applicable magnet size (thickness) is limited because of the limited diffusion driving force, and above all, the amount of heavy rare-earth elements discarded due to surface processing is large. This is because heavy rare-earth elements, which are diffusion sources, must be removed from the surface in order to keep the flat surface of final product and contain the most heavy rare-earth elements there. Thus heavy rare-earth elements are used and consumed much more than the amount contained in the magnet as a final product.

In any case, the magnet using the core-shell structure is premised on the use of rare-earth elements having higher anisotropy such as heavy rare-earth elements for shell. Therefore, it is not considered to be a fundamental solution for not using these elements.

1.5.2 Grain boundary design

R-rich grain boundary

Attempts have been made to improve the coercivity by controlling grain boundaries since the invention of Nd-Fe-B magnet. Because the coercivity is strongly influenced by the microstructure, especially the magnetic isolation of the ferromagnetic grains, important microstructure changes are expected to occur during the post-sinter annealing process, particularly at the grain boundaries [73]–[75]. However, the reason for this effect had not been understood for a long time since the discovery of $Nd_2Fe_{14}B$ magnet. One reason for this is that there had no way to accurately analyze the composition and state of very thin grain boundaries, which are as thin as a few nm in the past. For example, in an earlier paper by Sagawa et al., the Nd concentration in the R-rich phase was reported to be 95 at% and the Fe concentration to be 3-5 at% [7], which is much higher than the Nd concentration currently considered.

The grain boundary phase, formed by an annealing process [53], is a R-rich (Nd-Fe based) phase with a small amount of Cu (≈0.1 at%) and had been considered to be non-magnetic [73], [74]. A small amount of Cu addition has been found to be effective in increasing the coercivity [76] and has been widely used in industry. The grain boundary phase plays an important role to decouple the exchange interaction between each $R_2Fe_{14}B$ grains, then the movement of magnetic domain walls will be stopped at the grain boundary. Therefore, the R-rich phase configuration and magnetization are important [76]. However, the exact composition of the grain boundary has only been revealed in the last 10 years or so by detailed studies by Hono and his group [18], [76].

Sepehri-Amin et al. accurately determined the composition of thin grain boundary phase using the 3DAP method and found that the (Fe + Co) concentration was as high as 65 at% [76], [77]. A thin film having the same composition was formed, and the magnetic curve was measured to find a soft magnetic phase having a magnetization of 440 emu/cm^3 [76]. Nakamura et al. directly observed the grain boundary phase remaining on the fracture surface of Nd-Fe-B sintered body using the soft X-ray magnetic circular dichroism method, and reported that the magnetization was about 60% of that of Nd-Fe-B grains [78]. In addition, a research group of Hitachi Metals, Ltd. conducted magnetization estimation of the grain boundary phase of the fracture surface using spin SEM, and concluded that it was about 0.4 T [79].

As far as the effects of copper addition, thin Cu-enriched layer was also formed along the R-rich/$Nd_2Fe_{14}B$ interface and that could decouple the exchange interaction [80]–[82]. The eutectic temperature of Nd-Cu was as low as 520°C [83], which could be due to its liquidation during the annealing process and its penetration between the particles by capillary action. The role of the R-rich phase,

which had been used since the invention of the Nd-Fe-B magnet, became clear 30 years after the invention.

Ga-added grain boundary

On the other hand, the effect of adding Ga to Nd-Fe-B magnets to improve their coercivity has been recognized for a long time. Tokunaga et al. reported that Ga addition of several at% contributed to the improvement of coercivity in the late 1980s [80], [84]–[87]. At that time, several studies were made on the coercivity of small quantity of Ga additions using a melt span [88]–[90]. However, at the same time it was known that the magnetization and the squareness decrease by Ga addition [91], and the coercivity could decrease depending on the composition [84]. Such effects were observed not only for Ga but also for various minor additives such as Al, Nb, Ag, Au and Si [92]–[95]. Initially, it was considered that the increase in coercivity due to the addition of Ga was caused by the improvement in wettability of the grain boundary phase [91], [96], [97], which can improve the penetration of the R-rich phase into the grain boundaries. Since the amount of Ga addition was small and the analysis technology was not developed at that time, it was not possible to analyze where and what kind of phase Ga existed in a very narrow grain boundary region. Formation of Nd_3Ga and Nd_5Ga_3 [98], [99], precipitation in Nd-Fe-B grains [100], and formation of new grain boundary phase were suggested [101], [102]. Furthermore, TEM analysis revealed that the $Nd_6(Fe, Ga)_{14}$ phase was observed at triple junction [91], [98], [99], and that $Nd_6(Fe, Co)_{13}Ga$ was effective for corrosion resistance [100], suggesting the formation of $Nd_6Fe_{13}Ga$ phase. Little is known about the existence of these phases, but it is not clear whether they are at the triple junction or at the grain boundary and how they are formed.

It has been indicated that the Ga-containing phase promoted the magnetic isolation between particles [97]–[99], [101] however the physical mechanism of the Ga effect on coercivity still have not been clear. In this way, it was recognized that Ga addition contributed to the improvement of coercivity, but the physical and magnetic effect remained unknown. In addition, since there is a problem of squareness due to Ga addition, it is considered that Ga addition had not used in the mass production magnet.

TDK Corporation had manufactured Bi-containing magnets for higher coercivity in the past, and the formation of $R_6Fe_{13}M$ phase [96], [103], [104] at grain boundaries was expected [105] though it was difficult to identify a trace of the grain boundary phase with the analytical capability at that time. Although it was known that this phase affected the coercivity, its mechanism was not clearly understood. Therefore, the application of Ga, Si and Sb as an M element has been studied to form $R_6Fe_{13}M$ phase at grain boundaries since 2007 and found Ga addition was effective.

TDK corporation has been developing Dy-free magnets, and in October 2012 began manufacturing NEOREC 46HF magnets, which was the first Nd-Fe-B magnet using $R_6Fe_{13}Ga$ phase, with a coercivity more than 1274 kA/m in a Dy-free composition. Showa Denko Co., Ltd., an alloy manufacturer, made a press release[1] in October 2013, stating that it had succeeded in developing a Dy-free magnet alloy for factory automation applications and had a presentation at the domestic conference about the existence of $RE_6Fe_{14-x}M_X$ phase [103], [106]. Chuden Rare Earth Co. Ltd., another alloy manufacturer, also reported on Ga-added alloys, but it was reported that what phase Ga would form was unclear [107]. Thus, the

[1] https://www.sdk.co.jp/english/news/13382/13817.html

formation and formation mechanism of grain boundary phases in Ga-doped Nd-Fe-B magnets and their contribution to coercivity have not been well understood.

The authors reported the formation of $Nd_6Fe_{13}Ga$ [108], [109] at the grain boundary as concluded in this thesis and the phase was also called as $Nd_6(Fe,Ga)_{14}$ phase [52], [110]. The reason why the existence of this phase has an effect on the coercivity improvement was not clear before then.

Ce-added grain boundary

After the Senkaku Islands issue in 2010, rare earth price hikes have spurred efforts to reduce the use of Nd and Pr as well as Dy and Tb. In particular, studies were conducted to replace Ce, which is inexpensive and rich in resources, with Nd and Pr to reduce the use of expensive rare earth elements.

The substitution of Ce as an alternative light rare-earth element has been actively studied for $R_2Fe_{14}B$ alloy [111]–[115], melt-spun [116]–[128], thin film [129], hot-deformed [102], [130]–[134], and sintered magnets [121], [135]–[142] over the last ten years. Simultaneous substitution with La, which is also an abundant element, has been also widely studied [121], [122], [133], [135], [143]–[146]. Since the saturation magnetization *Is* and the anisotropy field H_A of $Ce_2Fe_{14}B$ and $La_2Fe_{14}B$ are much lower than those of $Nd_2Fe_{14}B$ as listed in Table 1-1, it is not easy to attain magnetic properties that are equivalent to $Nd_2Fe_{14}B$ through substitution as described in section 1.2. Since the residual magnetic flux density is largely determined by the composition, efforts have been made to improve the coercivity. The improvement of coercivity is also an important issue affecting $R_2Fe_{14}B$ magnets with a smaller Nd content.

Since an $R_2Fe_{14}B$ sintered magnet exhibits a nucleation-type coercivity mechanism [17], [18], it is possible to increase the coercivity by increasing the

anisotropy of the shell in the core–shell grain structure [141], [147]. To this end, techniques such as a binary main phase (BMP) approach involving the blending of two kinds of $R_2Fe_{14}B$ powder [119], [121], [135], [148], [149], which improved the coercivity of less than 160 kA/m [150], and a grain-boundary diffusion approach [130], [148], [151] have been used as same as general Nd-Fe-B magnet. As a process similar to grain boundary diffusion, the infiltration method of grain boundary components is used in hot-deformed magnets [102], [131]–[133]. Tang et al. attempted to improve coercivity by infiltrated hot-deformed Ce-Fe-B with Nd-Cu, but the increase was only about 0.2 T [131]. It has been found that the manipulation of the grain boundary is important to both techniques.

Grain boundary phases of Ce-substituted $R_2Fe_{14}B$ magnets have also been studied. As described above, the method of improving coercivity by introducing a R-rich phase into the grain boundaries has been widely used since the development of $Nd_2Fe_{14}B$ magnets. It has been revealed that an $R_2Fe_{14}B$ magnet with Ce substitution forms not only an R-rich but also an RFe_2 grain-boundary phase [135], [144].

It has been reported that the RFe_2 phase is effective for improving the wettability of grain boundaries as well as the general R-rich phase [117]. An increase in coercivity and a decrease in magnetization of a (Nd, Ce)-Fe-B system magnet at a Ce concentration of about 20% have been demonstrated by melt-span experiments [117], [118], [140]. It has been reported that this is caused by phase separation [135] and valence change of Ce [117], [120], but no clear conclusion has been reached. Thus, the role of the RFe_2 phase remains still unclear.

As a result of such research, the coercivity of sintered magnets obtained by substituting Nd and Pr with other resource-rich rare earth elements is difficult to be accurately compared because the substitution amounts are different, but the

maximum coercivity is about 720 kA/m [135], [140] and the maximum energy product is about 240 to 280 kJ/m^3 [135].

1.5.3 Grain boundary protection in near-net shaping process

Here was summarized on past investigation on reduction of rare earth use from process. In order to obtain the magnet as the final product, the magnet is cut and polished in the manufacturing process, and it is effective to reduce all rare earths used for the magnet by minimizing the amount of the works. The near-net shaping method has been studied for this purpose, but the problem is always how to maintain the grain boundary phase and coercivity.

In the application of autonomous driving technology to automobiles, it is inevitable to use electric power for all control systems of automobiles, and for this reason, electric power for power steering, parking brakes, etc., has been promoted. Surface permanent magnet (SPM) motors are often used for these motors, and arcuate magnets are used instead of simple rectangular magnets [152] . More machining is required to produce such shaped magnets. Since the machined residue is disposed of as an oxide that is difficult to recycle, the amount of Nd, Pr, Dy, and Tb disposed can be reduced when near-net shape molding becomes possible. The difficulty in near-net shaping is due to the poor flowability of the dried magnet powder [44], [153]. This is because powder with low flowability is difficult to fill in the die during pressing [154]. In particular, the narrower the opening and the deeper the cavity, the more difficult it is to fill. The Nd-Fe-B magnet powder has poor flowability due to the following reasons: the shape is irregular because it is a breakdown powder [155]; the Hamaker constant [156] is relatively large because it is a metal powder and as a result Van der Waals adhesion is large [157]. Powders with high cohesiveness generally have low fluidity.

By the way, the Nd-Fe-B magnet powder is pulverized from a polycrystalline substance to a single crystal size, and in the state before magnetization, the magnetic flux is closed in the particle of multi domain structure, and as a result, it is considered that magnetic aggregation is not generated.

If the flowability is poor, it is difficult to fill the cavity of the narrow and deep die with powder. Therefore, a desired shape is cut out by molding using a die shape which is easier to fill and cutting the sintered magnet. In order to improve the filling property of the mold, several molding methods different from the conventional dry molding technique have been developed [158] such as the wet molding method [159], [160], the metal injection molding (MIM) method [161]–[163] and additive manufacturing (AM) [164]–[167] as described below.

In the wet process, powder is filled into a mold in a slurry state. It is well known that this method was mass-produced and applied by Hitachi Metals, Ltd. as a method for handling powders at low oxygen concentrations, which is called Hitachi low oxygen process (HILOP). Since oil is used as a dispersion medium, the magnet powder does not come into contact with oxygen, and oxidation of the magnet powder is prevented. Because the slurry is macroscopically liquid, it is easy to fill a narrow cavity. However, the residue adheres to the piping and the like, and the material yield is lowered from the viewpoint of the whole magnet manufacturing process.

In the metal injection molding process, the magnet powder is mixed with a thermoplastic resin and injection molding is performed. In the molding, the magnetic field orientation is also carried out. As with the general injection molding of resin, it is easy to form a desired shape, however there is also a problem that the material yield does not increase because the runner remains as same as conventional ceramic injection molding (CIM) process.

Additive manufacturing (AM) is a technique to form an object by stacking materials, and is a relatively new near-net shaping technique. Although applications to magnets have been attempted, their use is limited to isotropic bonded magnets [165], [166] because of the difficulty in orienting primary particles and in demineralizing resins. Application to sintered magnets requires the construction of measures to prevent carbonization and oxidation as well as the Wet and MIM methods.

A problem common to those methods is that the elimination of oil or resin is required as a pre-process for sintering. Since oils and resins contain carbon or both oxygen and carbon, they easily combine with Nd at high temperatures to form oxides and carbides. Since this removal is not easy, there is an adverse effect that the size of the magnet is limited. To prevent this, it is necessary to carry out a long time decarbonization such as long-time low temperature heating, treatment in hexane [161], [163], or/and a heat treatment in hydrogen [161], [162], which causes a complicated magnet manufacturing process and a cost up. Further, in these methods, residue tends to remain in, for example, pipes and filters during the process, and the deterioration of the material yield is a problem. Therefore, it is difficult to reduce the amount of rare earth elements in total.

As illustrated in Figure 1-6, Nd-Fe-B magnets are composed of grains, grain boundary phases, and several impurity phases. The larger the volume occupied by the grains, i.e., the $R_2Fe_{14}B$ phase, the higher the magnetization is obtained, but the grain boundary phase decreases. As discussed in Section 1.5.2, a decrease in the grain boundary phase enhances the exchange interaction between particles and reduces coercivity [168]–[175]. Therefore, one of the most important issues in near-net shaping is to prevent coercivity degradation by constructing an oxygen and carbon less process.

In this regard, in the late 1990s, researchers at Sumitomo Special Metals Co., Ltd. developed a granule forming method [171]. This is the only previously reported metal magnet granulation technique. Flowability of powder was improved by using spray-dry granules. The oxygen content had to be kept below 10,000 ppm [175]. To avoid oxidation of Nd-Fe-B magnet powder as much as possible, cold water with reduced dissolved oxygen was used [170] as a dispersion medium and poly-vinyl alcohol was used as a binder when preparing a slurry to be applied to the spray dry method. The carbon content had to be kept below 1,000 ppm [171]. For that purpose, a hydrogen decarbonization process was added to reduce residual carbon [171]. Although the coercivity was maintained in exchange for the addition of the high-cost decarbonization step, the obtained residual magnetic flux density remained at about 90 to 95 % of using non-granulated powder due to the strength of the bonding force between the primary particles. Although the granule forming method is effective in reducing magnet waste by near-net shape forming, it is difficult to reduce residual oxygen and carbon in order to maintain coercivity, and a problem remains that sufficient residual magnetic flux density cannot be obtained.

1.6 Purpose of the present study

The purpose of this thesis is to improve the coercivity in an extrinsic manner by designing and controlling the microstructure, especially the grain boundary structure. This requires material science of how and what phases with what magnetic properties are arranged at grain boundaries, and why they improve coercivity. Especially, the introduction of new grain boundary phase is examined. Thus, if the dependence on the intrinsic characteristics of the specific rare earth elements can be reduced, it is possible to reduce the amount of those specific rare earth elements used in the Nd-Fe-B magnet.

Although the amount of rare-earth elements cannot be reduced compared with the stoichiometric composition, the required magnetic properties can be ensured by using rare-earth elements with lower intrinsic properties and supplementing with an extrinsic method of grain boundary phase control. Furthermore, a process that utilizes these technologies and can reduce the amount of rare earth element waste in the manufacturing process is proposed.

If the use of Nd, Pr, Dy, and Tb, which are the four elements with the largest resource risk among whole rare earth elements, can be reduced, it will contribute to the sustainable development of social demands such as the future electrified vehicle and autonomous driving society. Since the reduction of one element is insufficient and the reduction of all four elements is necessary, the fundamental study on coercivity of Nd-Fe-B magnet was aimed. The actual target was to reduce all elements by 50%. The purpose and solution method are described in detail below;

Nd and Pr are rare earth elements that have been considered essential for Nd-Fe-B magnets, and Dy and Tb are rare earth elements that have been considered essential for high coercivity magnets. Therefore, it is necessary to consider the improvement of coercivity by using different grain boundary phases for each of them.

In order to reduce the amount of Dy and Tb used, the grain boundary phase of $Nd_6Fe_{13}Ga$ was introduced. In the past, attempts have been made to improve the coercivity by using Ga-doped magnets, but these improvements are not sufficient and have not been applied to commercial magnets. Moreover, there is no clear report that $Nd_6Fe_{13}Ga$ could form at grain boundary but triple junction, and the magnetic separation performance is not clear. The formation of this grain boundary

phase, the confirmation of its existence, and the elucidation of its magnetic characteristics and formation mechanism are carried out. In addition, the mechanism of how the formation of this phase contributes to the enhancement of coercivity is verified. By further extracting the potential of Nd-Fe-B magnets that do not contain Dy and Tb, reduction of the use of Dy and Tb by more than 50% is aimed. This is summarized in Chapter 2.

The introduction of $R_6Fe_{13}Ga$ and RFe_2 phases is attempted to reduce the use of Nd and Pr. (where R is a plurality of rare earths including those other than Nd, Pr, Dy and Tb) Substitution with Ce has been attempted to reduce the use of Nd and Pr. However, there is no report that $R_6Fe_{13}Ga$ was formed in the grain boundary phase containing Ce. Therefore, we first search for candidate rare earth elements to replace Nd and Pr by elements rich in resources including Ce, and introduce $R_6Fe_{13}Ga$ grain boundary phase in this magnet, and clarify its magnetic properties and formation mechanism. Furthermore, the effective use of the RFe_2 phase was investigated. The mechanism of how the formation of these phases contributes to the enhancement of coercivity is verified. This leads to the extraction of the potential of Nd-Fe-B magnets with 50% reduction of Nd and Pr. This is summarized in Chapter 3.

For the purpose of reducing the amount of rare earth element waste in Nd-Fe-B magnet manufacturing, the introduction of the technique which enables the near-net shaping without damaging the grain boundary phase is tried. Further reduction of rare earth elements will be achieved by establishing a method applicable to magnets with new grain boundary phases introduced in Chapter 2 and Chapter 3. Many near-net shaping methods have problems of oxidation and carbonization of grain boundary phase, and are not necessarily connected to actual waste reduction. Therefore, a granule forming method which retains the grain boundary phase and does not damage the coercivity of the magnet is established. A new granule called

liquid-bound granule is introduced to protect the grain boundary phase from oxidation and carbonization. Thus, the waste amounts of Nd, Pr, Dy and Tb are reduced. This is summarized in Chapter 4.

Chapter 2 Microstructural design of Ga-added grain boundary phase for Dy and Tb reduction

2.1 Introduction

In 1997, Toyota Motor Corp. introduced the Prius, a Hybrid Electric Vehicle (HEV). Electric cars had existed before then, but they never became a major player because of the range problem. The Prius acted as a hybrid, seamlessly connecting the engine and electric motor drive, making it distinct from previous electric cars with less mileage. Since that time, a large amount of highly heat-resistant Nd-Fe-B magnets has been used for the main motor and generator in automobiles.

Depending on the vehicle type, magnets for the main motor and generator for electrified vehicles are expected to be used at a high temperature of about 140-200°C. In contrast, the coercivity required for magnets depends on the design of the motor, but it can be as high as 1700-2700kA/m at room temperature, which is considerably higher than that of motors for industrial equipment and home appliances. When a simple substitution of Nd and Dy or Tb was attempted to achieve this coercivity, the amount of substitution was equal to around 5-10 wt% Dy or 2.5-5 wt% Tb. As shown in Table 1-2, as of 2014, the price of Dy oxide and Tb oxide were more than five times and ten times that of Nd oxide, respectively, so the price of such high heat-resistant magnets is very expensive, and there have been concerns about resource depletion and supply. Furthermore, simple substitution of Nd with heavy rare-earth elements greatly reduced the magnetization of the magnet, resulting in a decrease in the torque of the motor. Under these circumstances, it was necessary to develop a technology to achieve high coercivity without using heavy rare earth elements, such as Dy and Tb.

In this background, in order to obtain a magnet with high coercivity which can be used for motor and generator of electrified vehicles without using heavy rare earth elements have keenly studied. In particular, the isolation of each grain by grain boundary phase control was attempted in the Ga-doped system to take advantage of the high anisotropy field of Nd-Fe-B magnets. The detailed observation of grain boundaries in relation to heat treatment was also carried out to understand the mechanism of high coercivity.

2.2 Experimental procedure

The sintered magnets were prepared by the conventional method as shown in 1.1.2. The details are described below.

2.2.1 Sample preparation

All raw alloys were produced by the strip casting method and had the composition of (14-14.5) at% TRE (Total Rare Earth)-Co-B-M-bal. Fe (M=Cu, Al, Ga, Zr). The rare-earth elements contained in the alloys were Nd and Pr, and the amount of others was negligibly small.

The raw alloys were coarsely pulverized by a hydrogen grinding method followed by fine pulverization by a jet milling method to obtain fine powders of 2.5 to 3.5 μm in average diameter. The powders were pressed in a magnetic field of 1600 kA/m to obtain compacts. Those compacts were sintered for 4 hours at around 1273 to 1333K in a vacuum, and were then annealed for 1 hour. The pulverizing, pressing and sintering processes were carried under a low oxygen atmosphere of less than 50 ppm.

2.2.2 Measurement of general properties

The magnetic properties of the specimens were measured with a BH tracer (Tamakawa Co., Ltd.), high-temperature BH tracer (Toei Industry Co., Ltd.) and vibrating sample magnetometer (VSM, Tamakawa Co., Ltd.). Microstructural analysis was performed by FIB-SEM, EPMA, TEM and 3DAP (three-dimensional atom probe).

2.2.3 Grain boundary evaluation by 3DAP

Atom probe tomography is a powerful characterization method to obtain three-dimensional distributions of atoms in materials at nearly atomic-scale resolution by detecting atoms one by one. A Three-Dimensional Atom Probe (3DAP, LEAP4000, AMETEK CAMECA) was applied to evaluate the composition at grain boundary. The analysis area, which includes grain boundary region, is sampled, and mounted to the sample holder for 3DAP by using FIB-SEM. The sample is prepared in the needle shape with a diameter of 50-100nm and length of several hundred nm. The specimen was biased by laser pulsing and evaporated atoms were detected by a position sensitive detector to obtain a 3D mapping of the elements as illustrated in Figure 2-1. A line profile perpendicular to the grain boundary plane was taken from the 3D mapping in order to roughly estimate the grain boundary width.

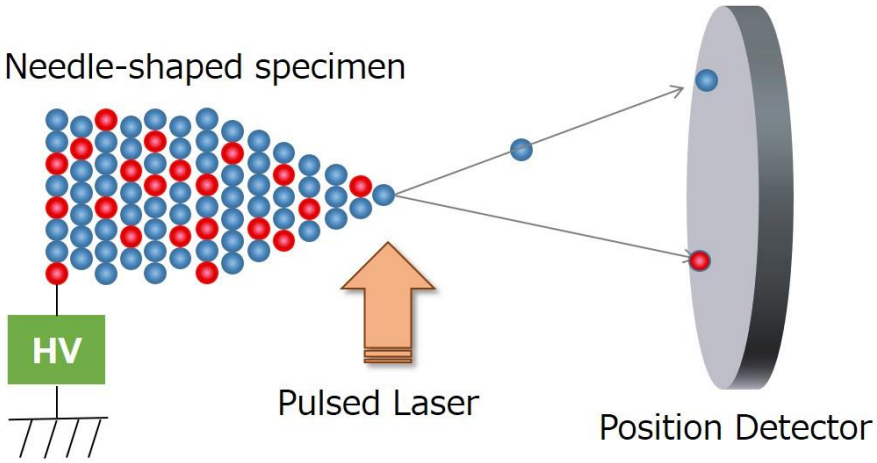

Figure 2-1 Principle of 3DAP measurement.

2.2.4 Synchrotron radiation measurement

The XRD measurement for the phase analysis was performed with synchrotron radiation. The measurement was carried out on beamline BL02B2 at SPring-8 in Hyogo, Japan. An isotropic sintered magnet was prepared. A sintered specimen was ground to the size of 0.24 x 0.24 x 15 mm and then sealed in a quartz tube capillary filled with inert gas as shown in Figure 2-2. For the high temperature measurement, the specimen was heated to a desired temperature at a heating rate of 50 K/min, after which XRD measurements were performed twice within 4 min, and the specimen was then heated repeatedly to another desired temperature. The XRD profiles were measured with a wavelength of 0.412452(2) Å.

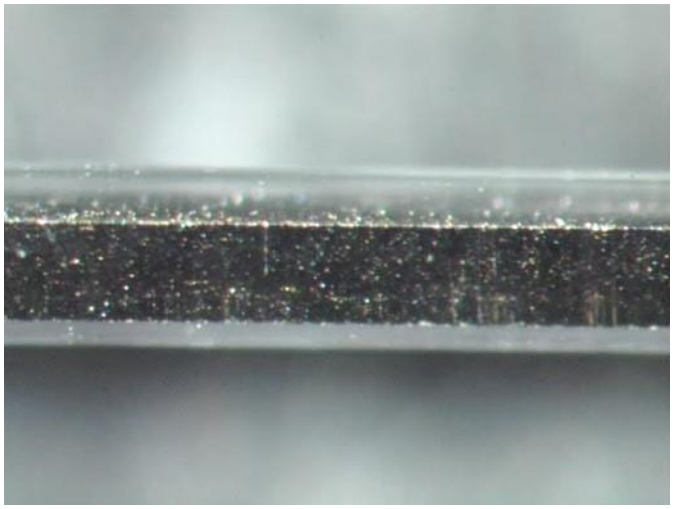

Figure 2-2 A specimen for XRD measurement in a quartz tube.

2.2.5 Coverage ratio of grains by grain boundary phase

The grains are surrounded by grain boundary phases existing at the triple junctions and grain boundaries. In order to evaluate the microstructure quantitatively, the coverage ratio of grains by the grain boundary phase was estimated. Grains and grain boundaries were recognized automatically on SEM images by using an in-house image analysis software. Because it was not possible to recognize grain boundaries thinner than 20 nm in the magnitude of SEM image as shown in Figure 2-3, those grain boundaries were manually complemented on the image. The ratio of the length of the grain boundary which was automatically detected to the length of the grain boundary which was manually complemented was defined as the coverage ratio of grains by grain boundary phases with thicknesses of more than 20 nm.

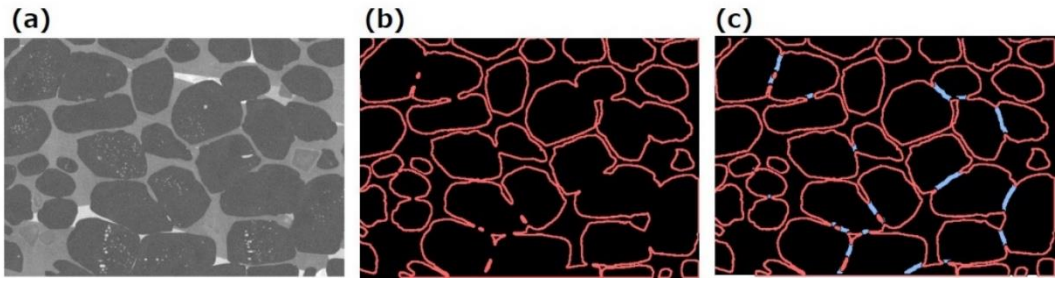

Figure 2-3 Derivation of coverage ratio; (a) SEM photographs, (b) automatically detected grain boundaries and (c) manually complemented grain boundaries.

2.3 Results and discussions

2.3.1 Particle size

It was confirmed how small the grain size can be reduced in terms of initial magnetization behavior. Sintered magnets with various powder diameters as starting material were prepared. A magnetization field of 160 kA/m was applied to the magnets and magnetic flux was measured with a flux meter, after which a magnetization field of 320 kA/m was applied and increased repeatedly to that of 4776 kA/m. The magnetization ratio normalized by the amount of magnetic flux at full magnetization as a function of magnetization field is shown in Figure 2-4.

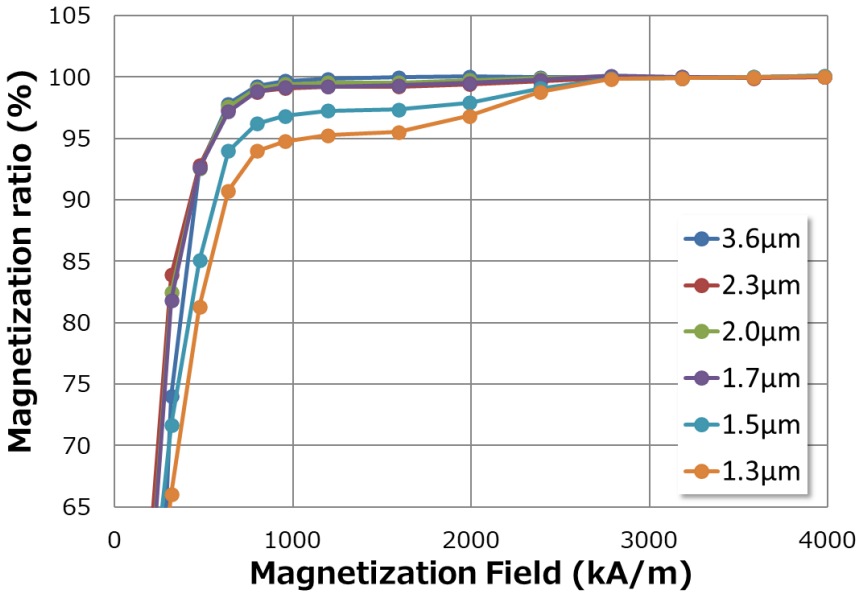

Figure 2-4 Initial magnetization curves for Nd-Fe-B magnets with various D50 starting powders.

Magnets with starting material having a D50 less than 2.0 μm show two-step curves. It is considered that step is related to the magnetization rotation of single domain. In the case of the 1.3 μm specimen, the magnet is considered to contain 5 % of single domain grains estimated from the 1st step magnetization, which are harder to magnetize than multi domain grains which show nucleation type magnetization [17], [18]. Considering the fact that the coercivity increases as the crystal grain size becomes smaller, a fine powder with an average diameter of 2.5 - 3.5 μm was applied to the development of the HREE-free magnet.

2.3.2 Magnetic properties of Ga doped specimen

A developed specimen with a Ga addition of 0.6 wt% was prepared with using a diameter for starting powder of 2.5 μm. Its magnet composition and heating conditions were optimized to achieve the best balance of residual magnetic flux

density, coercivity and squareness ratio. The developed specimen showed residual flux density of 1370 mT, coercivity of 1830 kA/m and squareness (H_k/H_{cJ}) of 97%, as shown in Figure 2-5.

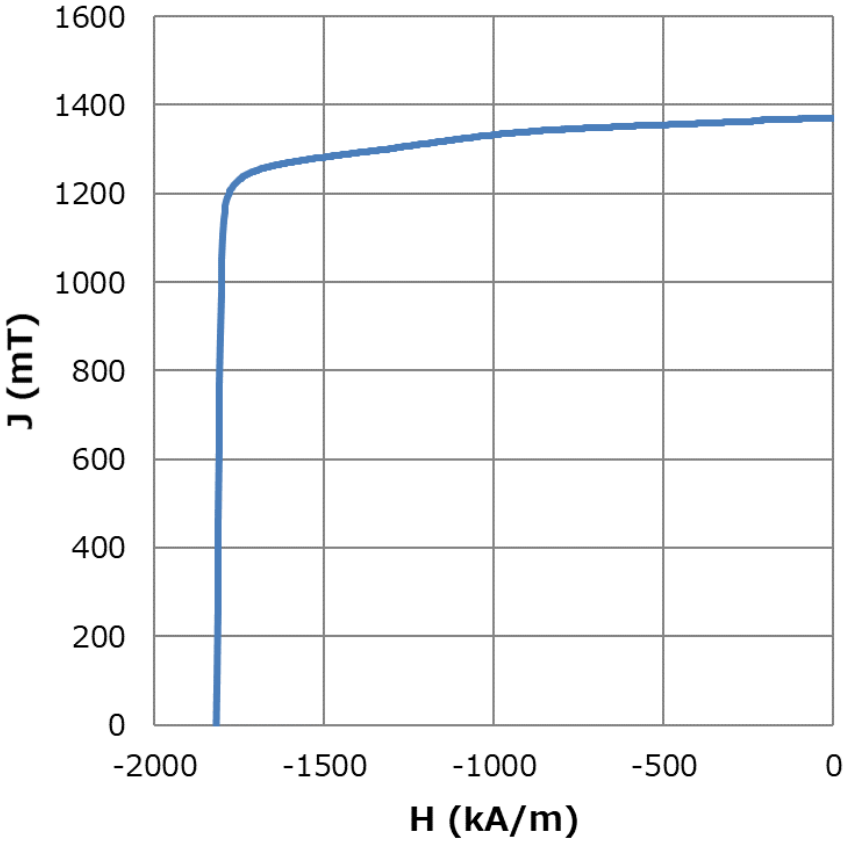

Figure 2-5 Demagnetization curve of developed specimen.

Most of the analyses discussed below were performed with this developed specimen. For comparison, a conventional specimen with the composition of 14at% TRE-Co-B-M-bal. Fe (M=Cu, Al, Zr), which showed a coercivity of 1080 kA/m, was also prepared.

Compared with a Nd-Fe-B magnet with a coercivity of 1830 kA/m containing 4 to 6 wt% Dy in general, the achieved coercivity without heavy rare earth elements substitution is remarkably high. The initial magnetization curve measured by a B-H tracer is shown in Figure 2-6. Since the average diameter of the starting powder was 2.5 μm, there's no step observed in this magnetization curve.

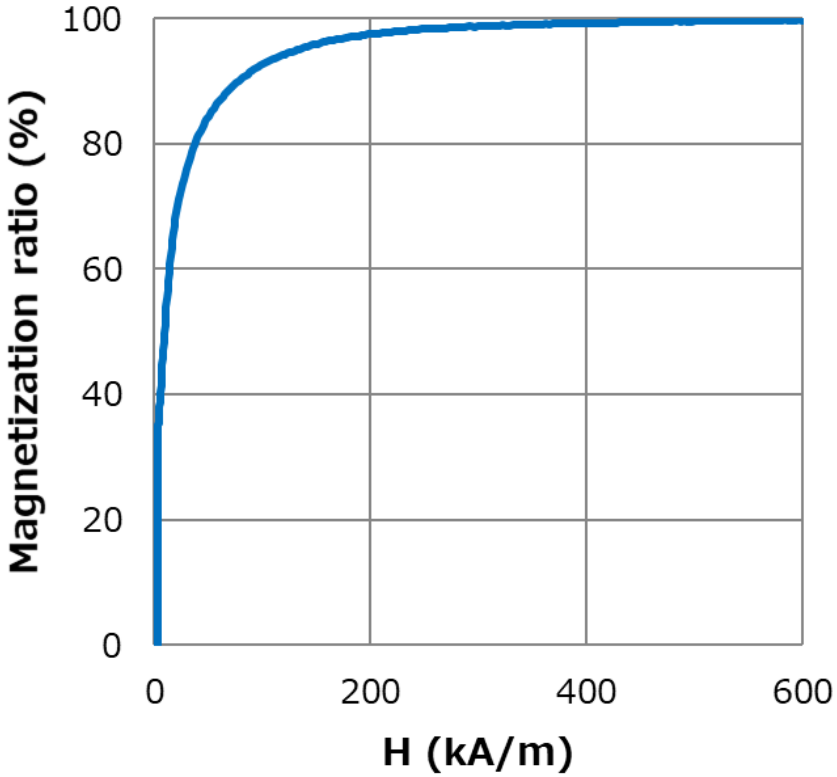

Figure 2-6 Initial magnetization curve for a magnet with a coercivity of 1830 kA/m.

The temperature dependence of coercivity was measured using mass production specimens which contain Dy as references. The result is shown in Figure 2-7. The coercivity at room temperature differs from sample to sample. The developed specimen shows a same or better temperature dependency to above 400 K and

the coercivity is slightly better than that of the commercial I specimen which shows higher coercivity at room temperature than developed. The temperature coefficient β of the coercivity was -0.64 K /%, -0.67 K /%, and -0.68 K /% (293-413 K) for the developed material, Commercial I material, and Commercial II material, respectively. From these results, the developed HREE-free Nd-Fe-B sintered magnet can be practical for industrial use.

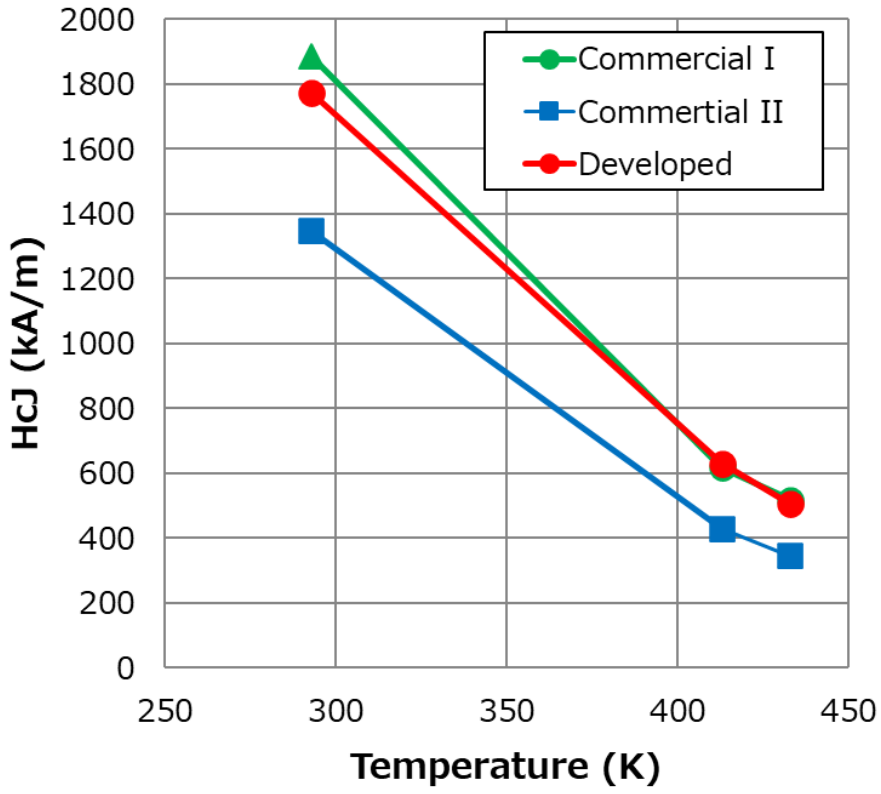

Figure 2-7 The temperature dependence of coercivity of an HREE-free sample compared with commercial samples as references.

2.3.3 Identification of grain boundary phase

The microstructures of the conventional and developed specimens were observed by SEM, as shown in Figure 2-8. The conventional magnet was prepared with the composition of 14 at% TRE-Co-B-M-bal. Fe (M=Cu, Al, Zr) using powder with an average diameter of 4.0 μm. As shown in Figure 2-8 (a), in the conventional specimen, a grain boundary is hardly observed between the grains but triple junctions are present. This is due to the fact that the grain boundary phase is thin (less than 20 nm at most, considering from the resolution of SEM image at this magnification) or almost non-existent. In contrast, in the developed specimen, a grain boundary is easily observed and is continuously connected to the triple junctions, as shown in Fig. 2 (b). In order to quantitatively judge how much the grains are surrounded by the grain boundary phase, the coverage ratio of grain was determined. The average value of how much the grain boundary of each grain is covered by the grain boundary phase recognizable in the SEM image was obtained by image analysis. Although the coverage varies depending on the image, the coverage ratio of the conventional specimen and the developed specimen was about 20% and 75%, respectively.

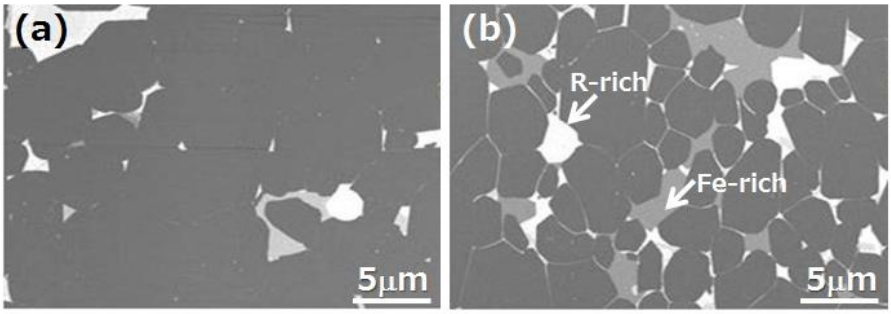

Figure 2-8 Cross-sectional images; (a) Conventional specimen and (b) Developed specimen.

Judging from the SEM contrast, several grain boundary phases coexist. The grain boundary phases were roughly identified by EPMA as R(Nd, Pr)-rich, Fe-rich and a small amount of RO_x phase. The existence of Ga was not recognized inside the grain. The Fe-rich phase is only observed in the developed specimen. The composition of these phases at the grain boundary was precisely investigated by using 3DAP.

Line profiles perpendicular to the thin grain boundary plane were extracted from the 3D mapping of the elements. A typical line profile across grain boundaries of conventional specimens, especially thin grain boundary phases that are difficult to observe with SEM, were measured, as shown in Figure 2-9. The bright line in Figure 2-9 (a) is the grain boundary. The width of the grain boundary is less than 5 nm. In principle, 3DAP cannot accurately estimate the distance along the length of a needle sample, the width estimated from 3DAP almost coincides with the observational result by FE-SEM (Field Emission SEM) without correction. The Fe content at the grain boundary region is slightly lower than that in the grains. Judging from the iron concentration, it is difficult to say that this grain boundary phase is non-magnetic. Although the concentration of R (Nd, Pr) was not constant between grain boundaries, most grain boundaries observed contained less than 30 at% R(Nd, Pr). Although the Nd-rich phase contains more Nd than the $Nd_2Fe_{14}B$ phase (11.8 at% Nd), it still contains more than 70% Fe, indicating the possibility of having a large magnetization.

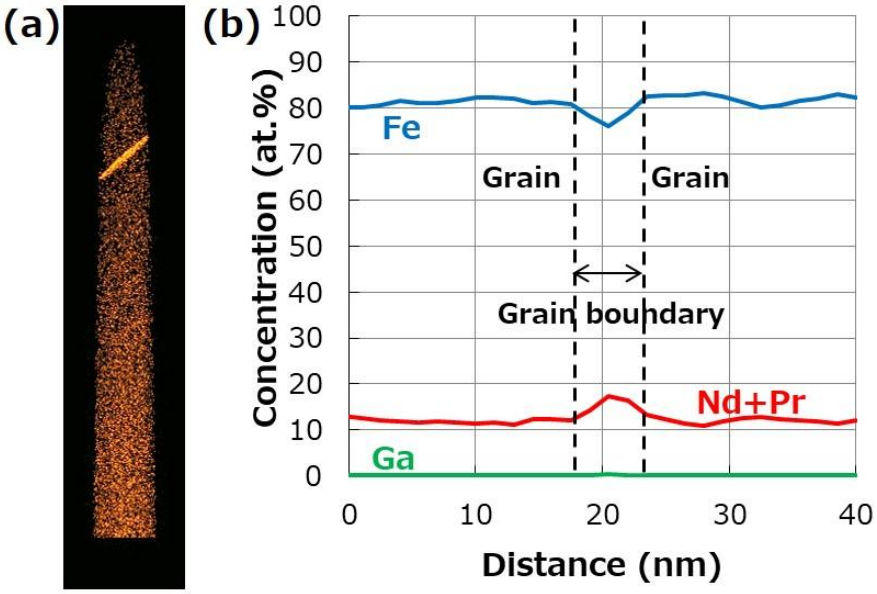

Figure 2-9 Compositional distribution at grain boundary of conventional specimen; (a) 3DAP mapping of Nd and (b) Line profiles across the grain boundary.

It is difficult to determine the minimum thickness of the grain boundary phase required to break the magnetic coupling between particles. The exchange length (L_{ex}) of the $Nd_2Fe_{14}B$ phase is around 2.1 nm, calculated from the equation below;

$$L_{ex} = \frac{A_{ex}}{\mu_0 \cdot {M_s}^2}$$

where A_{ex} and M_s are the exchange stiffness and saturation magnetization, respectively, however the dipolar interaction would remain because of its rather long-range interaction [74]. The domain wall width of $Nd_2Fe_{14}B$ is estimated to be about 5 nm experimentally [176], [177], and decoupling in a thinner region is expected to be difficult. Therefore, the thin grain boundary phase with high iron concentration as shown in Figure 2-9 may not be able to break the magnetic coupling between particles.

The line profiles of the bright and dark phases between two grains in the developed specimen were measured as shown in Figure 2-10. Both the grain boundary phases were thicker than that in the conventional specimen. The bright phase, which is R-rich phase, was composed of more than 95 at% R (Nd and Pr) and less than 5 at% Fe, as shown in Figure 2-10 (a). The concentration of R (Nd and Pr) varied with the observation point, and was roughly from 70 to 100 at%. In all cases, the concentration was much higher than that of the conventional specimen.

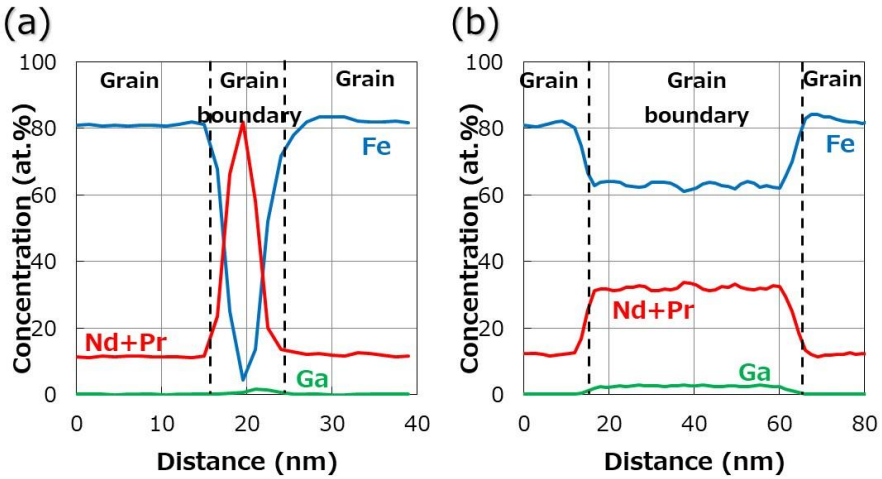

Figure 2-10 Compositional distribution at grain boundary of developed specimen; (a) Bright phase and (b) Dark phase.

Next, an attempt was made to identify the Fe-rich phase, which is observed as a dark area at the grain boundary. A composition profile of the dark grain boundary is shown in Figure 2-10 (b). The concentration of each element in the grain boundary phase is almost constant, being 30 at% R (Nd and Pr), 65 at% Fe and 5 at% Ga. The thin Fe-rich grain boundary was identified as the $R_6T_{13}M$ phase, which has a $La_6Co_{11}Ga_3$ crystal structure, as shown by its diffractogram in Figure 2-11.

From these, the dark grain boundary phase is considered to be the $R_6Fe_{13}Ga$ phase, where R is Nd and Pr. Hereinafter, the $(Nd, Pr)_6Fe_{13}Ga$ phase is conventionally referred to as $Nd_6Fe_{13}Ga$.

Both R-rich and $Nd_6Fe_{13}Ga$ phases are considered to be important for high coercivity, but the formation of the latter phase is unique to Ga added specimens. Therefore, the $Nd_6Fe_{13}Ga$ phase was investigated in detail.

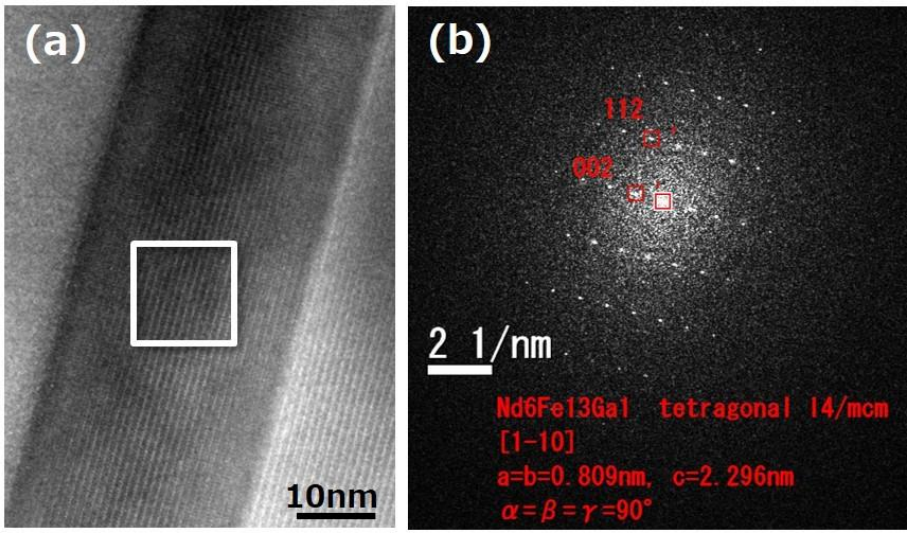

Figure 2-11 Diffractogram of Fe-rich phase at grain boundary;

(a) TEM image of Fe-rich phase and (b) Diffractogram taken at rectangular area in (a).

2.3.4 Effect of annealing on $Nd_6Fe_{13}Ga$ grain boundary phase

The characteristic of the developed specimen is that the $Nd_6Fe_{13}Ga$ phase constitutes a thick grain boundary, and this grain boundary phase is formed by annealing. Figure 2-12 shows SEM photographs of the developed specimens before and after annealing. There is no gray phase before annealing, i.e., $Nd_6Fe_{13}Ga$ phase, but a thick and clear $Nd_6Fe_{13}Ga$ grain boundary phase is formed after annealing.

Moreover, the white R-rich phase also forms thick and clear grain boundaries. The formation of these grain boundary phases was investigated.

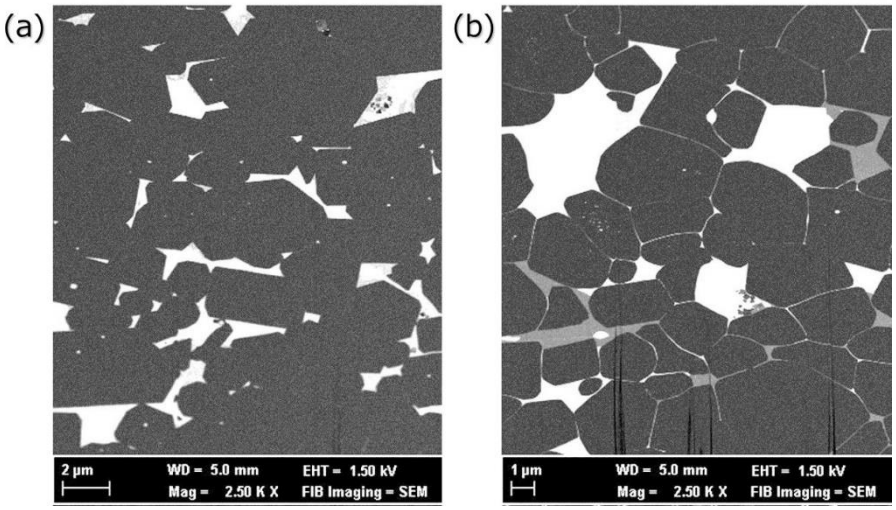

Figure 2-12 Cross sections of developed specimen;

(a) before annealing and (b) after annealing.

First, the relationship between the annealing temperature and magnetic properties was investigated. Two kinds of specimens, conventional composition without Ga and developed composition with Ga were prepared without annealing, and were then first annealed at 1073 K for 1 hour and second annealed at various temperatures for 1 hour, after which residual magnetic flux density and coercivity were measured, as shown in Figure 2-13.

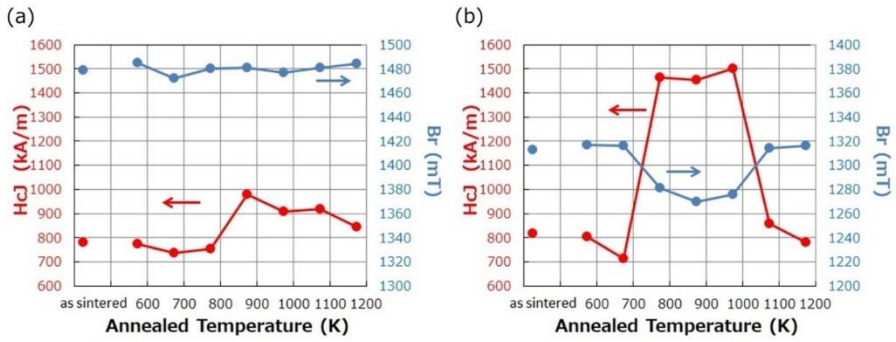

Figure 2-13 Annealing temperature dependence of magnetic properties;
(a) conventional Ga non added specimen and (b) developed Ga added specimen.

In the conventional specimen, the residual magnetic flux density hardly changed by annealing temperature, and the coercivity was improved by about 200 kA/m in the annealing temperature range of 800-1100 K. On the other hand, in the developed specimen, the residual magnetic flux density decreased and the coercivity increased dramatically to about 700 kA/m in the annealing temperature range of 700-1000 K.

Generally, the densification and phase formation of $Nd_2Fe_{14}B$ grains is completed in the sintering stage. Since the annealing procedure is performed at much lower temperatures than the sintering procedure, the $Nd_2Fe_{14}B$ main phase, which decides magnetization, does not change in the annealing stage as shown in Figure 2-13 (a). However, both the increase of coercivity and the decrease of magnetization occurred in the annealing stage for the developed specimen as shown in Figure 2-13 (b). This indicates that decomposition of the $Nd_2Fe_{14}B$ main phase and formation of $Nd_6Fe_{13}Ga$ grain boundary phase occurred simultaneously in this temperature range in Ga added specimen. The decrease of residual flux density is not observed below 700 K or above 1000 K. This means the $Nd_6Fe_{13}Ga$ grain boundary phase which affects coercivity is formed only in the limited temperature range between 700 K and 1000 K. The cross sections of the developed

specimens annealed at various temperatures are shown in Figure 2-14. A thick, continuous grain boundary phase is observed in the specimens annealed at 773 K and 973K, but this grain boundary phase between two grains becomes thinner and discontinuous at 1073 K.

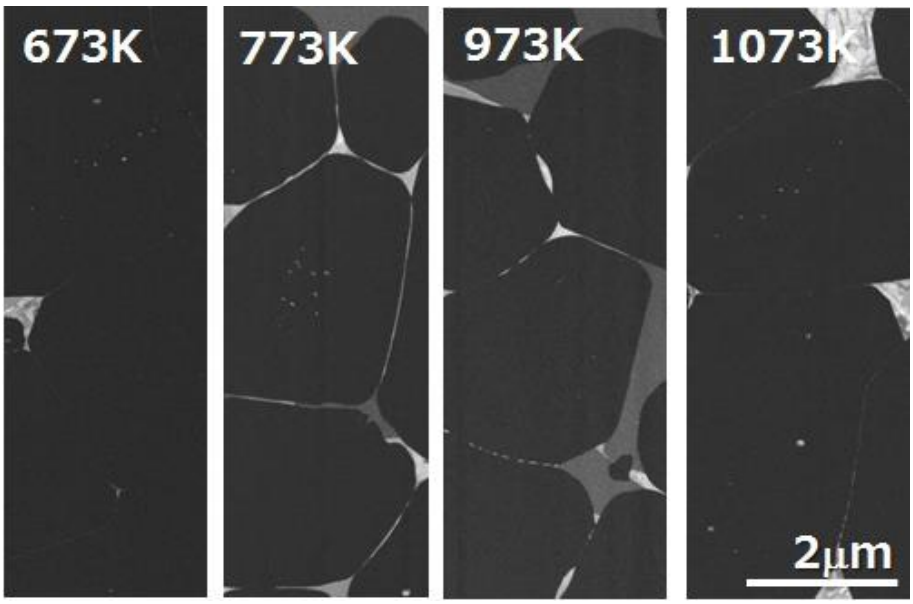

Figure 2-14 Cross sections of developed specimens annealed at various temperatures.

Next, the temperature range of grain boundary phase formation during annealing was investigated more directly, focusing on the $Nd_6Fe_{13}Ga$ phase. The temperature dependence of the XRD spectra in the developed specimen was investigated in detail. Due to the low intensity of the $Nd_6Fe_{13}Ga$ phase, synchrotron radiation was used.

The XRD profiles of the developed specimen without annealing were measured at high temperatures, as shown in Figure 2-15. The formation and annihilation of $Nd_6Fe_{13}Ga$ phase was successfully captured by XRD for the first time. At lower temperatures, there are no peaks which indicate the $Nd_6Fe_{13}Ga$ phase. The phase

appears between 800 K and 850K, but substantially disappears at 1075 K, probably because of decomposition. On the other hand, the peak of Nd-metal existing at room temperature disappears above 850 K, probably because of melting by a eutectic reaction with Cu.

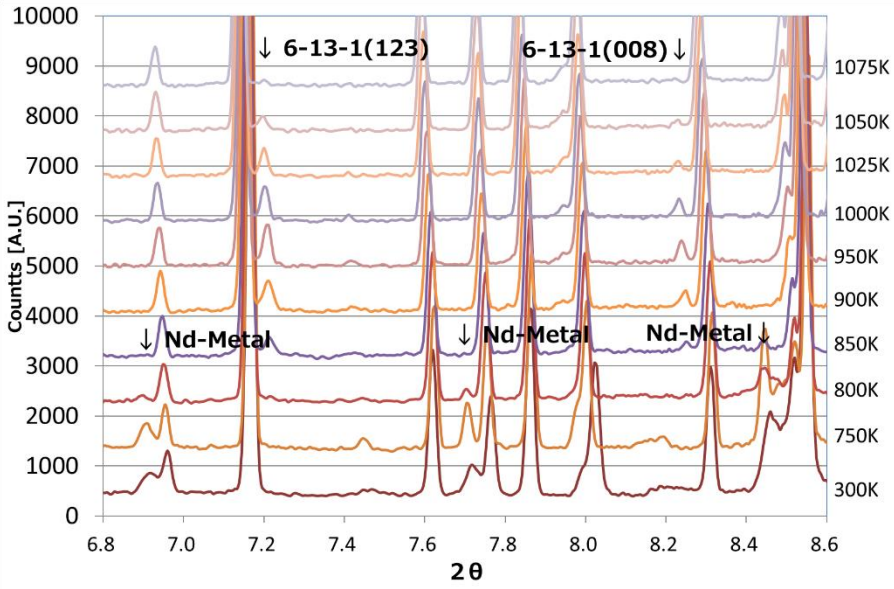

Figure 2-15 Temperature dependence of XRD spectra of developed specimen during heating.

After sintering (before annealing), the specimens were exposed once to the same temperature range as that exposed during annealing process though $Nd_6Fe_{13}Ga$ phase did not form after sintering. It was thought that the rapid cooling after sintering might make formation of the $Nd_6Fe_{13}Ga$ phase difficult. In order to confirm this, the specimen was once annealed to a high temperature at which the $Nd_6Fe_{13}Ga$ phase disappears, and then rapid-cooled at the cooling rate of -100 K/min. The XRD profiles are shown in Figure 2-16. When rapid cooling was applied, the $Nd_6Fe_{13}Ga$ phase did not form.

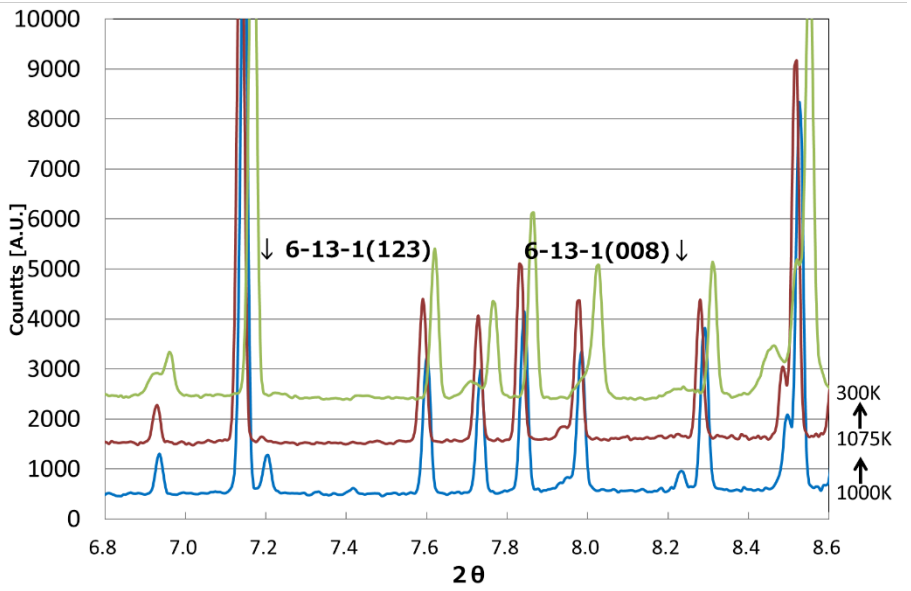

Figure 2-16 Temperature dependence of XRD spectra of developed specimen during rapid cooling.

These results indicate that the formation of the $Nd_6Fe_{13}Ga$ phase occurs in a certain limited temperature range and also requires a certain amount of time. Most importantly, the high coercivity temperature range shows good agreement with the $Nd_6Fe_{13}Ga$ phase formation range as shown in Figure 2-13. The slight difference in the temperature ranges for phase formation and for high coercivity could be caused by the difference in annealing time. Specifically, for measurement of magnetic properties, the specimens were annealed for 1 hour, while for XRD, annealing was performed for only 4 min at each temperature.

The relative temperature change of several main peak intensities of $Nd_2Fe_{14}B$ phases in XRD is shown in Figure 2-17. The peak intensity decreased with increasing temperature due to thermal fluctuation. There is a temporary increase in the rate of decrease at 700-800 K for all Miller indices. This is estimated to decrease with the decomposition of $Nd_2Fe_{14}B$ phases. Since this temperature range

was just below the formation start temperature of the $Nd_6Fe_{13}Ga$ phase, the results proved that the $Nd_6Fe_{13}Ga$ phase was formed using Fe after the decomposition of the $Nd_2Fe_{14}B$ phase.

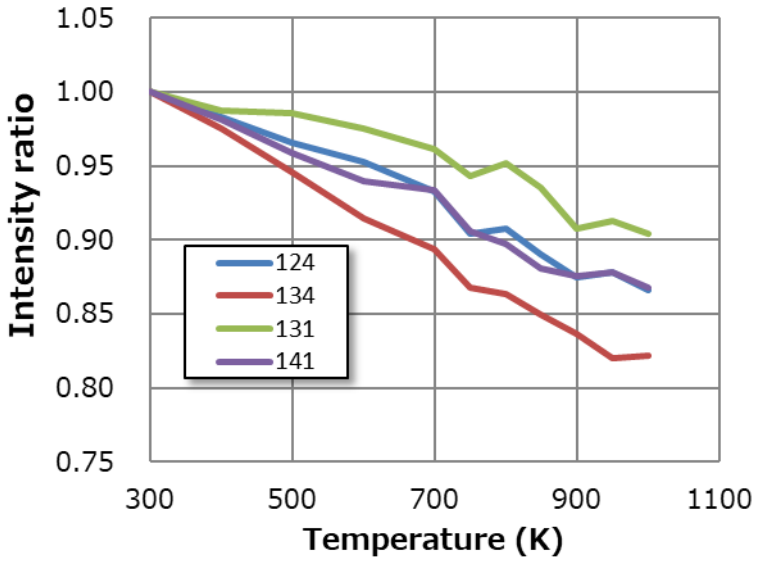

Figure 2-17 Main peak integrated intensities of $Nd_2Fe_{14}B$ as a function of temperature.

Figure 2-18 shows an example of a TEM photograph of the interface between $Nd_2Fe_{14}B$ and $Nd_6Fe_{13}Ga$. The facet growth of $Nd_6Fe_{13}Ga$ is observed for $Nd_2Fe_{14}B$. The NdCu-rich amorphous phase of about 1-2 nm exists between the two phases, and it is considered that the decomposed $Nd_2Fe_{14}B$ supplies Fe to the $Nd_6Fe_{13}Ga$ phase through this amorphous phase. Although not all grain boundaries observed were faceted, this helps to understand the crystal growth of $Nd_6Fe_{13}Ga$.

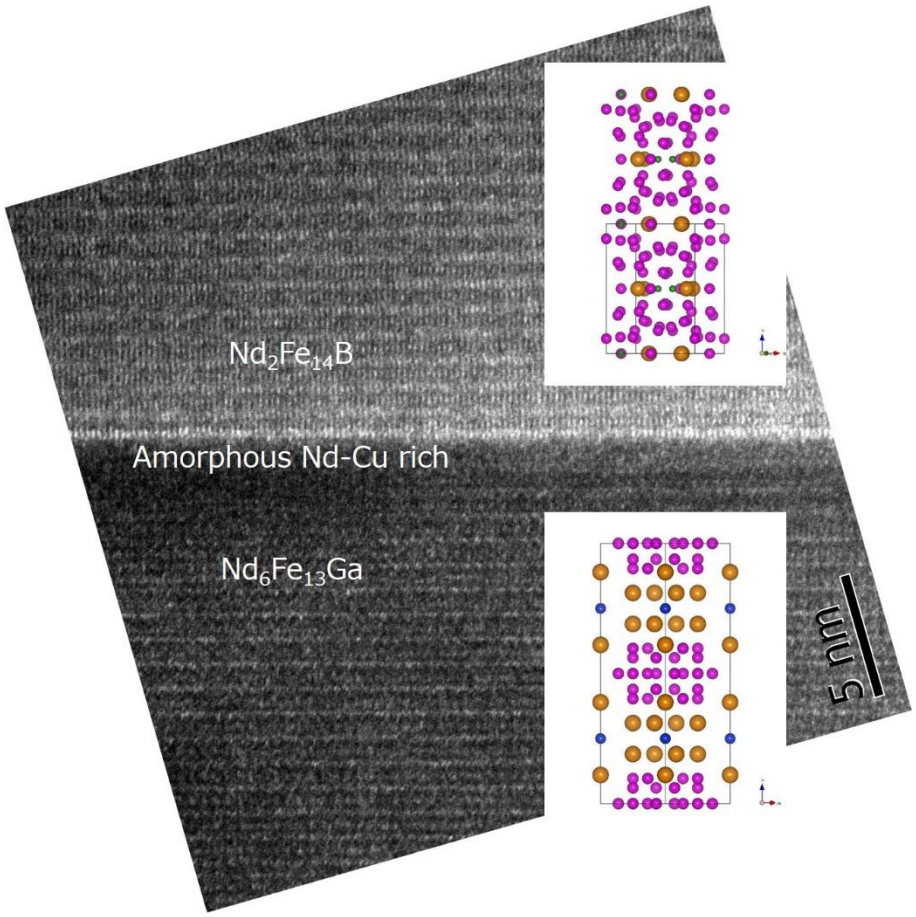

Figure 2-18 Cross section of interface between $Nd_2Fe_{14}B$ and $Nd_6Fe_{13}Ga$ phases.

From the above, the $Nd_6Fe_{13}Ga$ phase is considered to form during annealing by consuming Fe from $Nd_2Fe_{14}B$ grains and the R-rich phase. Decomposition of $Nd_2Fe_{14}B$ grains lowers residual flux density, while the formation of both $Nd_6Fe_{13}Ga$ phase and lower-Fe R-rich phase improves coercivity. Thus, formation of the $Nd_6Fe_{13}Ga$ phase occurs around the grain boundaries where Ga exists, and it accelerates the surface decomposition of $Nd_2Fe_{14}B$ grains.

As described above, a thick grain boundary phase of $Nd_6Fe_{13}Ga$ forms by annealing. In the conventional sintered magnets, the grain boundary phase is

formed by a passive mechanism in which the R-rich phase, which is a liquid phase at the annealing temperature, penetrates into grain boundaries from the triple junction by capillary action. However, in the developed magnets, it was found that the $Nd_6Fe_{13}Ga$ grain boundary phase is formed by a completely different mechanism in which the $Nd_6Fe_{13}Ga$ phase is formed by decomposing the surface of $Nd_2Fe_{14}B$ grain. Therefore, a thick grain boundary phase was easily formed in the developed magnet. Furthermore, the magnetization of the R-rich phase is expected to decrease due to the consumption of Fe in the surrounding R-rich phase by the formation of the $Nd_6Fe_{13}Ga$ phase.

2.3.5 Magnetism of grain boundary phases

For a high coercivity HREE-free Nd-Fe-B magnet, a non-ferromagnetic or low magnetic grain boundary is considered to be desirable. From this viewpoint, the magnetization of grain boundary phase was estimated at a triple junction because the grain boundary is so thin that it is difficult to estimate the magnetization of this region. Before conducting this experiment, the $Nd_6Fe_{13}Ga$ phase at the grain boundary was observed by TEM to find that the phase is crystalline and continuously connected to the dark area at the triple junction while keeping its lattice structure. Therefore, it is considered that the magnetism of the gray phase of the triple junction coincides with that of the thin grain boundary.

First, an electron holographic method was applied [108], [109]. The $Nd_6Fe_{13}Ga$ phase was cut away and thinned for TEM observations by using a focused ion beam (FIB) as shown in Figure 2-19. It can be seen that $Nd_6Fe_{13}Ga$ phases were successfully extracted from the three points and $Nd_2Fe_{14}B$ phases were successfully extracted from the grain.

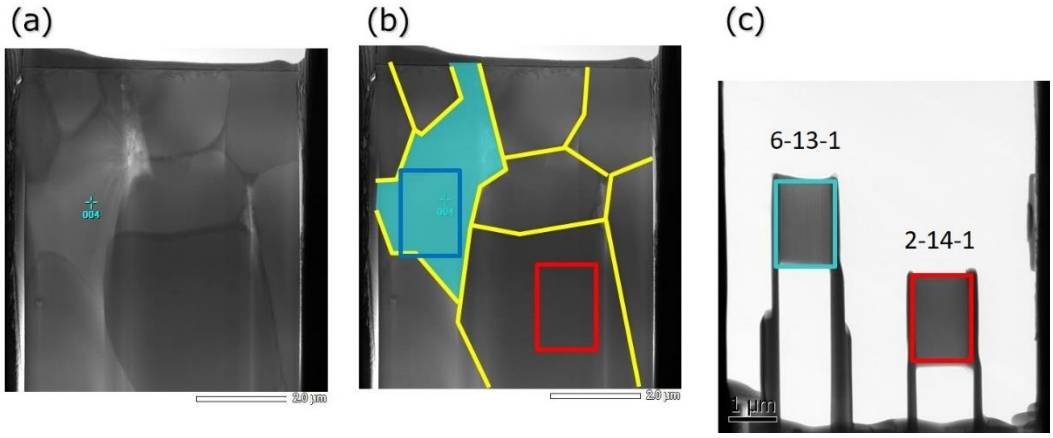

Figure 2-19 Sample preparation for electron holography; (a) SEM image of developed specimen, (b) Sampling location (blue and red squares) and grain boundary location (yellow line) and (c) Samples cut out by FIB (Left: $Nd_6Fe_{13}Ga$, Right: $Nd_2Fe_{14}B$)

A magnetic field was applied to this specimen, and its magnetization was estimated from the width of the interference fringes and the sample thickness with using the equation shown below.

$$B = \frac{h}{2\pi e} \cdot \frac{\Delta \emptyset}{S}$$

Where B is magnetic flux density, h is Planck's constant and e is the elementary charge, Δø is the phase change of electrons, S is the cross-sectional area. A holographic image was observed by using TEM.

A Holographic image of $Nd_2Fe_{14}B$ (right side of Figure 2-19) is shown in Figure 2-20 (a). A holographic pattern due to spontaneous magnetization of $Nd_2Fe_{14}B$ are observed. The magnetization calculated from the holographic pattern was 0.96 T. From the actual magnetization 1.6 T of $Nd_2Fe_{14}B$, the demagnetizing factor in this sample shape was determined to be 0.60. Figure 2-20 (b) shows the holographic pattern of $Nd_6Fe_{13}Ga$. Since a small part of the $Nd_2Fe_{14}B$ phase remains in the prepared specimen, non-uniform interference fringes are observed. It is considered

that the magnetization inside $Nd_6Fe_{13}Ga$ is weak and weakly magnetized by the external magnetic field from the neighboring $Nd_2Fe_{14}B$ rather than the spontaneous magnetization. From the demagnetization factor determined by $Nd_2Fe_{14}B$, it was estimated that the magnetization of the $Nd_6Fe_{13}Ga$ sample was about 0.05 T, calculated from the difference of the interference fringes inside and outside the specimen. Although the $Nd_6Fe_{13}Ga$ phase contains as much as 65 at% of Fe, it showed quite low magnetization compared to 1.6T of $Nd_2Fe_{14}B$. The results were summarized by the authors [18], and Niitsu et al.'s later study also confirmed that the $Nd_6Fe_{13}Ga$ phase is almost paramagnetic [178]–[180].

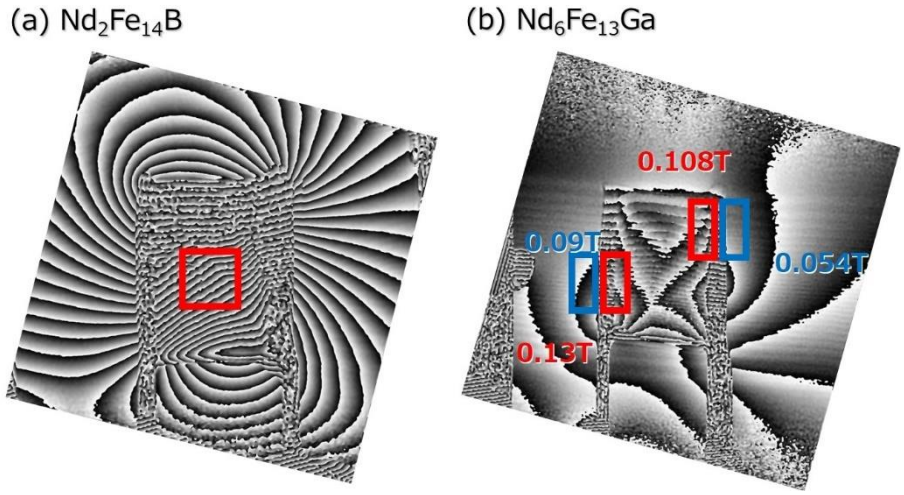

Figure 2-20 Electron holographic measurement of
(a) $Nd_2Fe_{14}B$ phase and (b) $Nd_6Fe_{13}Ga$ phase at triple junction.

To investigate magnetization more easily, a STEM-Lorentz method was applied [181]. Magnetization was calculated from the Lorentz polarization angle and the sample thickness. A schematic diagram of the STEM-Lorentz method is shown in Figure 2-21.

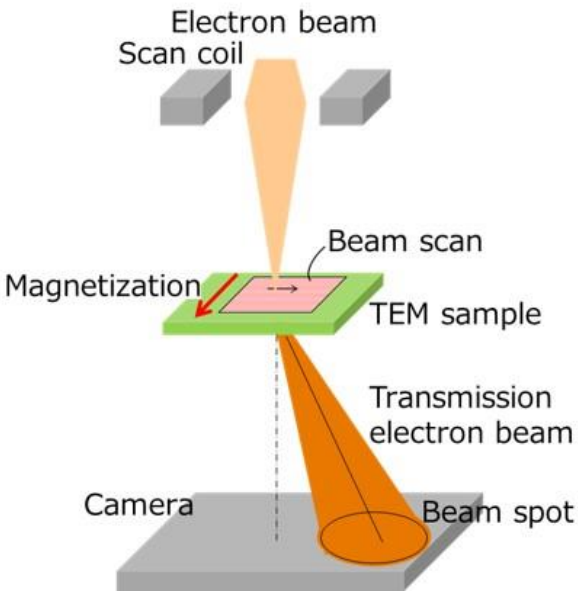

Figure 2-21 A schematic diagram of the STEM-Lorentz method.

A sample containing a target grain boundary was cut out by FIB, and a sample having a thickness of about 100 -150 microns was prepared. The sample thickness was accurately measured using electron energy loss spectroscopy (EELS). When a sample with magnetization is exposed to an electron beam using a Lorentz-TEM, the angle of the electron beam changes due to the Lorentz force. From this angle, the amount of magnetization can be estimated. In this case, the magnetization amount is expressed by the following equation.

$$\beta = eBt\frac{\lambda}{h}$$

Here, β is a deflection angle, B is a magnetic flux t is a sample thickness, λ is a wavelength, h is a Planck constant, and e is an element charge.

The direct spot of the diffracted image was mapped in synchronization with the scanning of the STEM image with the magnetic field of the objective lens weakened. At this time, the position of the direct spot at each point of the scanning region was changed by receiving Lorentz deflection. This change was quantitatively analyzed as a Lorentz deflection vector, and a magnetic flux vector diagram in the material was visualized. Figure 2-22 shows STEM-Lorentz observations of $Nd_2Fe_{14}B$ particles. As a result, the magnetization of the $Nd_2Fe_{14}B$ particle is estimated to be 1.5-1.6 T, which is not much different from the actual value. From this result, it is concluded that magnetization estimation by STEM-Lorentz method is possible.

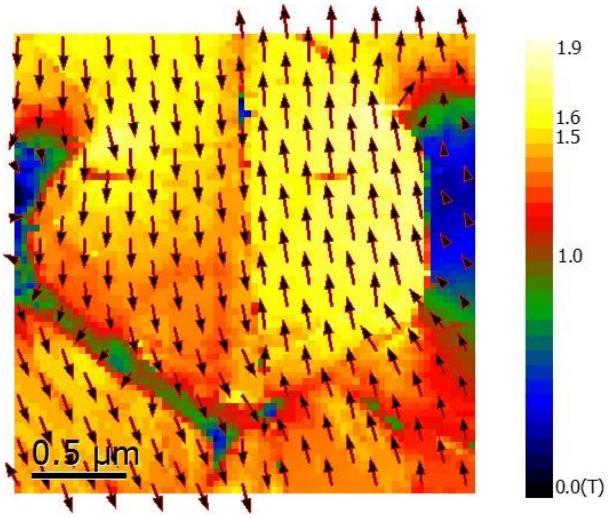

Figure 2-22 STEM-Lorentz measurement of $Nd_2Fe_{14}B$ grain.

The line profile of magnetization across the $Nd_6Fe_{13}Ga$ phase is shown in Figure 2-23. By using this method, the magnetization of the $Nd_6Fe_{13}Ga$ phase at the triple junction was estimated to be 0.04-0.06T, which showed good agreement with the holographic result.

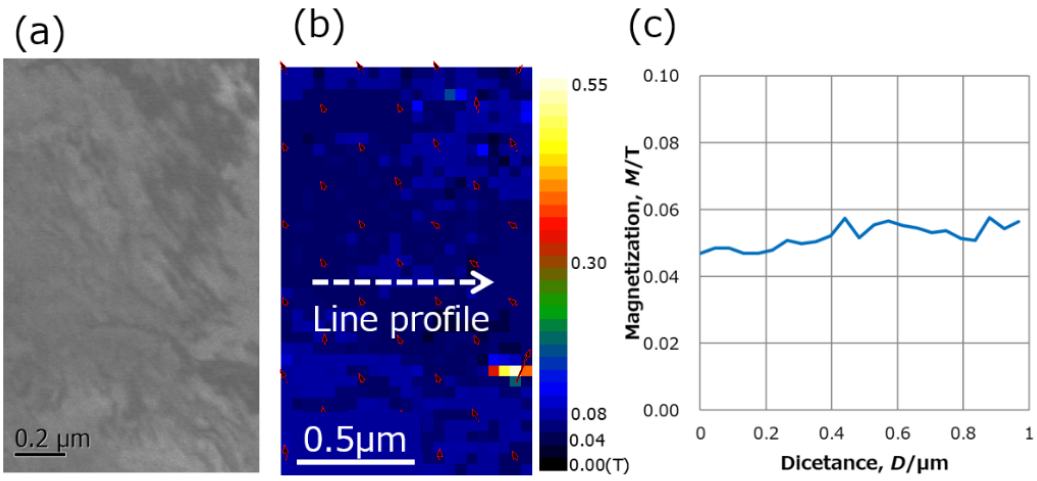

Figure 2-23 STEM-Lorentz measurement of $R_6T_{13}M$ phase; (a) STEM image, (b) Magnetization map and (c) Line profile of magnetization extracted from map (b).

Another grain boundary phase which is important for the coercivity of HREE-free Nd-Fe-B magnets is the R-rich phase. Hono et al. reported that the composition of R-rich phase was determined to $Nd_{30}Fe_{66}B_3Cu_1$ by 3DAP measurement and the magnetic properties of the same compositional thin film was measured and found to be amorphous and ferromagnetic with the range of $\mu_0 M \approx 0.4$ T [18], [76], [79]. While the R-rich phase in the developed specimen contains 70 to 100 at% R (Nd and Pr) as shown in Figure 2-10 (a), the magnetization of the phase is considered to be much lower.

Therefore, the magnetization of the R-rich phase was estimated. Nd-Fe ingots with different composition ratios were prepared, and rapidly cooled meltspun was prepared at a peripheral speed of 40 m/s. The saturation magnetizations were measured, and the phases were identified by XRD. These are shown in Figure 2-24.

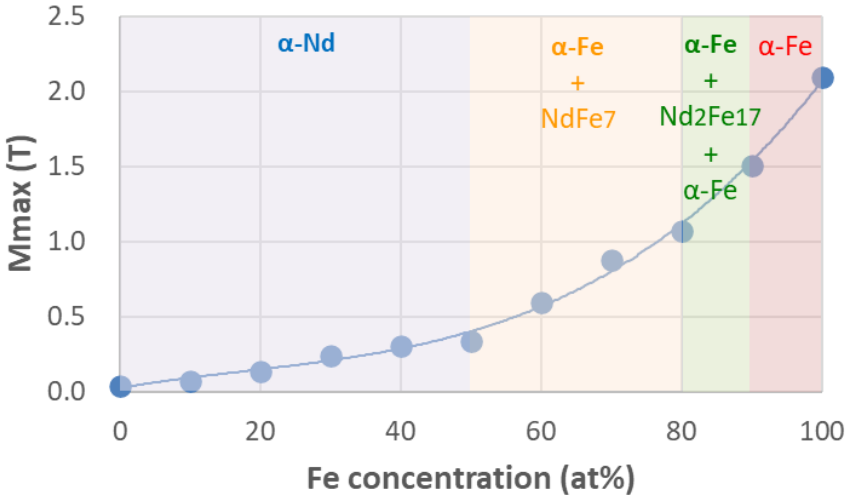

Figure 2-24 Saturation magnetization and identified phases of Nd-Fe meltspun.

Since the quenching condition is different from the actual grain boundary cooling condition and the actual sintered magnet contains various additives (Co, Cu, Al, Zr and Ga), this result does not accurately reflect the actual grain boundary composition, but it is considered to help to understand the magnetization of the R-rich phase. From XRD measurements, it was found that α-Nd (+ amorphous phase) was formed in the region of Fe concentration 50% or less, α-Nd + $NdFe_7$ phase [18] was formed in 50-80%, and α-Nd + Nd_2Fe_{17} phase + α-Fe was formed in 80-90%. The magnetization gradually increased with increasing Fe concentration, and the change of magnetization did not change greatly even if the phase changed. Since the Fe concentration of the R-rich phase of the developed magnet was 0-30 at%, the magnetization of the R-rich phase was expected to be 0.25 T or less. Since the magnetization is smaller than 0.4 T which is the magnetization of the R-rich phase of the conventional magnet, it is considered that not only the $Nd_6Fe_{13}Ga$ phase but also the R-rich phase contributes more strongly to the magnetic isolation of the particles.

From these results, both the R-rich and $Nd_6Fe_{13}Ga$ phases in the developed specimen are considered to have much lower magnetization compared to 1.6 T of the $Nd_2Fe_{14}B$ phase. These phases can exist at a grain boundary and decouple the exchange interaction between $Nd_2Fe_{14}B$ grains effectively.

2.3.6 Increase of grain boundary phase

The introduction of the $Nd_6Fe_{13}Ga$ phase suggests the possibility of forming a thick grain boundary phase with low magnetization. On the other hand, another simple method for forming a thick grain boundary, which helps to separate the magnetic coupling between each grain, is merely increasing the total content of the grain boundary phase.

Specimens with different TRE concentrations of 14.5 to 17.3 at% were prepared. The magnetic properties of these specimens are shown in Figure 2-25. Higher coercivity was obtained with higher TRE concentration. The specimen with 17.3 at% R(Nd, Pr) showed magnetic properties of Br=1181mT and HcJ=1998kA/m. Coercivity of higher than 1990 kA/m without using heavy rare earth elements is remarkably high, considering the fact that a general Nd-Fe-B magnet requires from 6 to 8 wt% Dy to meet a similar requirement. This value of coercivity is 35% of the anisotropy magnetization (H_{cJ}/H_A), which is much larger than that of a typical Nd-Fe-B magnet (as described in Appendix section), 15%.

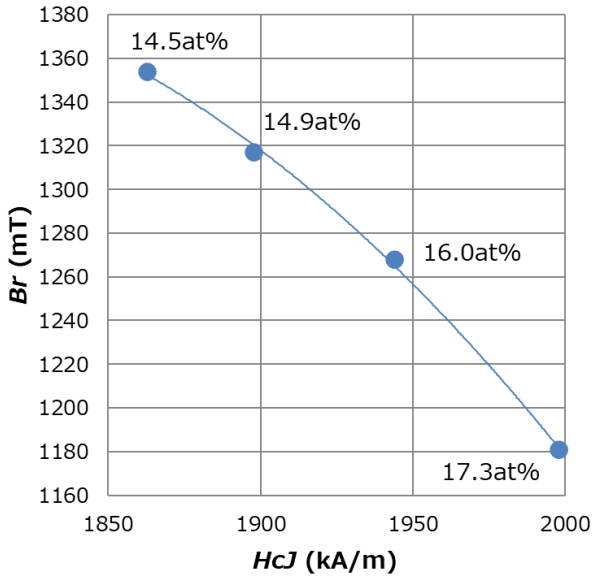

Figure 2-25 Magnetic properties of developed Dy-free Nd-Fe-B magnets with increased amount of grain boundary phase.

A cross-sectional image of the specimen is shown in Figure 2-26. Most grains are clearly separated by thick grain boundary phases. As the amount of TRE increases, the grain boundaries become thicker. However of course, the increase in the amount of grain boundary phase decreases the main phase ratio, resulting in a decrease in the residual flux density.

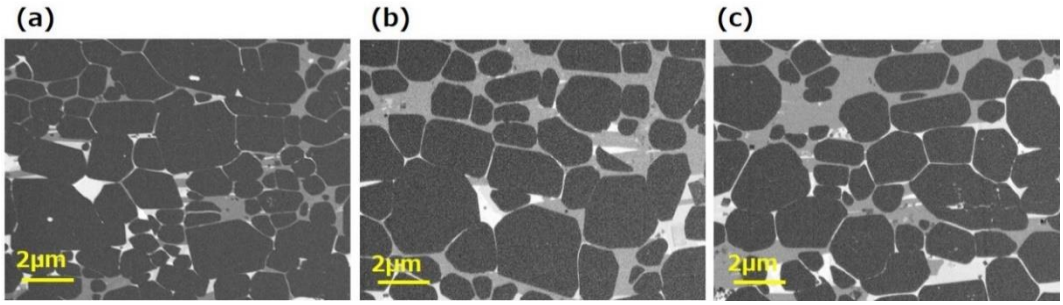

Figure 2-26 Cross section of specimen;

(a) 14.5 at% TRE, (b) 16.0 at% TRE and (c) 17.3 at% TRE.

The increase in the grain boundary phase does not necessarily mean a thicker grain boundary. The excess R-rich phase tends to accumulate at triple junctions, where it does not contribute to thicker grain boundary phases, although the existence of the $Nd_6Fe_{13}Ga$ grain boundary could help to impede the accumulation at triple junctions. For decoupling of the exchange interaction between $Nd_2Fe_{14}B$ grains, both grain boundary thickness and grain boundary continuity are considered to be important.

Therefore, the coverage ratio of $Nd_2Fe_{14}B$ grains by grain boundary phases containing both R-rich and $Nd_6Fe_{13}Ga$ phases was investigated by image analysis. The sample composition examined here is (14.0-17.3) at% TRE-Co-B-M-bal. Fe (M=Cu, Al, Ga, Zr). The results are shown in Figure 2-27. A good correlation between the coverage ratio and coercivity is observed. Moreover, as coercivity is still not saturated at a coverage ratio of 89%, further improvement may be expected.

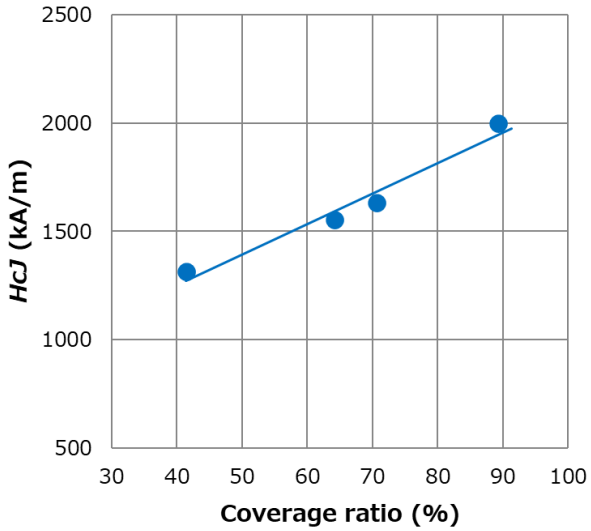

Figure 2-27 Relationship between coverage ratio, ratio of grains covered by grain boundary phase and coercivity.

2.3.7 Increase of Ga content

The effects of Ga addition on the formation of the $Nd_6Fe_{13}Ga$ phase and the reduction of Fe content in the R-rich phase have already been described. Then, how the quantity of the phase changed was examined. Several specimens with different coercivities prepared in the past were subjected to image analysis to investigate the amount of phases and the coverage. The results are shown in Figure 2-28.

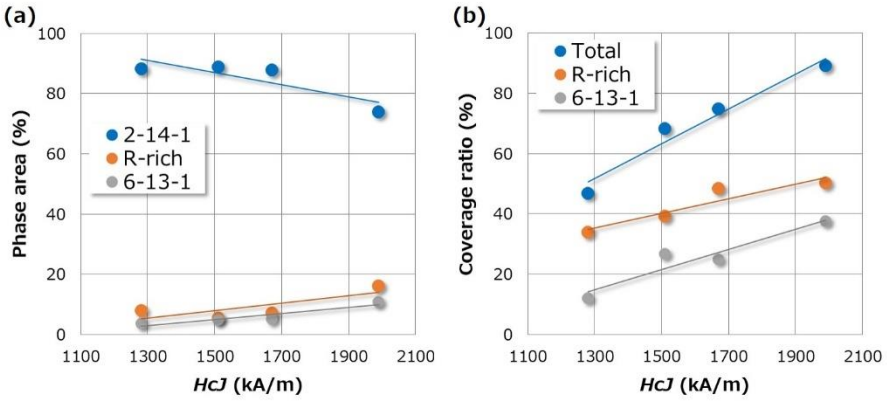

Figure 2-28 Image analysis of magnets with different coercivity (Ga concentration of 0.2, 0.4, 0.5, and 0.6 at%); (a) amount of phase and (b) coverage ratio.

In Figure 2-28, the relationship between the Ga addition amount and the coercivity agrees, and the Ga addition amount is 0.2, 0.4, 0.5, and 0.6 at%. However the other compositions did not necessarily change in a systematic manner. Therefore, although it is difficult to make an accurate comparison, it is possible to obtain a guideline for the structure of a magnet with a large coercivity. Considering the amount of phase, it is necessary to increase the amount of grain boundary phase to achieve high coercivity.

As the amount of Ga is increasing, it is natural that the $Nd_6Fe_{13}Ga$ phase is increasing, but the R-rich phase is also increasing accordingly. Furthermore, not only the coverage by the $Nd_6Fe_{13}Ga$ phase increases, but also the coverage by the R-rich phase increases. Even though the R-rich phase is only slightly larger than the $Nd_6Fe_{13}Ga$ phase in terms of the amount of phase, the coverage ratio is much larger than that of the $Nd_6Fe_{13}Ga$ phase. This suggests that the formation of the $Nd_6Fe_{13}Ga$ phase facilitates the penetration of the R-rich phase into grain boundaries from triple junctions. A cross section of the grain boundary phase where both grain boundary phases coexist is shown in Figure 2-29. As mentioned,

$Nd_6Fe_{13}Ga$ phase formed at grain boundary with decomposing the surface of $Nd_2Fe_{14}B$ grains. This is expected to create gaps between the particles and facilitate the penetration of the liquefied R-rich phase at the annealing temperature. In other words, the formation of the $Nd_6Fe_{13}Ga$ phase has the effect of promoting the grain covering by the R-rich phase.

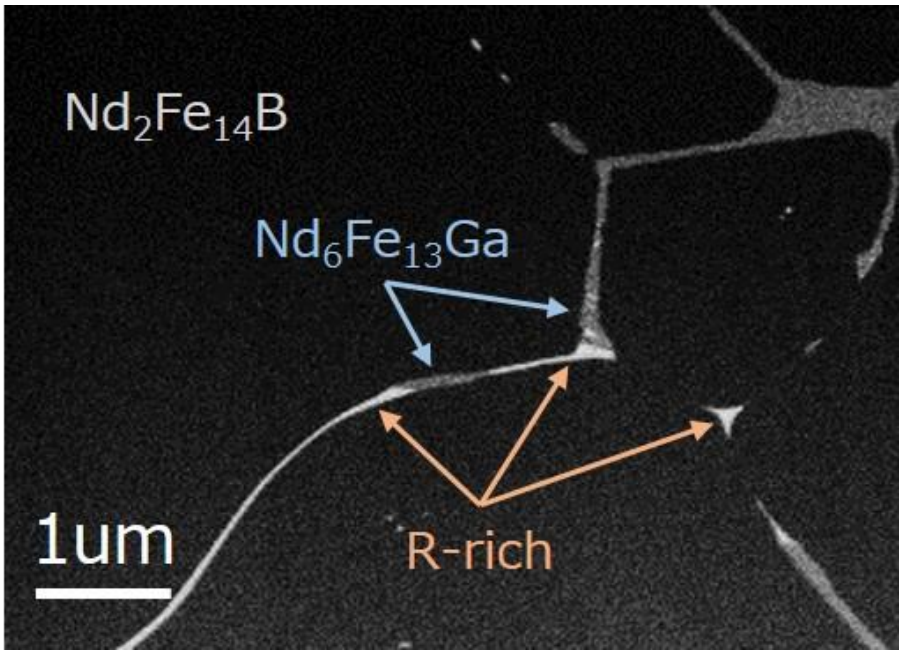

Figure 2-29 Coexistence of R-rich and $Nd_6Fe_{13}Ga$ phases.

2.4 Conclusion

In order to reduce the use of scarce heavy rare earth elements, such as Dy and Tb, the realization of sintered magnets with high coercivity without using heavy rare earth elements were examined. Coercivity of 1998 kA/m was achieved in a Nd-Fe-B sintered magnet without using Dy and Tb which is much higher than our target coercivity of 1592 kA/m. In order to decouple the exchange interaction

between $Nd_2Fe_{14}B$ grains, a thick and continuous grain boundary phase with low magnetization is important. A $Nd_6Fe_{13}Ga$ phase was introduced by adding Ga and the existence was also confirmed as thin grain boundary phase. The $Nd_6Fe_{13}Ga$ a phase is considered to form in a limited temperature range by consuming Fe from $Nd_2Fe_{14}B$ grains and the R-rich phase. The magnetization of the $Nd_6Fe_{13}Ga$ phase was estimated to be 0.05 T, which is much smaller than that of the $Nd_2Fe_{14}B$ main phase. The coverage ratio of $Nd_2Fe_{14}B$ grains by grain boundary phases affects the coercivity of the HREE-free Nd-Fe-B sintered magnet. The introduction of the $Nd_6Fe_{13}Ga$ phase is considered to contribute to the reduction of the magnetization of the R-rich phase. Thus, both grain boundary phases play important roles in achieving high coercivity in HREE-free Nd-Fe-B magnets.

Assuming the 2400 kA/m EV/HEV magnet with 10 wt% Dy described in Section 1.6, an equivalent result of 7.5 wt% reduction in Dy, or 75% reduction in HREEs, is achieved because the Dy-free composition achieved a coercivity of 1998 kA/m, which is equivalent to the addition of 7.5 wt% Dy. Since the same effect can be obtained even if Dy is Tb, it was concluded that 75% reduction of Dy and Tb was successfully achieved by this method considering from the criteria mentioned in Section 1.6. Nd-Fe-B magnets incorporating the $Nd_6Fe_{13}Ga$ phase have been mass-produced in TDK Corporation and widely used for automobile applications.

* Some of the results in this chapter were summarized in a paper [108].

Chapter 3 Microstructural design of Ce-added grain boundary phase for Nd and Pr reduction

3.1 Introduction

Various rare earth elements can take an $R_2Fe_{14}B$ structure as listed in Table 1-1 however only Nd, Pr, Dy and Tb have been widely used for mass-production magnets because of their high magnetization and coercivity. In Chapter 2, the reduction of heavy rare earth elements were discussed, but it is not only heavy rare earth elements that have resource problems. If we can use other “surplus” rare earth elements in Nd-Fe-B magnets, we can significantly reduce the rare-earth resource problem.

In addition, the imbalance between supply and demand of Nd resources has become a problem with the increase in production of electrified vehicles. Nikkei Asian Revies reported that Toyota Motor Corporation announced that “The supply of rare earths tends to shift as environmental regulations in that country change, creating uncertainty at a time when demand for those elements is set to rise with the popularity of electric vehicles. Even Toyota's most optimistic projections point to a neodymium shortage in 2025”[2] If this is true, reducing neodymium use is urgent for global development. It is necessary to reduce not only heavy rare earth elements but also neodymium, which is the root of Nd-Fe-B magnets.

For this purpose, the substitution of Nd with other more abundant rare earth elements have investigated to maintain high magnetic properties. Considerable

[2] https://newsroom.toyota.eu/download/514805/development-of-nd-reduced.pdf

time and number of experiments are required to investigate many composite compositions. In order to shorten this period as much as possible, the thin film combinatorial chemistry method was adopted as a technique of the High-throughput experiment. The candidate compositions were narrowed down by this method and developed into bulk experiments (sintered magnet). In the case of sintered magnets, not only the composition but also the microstructure has a great influence on the magnetic properties especially on coercivity, so the microstructure control was also investigated. This will be described in detail below.

3.1.1 Combinatorial chemistry

Although there have been many studies on substitution, the complex substitution of Nd by abundant rare earth elements has not been studied much. An increase in the number of experiments due to an increase in the number of substituted elements makes it difficult to investigate complex additions. In fact, this is probably the reason why the substitution of Nd by more abundant rare earth elements has been studied mainly by melt spun and less by sintered magnets as described in Section 1.5. For further research, the simultaneous substitution by multiple rare earth elements can be studied but it requires huge amount of experiments because of the combination of elements. In order to carry out the simultaneous substitution experiment more efficiently, the combinatorial chemistry method [182] was introduced. For the high-throughput experiment, the composition search was carried out by the thin film magnet instead of the bulk.

Combinatorial chemistry has developed since 1990s at first in a pharmaceutical field [183], [184] and it was applied for materials science field [185]–[189]. The sputtering and measurement system of composition gradient thin films and their magnetic properties of multiple-substituted $R_2Fe_{14}B$ thin film magnets were studied

in order to find candidate combination of substitution elements for bulk sintered magnet.

3.1.2 Bulk magnet

By applying the compositional studies from combinatorial chemistry, sintered magnet with 50 % Nd substitution was studied with the goal of achieving both good magnetic properties at a reasonable cost. Since the characteristics of sintered magnets are strongly dependent on not only composition but also microstructure, especially grain boundary control was studied. Since the magnetism of the grain boundary phase strongly affects the coercivity, the analysis of the phases was carried out as in Section 2.3.5. In particular, attention was paid to the magnetism of the grain boundary phases of both $R_6Fe_{13}Ga$ and RFe_2.

In this chapter, expressions such as $R_2Fe_{14}B$ or $R_6Fe_{13}Ga$ are used, where R represents a plurality of rare earth elements. In particular, it is used when elements other than Nd, Pr, Dy, and Tb, which are four elements usually used in Nd-Fe-B magnets, are contained.

3.2 Experimental procedure

3.2.1 Thin film preparation

The pseudo ternary composition gradient thin films were prepared by a combinatorial sputtering system (CMS-6400, Comet Inc.). The machine is a depo-up type sputtering machine which equips six sputter guns with shutters for layer-by-layer deposition. A 2-inch substrate is covered by fixed and moving masks.

Schematics of film preparation is shown in Figure 3-1. For the deposition of a composition gradient thin film, the mask moved over the substrate linearly during deposition in the unit layer. Then the deposited thickness changed linearly. After the deposition, the substrate rotated 120° followed by a next deposition by another sputtering gun. With repeating these procedures, an equilateral triangle thin film which has composition gradient was prepared.

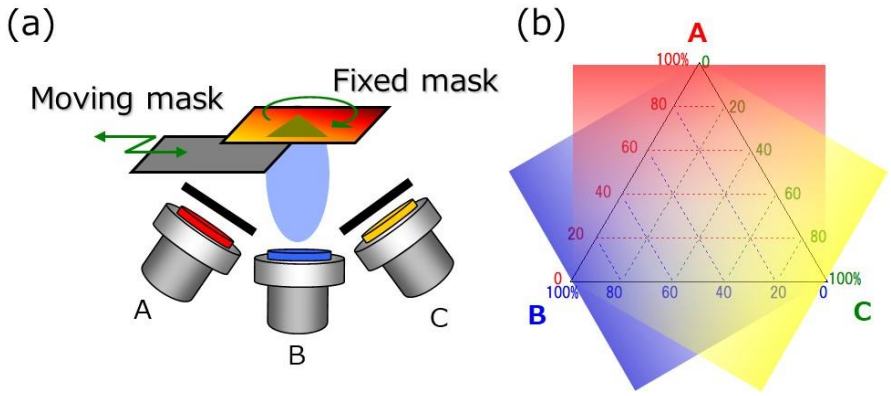

Figure 3-1 Schematics of thin film preparation;

(a) equipment configuration and (b) composition gradient thin film.

In order to measure B-H characteristics, multiple single composition thin films were also prepared at one time. By repeating movements and stops of the mask with covering sputter guns by shutters during mask movement, the thickness of the deposited layer changed stepwise. This process was repeated three times followed by the substrate rotation of 90°. With repeating these procedures, nine different single composition thin films, which was a matrix of 3 x 3 compositions, were deposited. The picture of fixed matrix mask is shown in Figure 3-2.

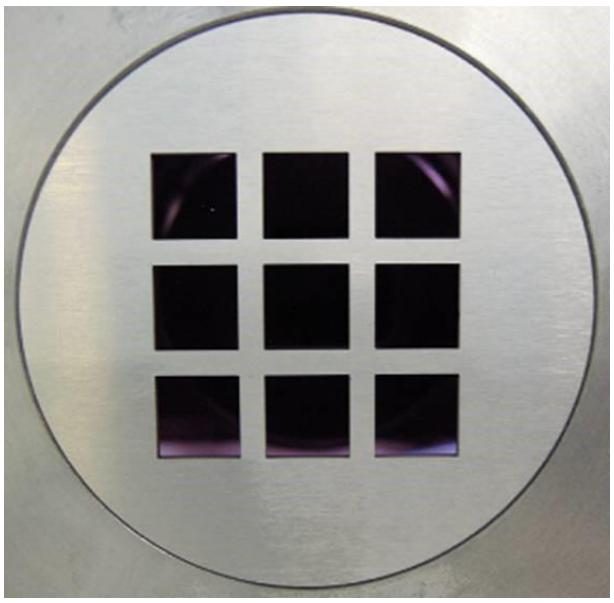

Figure 3-2 Fixed matrix mask for 3 x 3 compositions thin films.

Thermally oxidized silicon substrates were prepared. They were coated with Ta or Mo as a bottom layer and heated during sputtering. After the deposition of magnet thin film, cover layer was deposited with Ta or Mo.

3.2.2 Magnetic properties measurement of thin film

The surface leakage magnetic flux was measured with using a nano Magnetic Domain Scope (nano-MDS, TDK Corporation) [190], which was developed in house for this experiments, for all over the thin film. The apparatus equips a tunnel magneto resistance (TMR) sensor and piezoelectric driven x-y stage. Coercivity was measured by using a magneto-optical effect measurement system (BH-810CPC, Neoark Corporation) [191]. M-H characteristics were measured with using a vibrating sample magnetometer (VSM, Tamakawa, TM-VSM331483) and measurement of perpendicular to the substrate direction were performed. For VSM measurements, film thickness values were estimated from the film deposition rate

which was previously measured with a stylus type profilometer (Dektak 3030ST, Veeco).

3.2.3 Bulk magnet preparation

All the raw alloys were produced using a strip-casting method based on preparation compositions of (14.3-17.6) at% TRE (total rare earth)-Co-B-M-Bal. Fe (M=Cu, Al, Ga, Zr). The rare-earth elements contained in the alloys were 50 % Nd, with the other 50 % being made up of Y and Ce.

The raw alloys were coarsely pulverized by a hydrogen grinding method followed by fine pulverization by jet milling to obtain fine powders with an average diameter of 2.0–4.0 μm. The powders were placed in a magnetic field of 1600 kA/m to produce compacts. The compacts were then sintered in a vacuum for 4 h at a temperature ranging from 1213–353 K, and were then annealed for 1 h at 1173 K followed by a second annealing for 1 h at 913–1013 K to obtain the highest coercivity. The pulverizing, pressing, and sintering processes were performed in a low-oxygen atmosphere of less than 50 ppm.

3.2.4 Bulk magnet measurement

The magnetic properties of the specimens were measured using a BH tracer (Tamakawa Co., Ltd.) or a vibrating sample magnetometer (VSM, Tamakawa, TM-VSM331483). Analyses of the microstructure and crystal structure were performed by focused ion beam-scanning electron microscopy (FIB-SEM), electron probe microanalyses (EPMA), scanning transmission electron microscope-energy dispersive spectroscopy (STEM-EDS), and X-ray diffraction (XRD).

The area ratio of each phase was calculated as follows. The elemental mapping in a cross-section of a sintered magnet was obtained by STEM-EDS. Each phase of

the sectional view was identified from the element composition ratio of each phase and the XRD results that were confirmed beforehand. Then, the area ratio of each phase relative to the overall area of a cross-section was obtained by image analyses.

To evaluate the microstructure, the coverage ratio of the grains by the grain-boundary phase was calculated [108]. The grains and grain boundaries were recognized automatically in the SEM images by using in-house image-analysis software. Since it was not possible to recognize those grain-boundary phases with a thickness of less than 20 nm, thin grain-boundary phases were manually complemented in the image. Then, the ratio of the length of the automatically detected grain boundaries to that of the manually complemented boundaries was defined as the coverage ratio of the grains by the grain-boundary phases.

To examine the stability of the ferromagnetic (FM)/antiferromagnetic (AFM) states in the grain-boundary phases, first-principles calculations were performed by employing the projector-argument wave (PAW) method and a plane wave basis set within the spin-polarized density function theory implemented in the VASP (Vienna Ab initio Simulation Package) [192]–[194] software package. The generalized gradient approximation (GGA-PBE) was employed. The cutoff energy was set to 400 eV. A Monkhorst-Pack k-point 6 × 6 × 6 mesh was adopted for Brillouin zone sampling. In the PAW potential, ($5s^2$, $5p^6$, $6s^2$, $4f^4$) was treated as the valence electrons for Nd, ($5s^2$, $5p^6$, $6s^2$, 4f, 5d, $6s^2$) for Ce, ($4s^2$, $4p^6$, 4d, $5s^2$) for Y, ($3p^6$, $3d^6$, $4s^2$) for Fe, and ($3d^{10}$, $4s^2$, 4p) for Ga. The strong on-site Coulomb interaction of the f-orbital was corrected by applying a simple +U method with a U value of 6.0.

3.3 Results and discussions

Section 3.3.1 to 3.3.4 show the establishment and results of the candidate composition search using thin film $R_2Fe_{14}B$ magnets. Sections 3.3.5 to 3.3.7 show the results of manufacturing bulk magnets using the obtained candidate materials.

3.3.1 Surface leakage magnetic flux

A Nd-Fe-B ternary composition gradient thin film was investigated in order to confirm the concept of combinatorial chemistry. By using Fe, Nd and B targets, a ternary composition gradient thin film with a thickness of 100 nm was deposited on a Ta underlayer. The thin film was an equilateral triangle with 3.22 mm sides. The composition range was 0-33 at% Nd, 49-100 at% Fe and 0-51 at% B. The substrate temperature was 480°C and post-annealing was not applied. It should be noted that the concentration range is different from the ternary isothermal section at 298 K obtained from the Nd-Fe-B phase diagram in Figure 3-3.

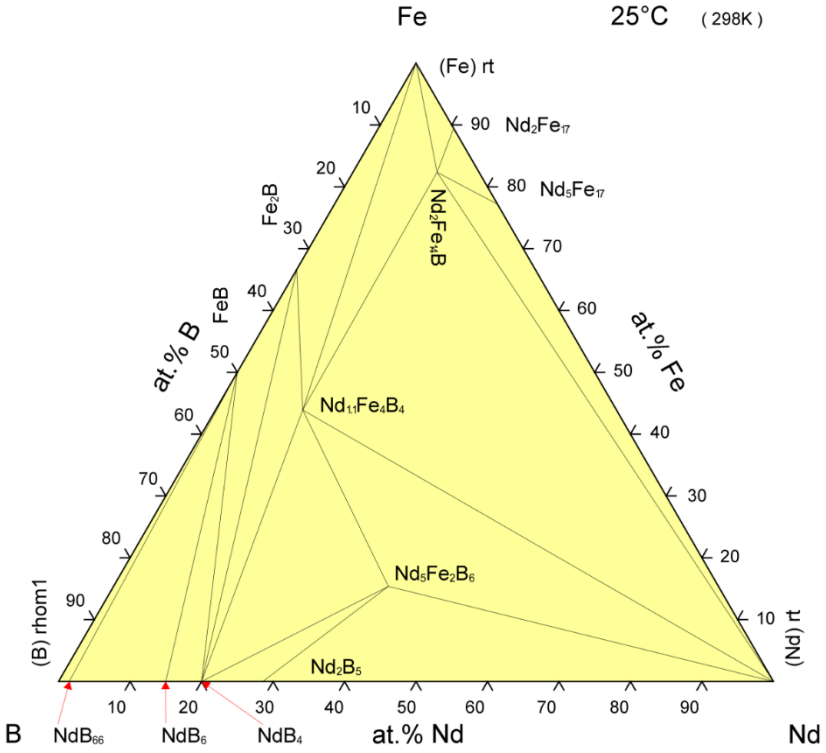

Figure 3-3 Ternary isothermal section of Nd-Fe-B at 298 K.

After magnetization with a pulsed magnetic field of 6382 kA/m, the surface leakage magnetic flux was measured. The higher the measurement resolution, the more detailed the mapping can be obtained, however it is not preferable for the purpose of high-throughput measurement because the measurement time is too long. Figure 3-4 shows the measurement results of the leakage magnetic flux mapping with different line and pitch spaces together with the measurement time.

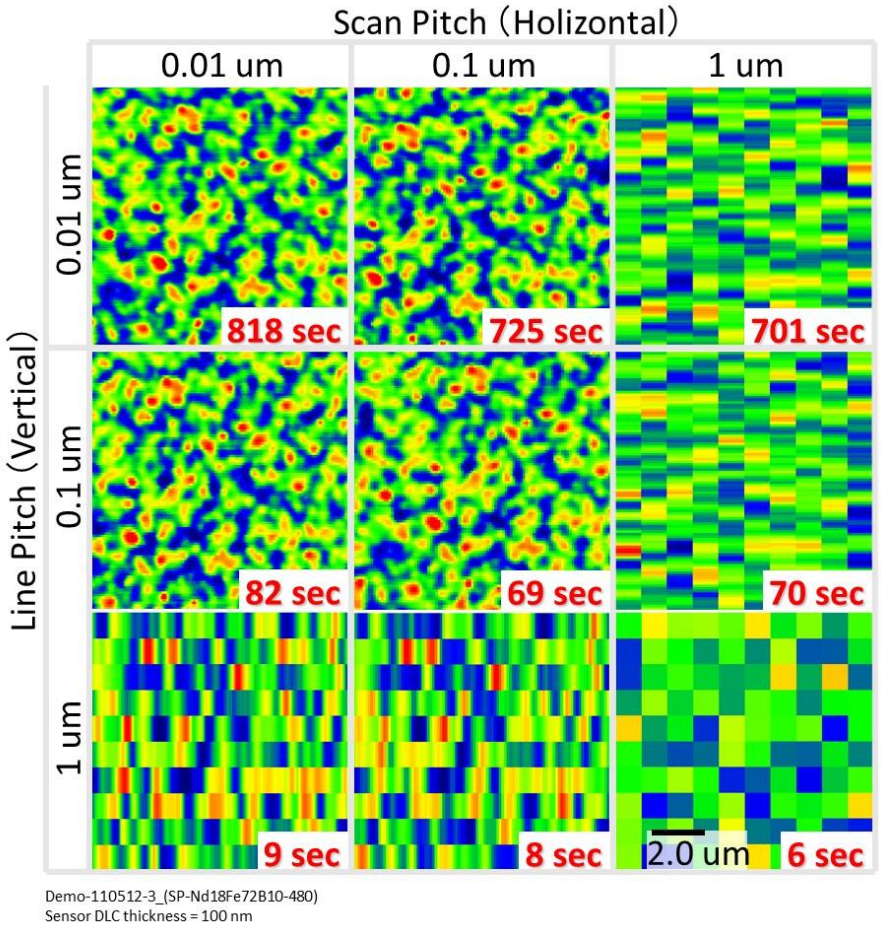

Figure 3-4 Measurement results of the leakage magnetic flux mapping with different line and pitch spaces together with the measurement time.

Although the Nano-MDS equipment had sufficient resolution to measure the magnetization of individual particles, it did not require such resolution to measure the leakage flux at each location in the compositionally graded film. Taking into account the area to be measured, measurement was done with a pitch of 28 μm and a line space of 28 μm with using x-y stage movement, which resulted in the number of measurement points exceeded 5,600. The mapping of surface leakage magnetic flux is shown in Figure 3-5.

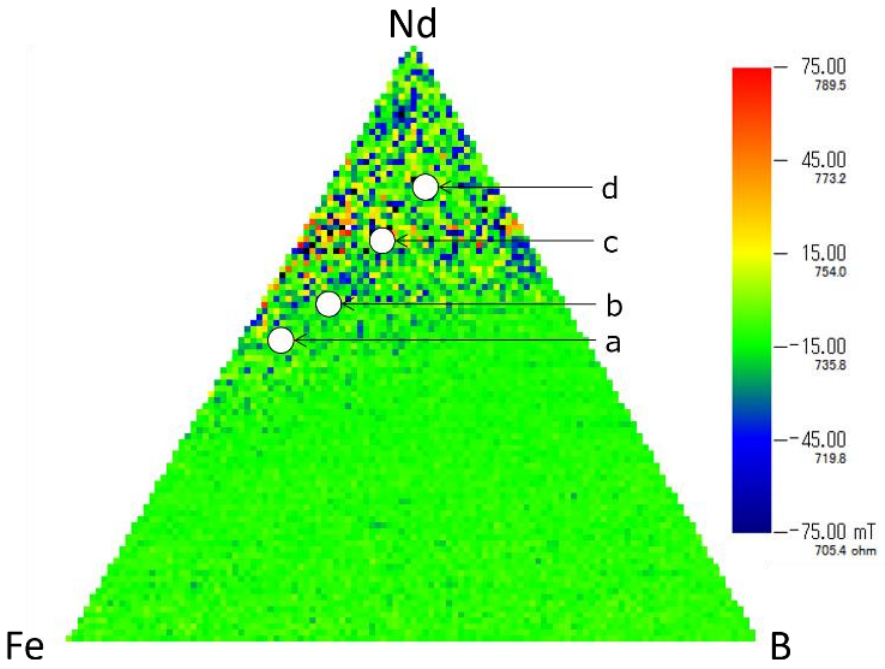

Figure 3-5 Surface leakage magnetic flux mapping of Nd-Fe-B ternary composition gradient thin film. a: $Nd_{10}Fe_{87}B_3$, b: $Nd_{12}Fe_{82}B_6$, c: $Nd_{15}Fe_{77}B_8$, and d: $Nd_{18}Fe_{72}B_1$.

By applying a magnetizing field, only hard magnetic thin film area generates remanent magnetization. A high contrast area is observed at around a vertex of Nd 100 % in the mapping, meaning the high surface leakage magnetic flux is generated.

The cross sectional image and elemental mapping of $Nd_{14.6}Fe_{78.0}B_{7.4}$ thin film observed by STEM-EDS are shown in Figure 3-6. The magnetic flux hardly leaks from the thin film if the film is perfectly uniform because of the demagnetizing field. However, the film is consisting of multi phases with grain structure, thus the magnetic flux can be leaked. From the mapping shown in Figure 3-5, higher contrast is observed around Nd-richer area.

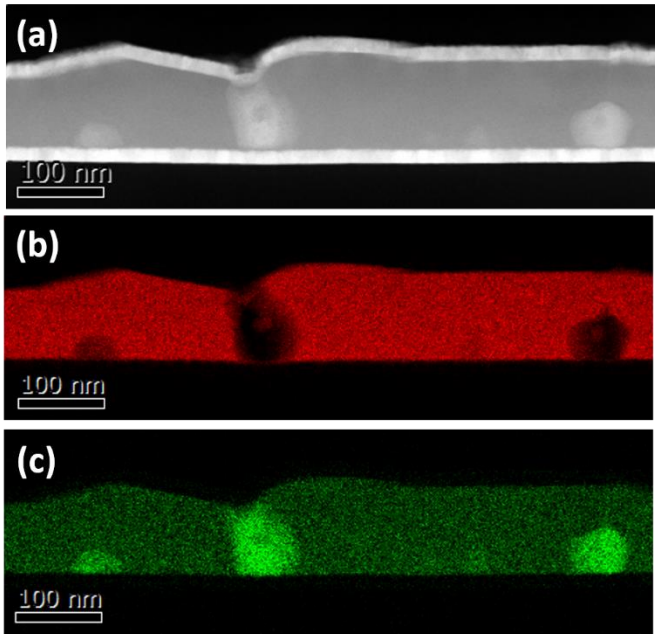

Figure 3-6 (a) The cross sectional TEM image, (b) and (c): the elemental mappings observed by EDS for Fe and Nd, respectively.

The single composition thin films with compositions of $Nd_{10}Fe_{87}B_3$ (Nd-poor), $Nd_{12}Fe_{82}B_6$ (Stoichiometric), $Nd_{15}Fe_{77}B_8$ (Nd-rich), and $Nd_{18}Fe_{72}B_{10}$ (Nd-richer), which is indicated in Figure 3-5 were prepared for measuring M-H characteristics in the direction perpendicular to the film at room temperature. Figure 3-7 shows the results of VSM measurement of the above four compositions, which were prepared by changing the substrate temperature and the annealing temperature.

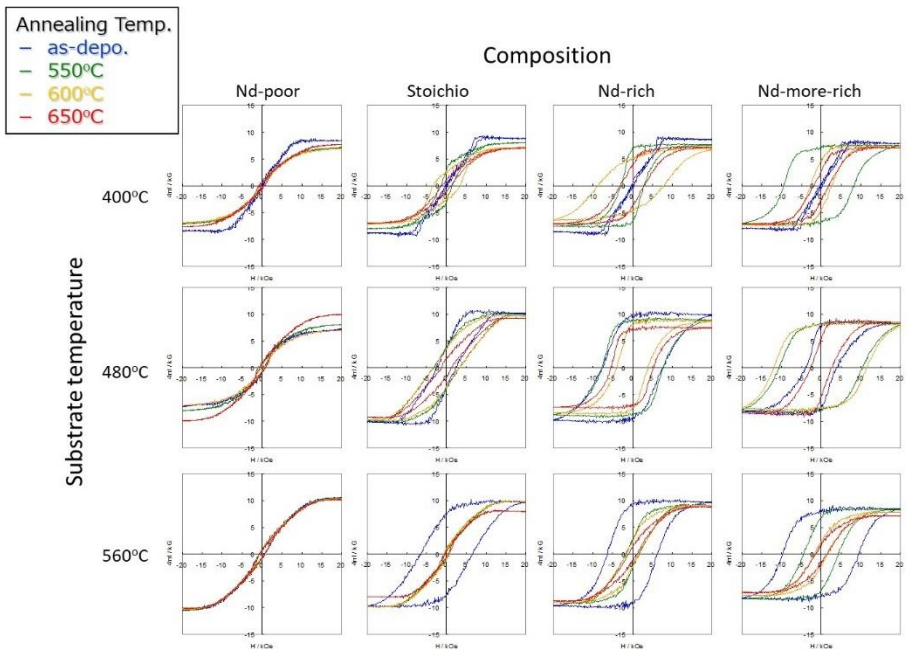

Figure 3-7 VSM measurement results of four compositional thin films prepared by changing the substrate temperature and the annealing temperature.

It can be seen that the sample with a large amount of Nd shows more hard magnetism, although it depends on the heat treatment conditions. The XRD measurement results of these films before annealing are shown in Figure 3-8. Specimens with Nd-poor composition showed no $Nd_2Fe_{14}B$ structure with (00l) orientation.

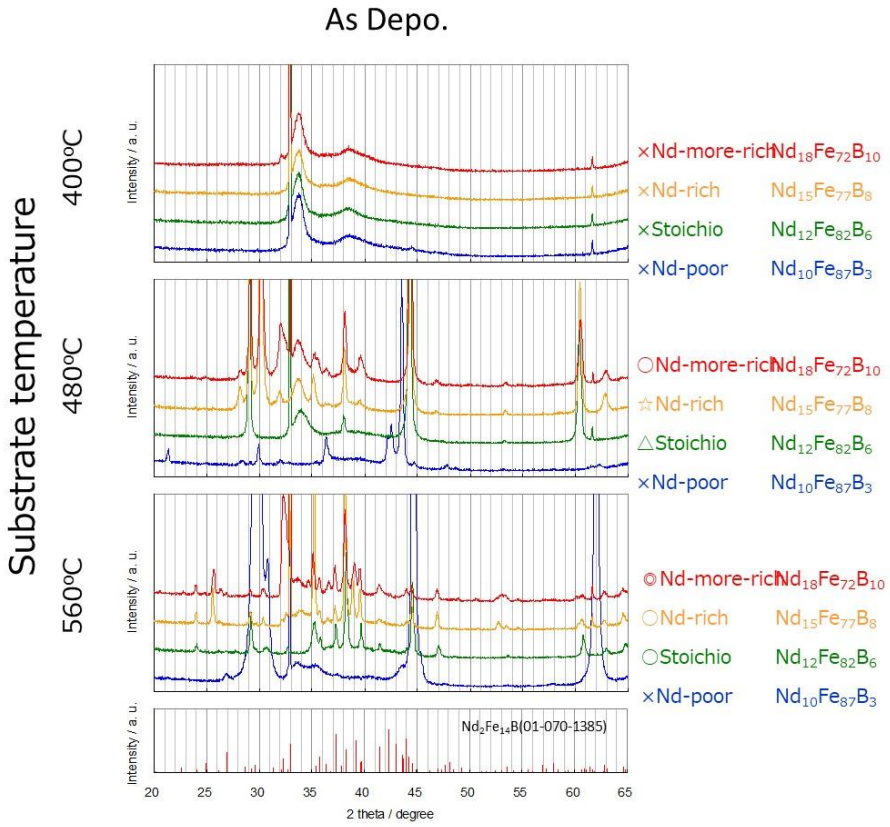

Figure 3-8 XRD results of four compositional thin films with preparing different substrate temperatures.

The VSM measurement results of perpendicular to the substrate are summarized in Figure 3-9. The highest coercivity was achieved in Nd rich composition. The main phase of this film was identified to $Nd_2Fe_{14}B$ by XRD measurement as shown in Figure 3-8. Generally the Nd-Fe-B bulk magnet is produced with a Nd-richer composition compared to the stoichiometric composition, because the excess Nd forms grain boundary phase which magnetically separates each grains. This is important for achieving high coercivity as described in Section 1.5. The grain boundary could affect the coercivity of the ternary composition gradient thin film. From these results, it is concluded that the gradient composition thin film contains the information on composition-dependent magnetization. By measuring the

surface leakage magnetic flux, the candidate composition for $R_2Fe_{14}B$ magnet can be screened.

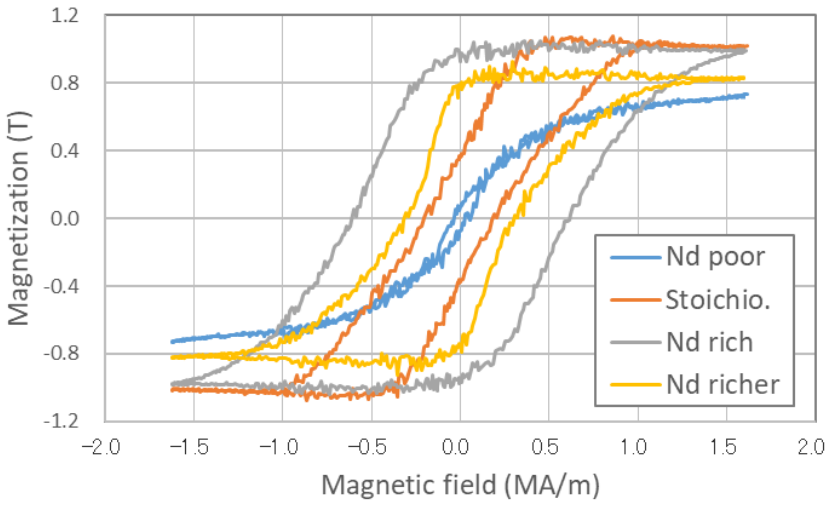

Figure 3-9 Magnetization curves of Nd-Fe-B single composition thin films.

3.3.2 Estimation of coercivity

For the high throughput screening of magnet composition, estimating coercivity is important. The VSM measurement of single composition thin film referring the result of the first screening on surface leakage magnetic flux is reliable, however it is time-consuming. Therefore, a method for simply estimating the coercivity of a portion of the composition gradient thin film was investigated.

Coercivity can be estimated by the demagnetization of fully magnetized thin film. The thin film is first fully magnetized unidirectionally perpendicular to the substrate direction, along to c-axis. When a reverse magnetic field equal to the coercivity is applied, half the entire magnetization reversals occurs, resulting in the highest contrast of surface leakage magnetic flux mapping.

As an example, the mapping change by demagnetization of $Nd_{18}Fe_{72}B_{10}$ thin film with a coercivity of 1093 kA/m (=13.7kOe) measured by VSM is shown in Figure 3-10. First, a magnetic thin film was fully magnetized by applying a vertical magnetic field of 6370 kA/m (=80 kOe), and its surface leakage magnetic flux mapping was measured. Then, a reverse magnetic field of 159 kA/m (=2 kOe) was applied in the direction opposite to the initial magnetization, and the magnetic flux mapping was measured again. These processes were repeated while increasing the applied magnetic field, and finally a reverse magnetic field of -6370 kA/m (=-80 kOe) was applied. The positions where the leakage magnetic flux mapping is measured are not exactly the same.

The highest contrast was observed in the thin film demagnetized with a demagnetization field of 1114 kA/m (=14 kOe). The coercivity and demagnetization field to obtain the highest contrast was almost identical. This is because by demagnetizing with a field correspond to coercivity, half of the grains magnetically reverse then the difference between positive and negative surface leakage magnetic flux reaches the maximum.

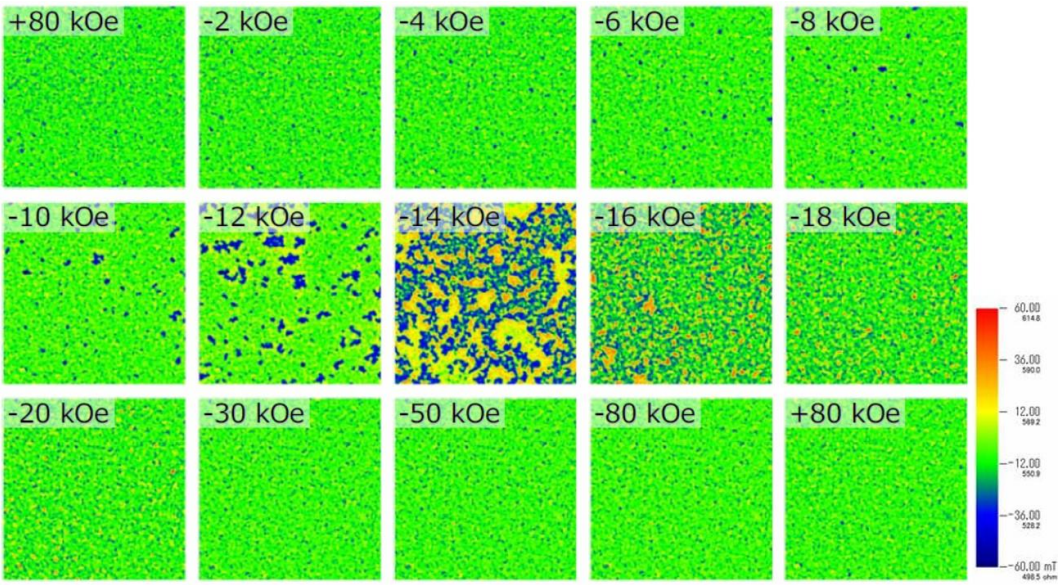

Figure 3-10 Mapping of surface leakage magnetic flux of $Nd_{18}Fe_{72}B_{10}$ thin films with sequential reversed magnetic field applied from full magnetization of 80 kOe (=6,368 kA/m) from left upper side to right lower side.

The continuous demagnetization and simultaneous surface leakage magnetic flux measurement are preferable to shorten screening time, however TMR sensors cannot be used in a high magnetic field. Thus the step-by-step demagnetization and surface leakage magnetic flux measurement is required for estimating coercivity.

3.3.3 Direct measurement of coercivity

In order to know the coercivity more directly, Kerr effect measurement was applied with using a magneto-optical effect measurement system. Reflected light from a magnetized surface can change in both polarization and reflected intensity. The laser with a diameter of 0.1 mm at the sample surface was applied to the thin film then Kerr rotation angle of reflected wave was measured continuously by

sweeping the magnetic field of ±1989 kA/m. The magnetic field is enough for the saturation and the local coercivity was measured from the Kerr rotation angle loop.

The results of VSM and Kerr rotation angle measurement of $Nd_{18}Fe_{72}B_{10}$ thin film annealed at 300 °C are shown in Figure 3-11.

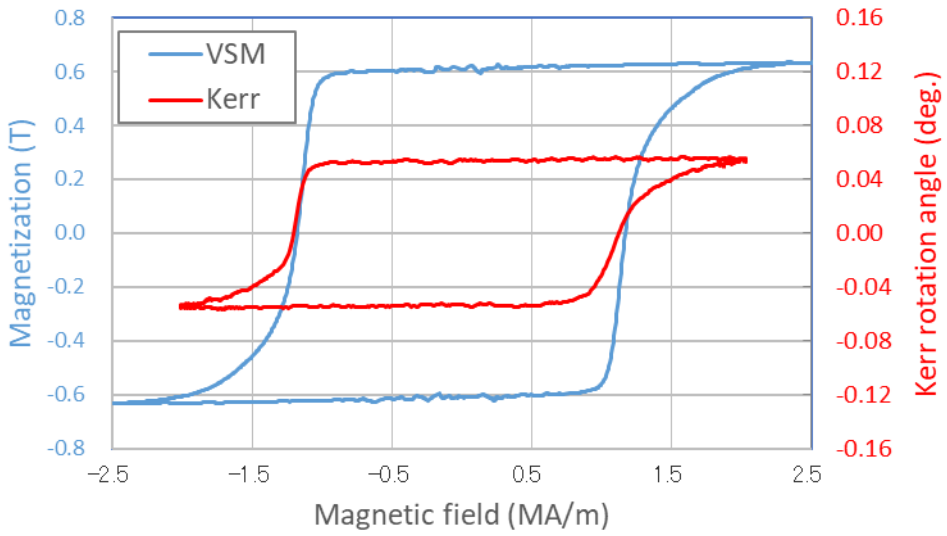

Figure 3-11 Magnetization and Kerr rotation angle curves of Nd-Fe-B single composition thin films.

The coercivities measured by two methods showed almost identical value. A small difference can be resulted from that the VSM measures the magnetization of whole thin film however Kerr rotation occurs at near the surface of thin film. At the bottom of Nd-Fe-B layer, a small amount of diffusion from the underlayer was observed; it affects the coercivity. The coercivity measured by Kerr rotation angle is less affected by this diffusion because Kerr rotation occurs at the surface of the thin film.

3.3.4 Substitution for Nd in R-Fe-B thin film

The high throughput screening method described above was applied to verify the substitution effect of $Nd_2Fe_{14}B$ thin film. As alternatives, yttrium (Y), lanthanum (La) and cerium (Ce) were selected from rare earth elements for their cost and availability. La and Ce are light rare earth elements. Y is not a lanthanoid, however is classified as a heavy rare earth element though it is much lighter than the lanthanoids and not a heavy element. As shown in Table 1-2, Y is a resource-rich and inexpensive element.

A $R_{18.5}Fe_{73.8}B_{7.7}$ composition gradient thin film with a thickness of 100 nm was prepared with using Nd, Y, La and Ce sputter guns as R element and $Fe_{87.8}B_{12.2}$ sputter gun. Thin films were sputtered at substrate temperatures of 821 K, 873 K, and 923 K. The composition range of rare earth elements were all 0-100 at% in the composition of R elements.

The mapping of surface leakage magnetic flux for $(Ce\text{-}Nd\text{-}La)_{18.5}Fe_{73.8}B_{7.7}$ composition gradient thin film prepared at various substrate temperatures are shown in Figure 3-12. The concentrations of all rare earths vary from 0 to 100 at%. Although the color bar indicates a leakage magnetic flux of -100 mT to + 100 mT, it is difficult to discuss the precise absolute value because the magnitude of the leakage magnetic flux varies depending on the surface condition of the sample and the measurement distance. Therefore, the magnitude of the magnetization was determined on the basis of the relative comparison in one composition gradient thin film.

High contrast is observed widely around at the vertex of Nd-Fe-B composition. It was not possible to find the composition which shows the peculiar high leakage magnetic flux. At the amount of substitution for Nd exceeds 60 at%, high magnetization cannot be expected.

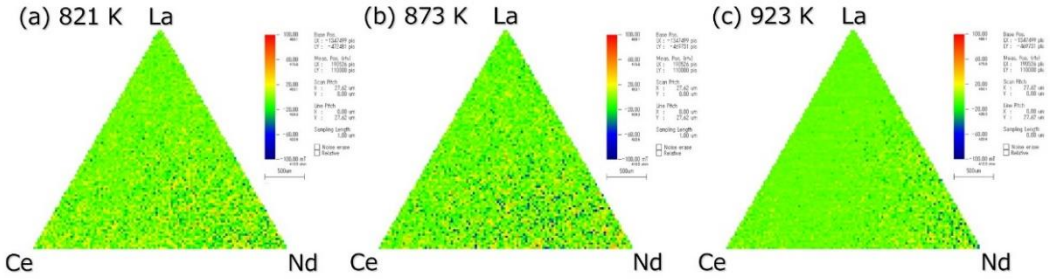

Figure 3-12 Mapping of surface leakage magnetic flux for (Ce-Nd-La)-Fe-B composition gradient thin film sputtered at the substrate temperatures of;
(a) 821 K, (b) 873 K and (c) 923 K.

The mapping of surface leakage magnetic flux for (Nd-La-Y)$_{18.5}$Fe$_{73.8}$B$_{7.7}$ composition gradient thin film prepared at various substrate temperatures are shown in Figure 3-13. The concentrations of all rare earths vary from 0 to 100 at%. The color bar indicates a leakage magnetic flux of -50 mT to + 50 mT, so the leakage magnetic flux of (Nd-La-Y)$_{18.5}$Fe$_{73.8}$B$_{7.7}$ could be comparatively lower than (Ce-Nd-La)$_{18.5}$Fe$_{73.8}$B$_{7.7}$. The highest contrast was unexpectedly achieved at the lowest substrate temperature of 821 K, considering from the melting points of Nd, Ce, La and Y of 1289, 1068, 1193 and 1799, respectively, The reason was not clear. As same as (Ce-Nd-La)$_{18.5}$Fe$_{73.8}$B$_{7.7}$, the high contrast is observed widely around at the vertex of Nd-Fe-B composition.

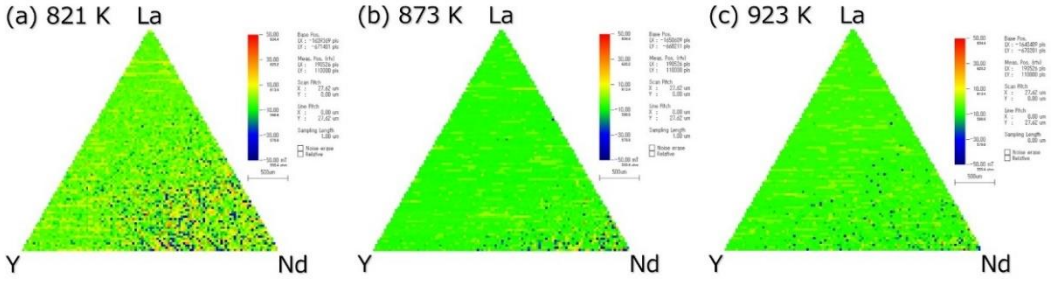

Figure 3-13 Mapping of surface leakage magnetic flux for (Nd-La-Y)-Fe-B composition gradient thin film sputtered at the substrate temperatures of; (a) 821 K, (b) 873 K and (c) 923 K.

The mapping of surface leakage magnetic flux for $(Nd\text{-}La\text{-}Y)_{18.5}Fe_{73.8}B_{7.7}$ composition gradient thin film prepared at various substrate temperatures are shown in Figure 3-14. As same as other $R_{18.5}Fe_{73.8}B_{7.7}$ composition gradient thin film, high contrast is observed widely around at the vertex of Nd-Fe-B composition.

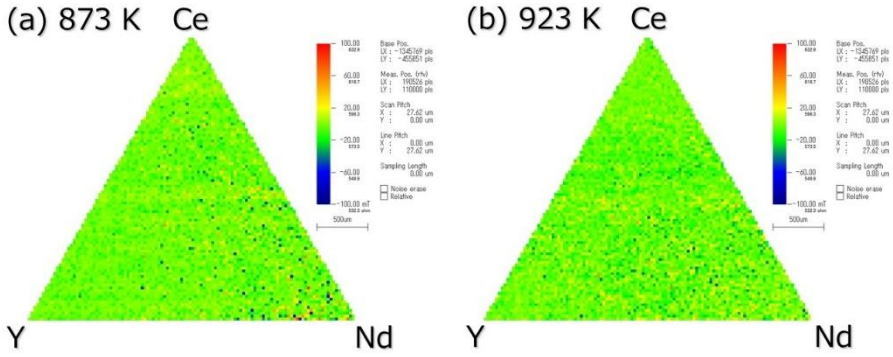

Figure 3-14 Mapping of surface leakage magnetic flux for (Nd-Ce-Y)-Fe-B composition gradient thin film sputtered at the substrate temperatures of; (a) 873 K and (b) 923 K.

The mapping of surface leakage magnetic flux for $(Ce\text{-}La\text{-}Y)_{18.5}Fe_{73.8}B_{7.7}$ composition gradient thin film, which does not contain Nd, prepared at various

substrate temperatures are shown in Figure 3-14. Unlike other $R_{18.5}Fe_{73.8}B_{7.7}$, leakage flux was hardly detected. Without Nd, the remanent magnetization could not be obtained because of the very small coercivity, soft magnetic property.

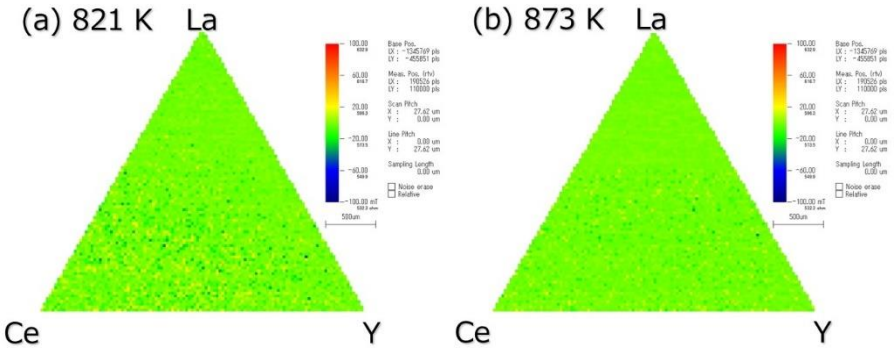

Figure 3-15 Mapping of surface leakage magnetic flux for (Nd-Ce-Y)-Fe-B composition gradient thin film sputtered at the substrate temperatures of; (a) 821 K and (b) 873 K.

In order to clarify the effect of the complex substitution, single composition thin films of $(Ce\text{-}Nd\text{-}La)_{18.5}Fe_{73.8}B_{7.7}$, $(Nd\text{-}La\text{-}Y)_{18.5}Fe_{73.8}B_{7.7}$ and $(Nd\text{-}La\text{-}Y)_{18.5}Fe_{73.8}B_{7.7}$ thin films were prepared. Thin films with different amounts of substitution were simultaneously deposited with using matrix composition deposition method for each ternary composition. The ratio of Nd was 50% in TRE for all samples, and the remaining two elements were 25% each in molar ratio. The magnetic properties of these specimens measured by VSM were shown in Figure 3-16. Although the absolute values of the residual magnetic flux density and the coercivity at the Nd content of 100% are different for each composition system, the relative evaluation is possible because all samples of the same composition system are formed simultaneously with using matrix composition deposition method.

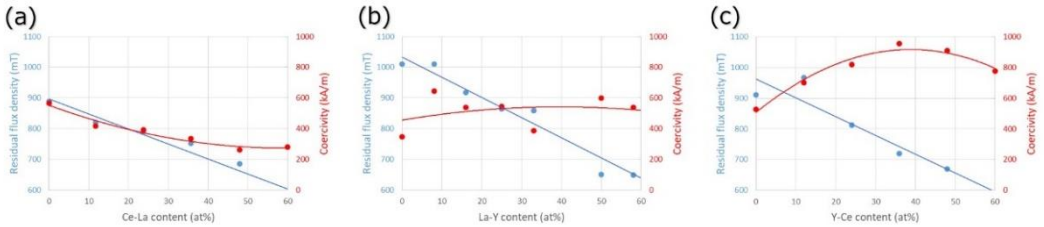

Figure 3-16 Residual flux density and coercivity as a function of substitution by; (a) Ce-La, (b) La-Y and (c) Ce-Y.

The residual magnetic flux density decreased with increasing Nd substitution in all composition systems, however the change of coercivity varied with composition systems. Among these composition systems, the Ce-Y substitution system were investigated in detail.

Three series of substitution, (Nd, Y), (Nd, Ce), and (Nd, Y-Ce) were deposited each separately. The Nd-100 % in TRE thin film was deposited every time as a standard sample for comparison. Because of the thickness difference between estimated value and actual value resulted from instability of deposition rate, the calculated magnetizations of Nd-100 % thin films were not always identical.

Thin films of $(Nd, Y)_{18.5}Fe_{73.8}B_{7.7}$ deposited at a substrate temperature of 923 K were prepared and their residual flux density and coercivity were measured as shown in Figure 3-17.

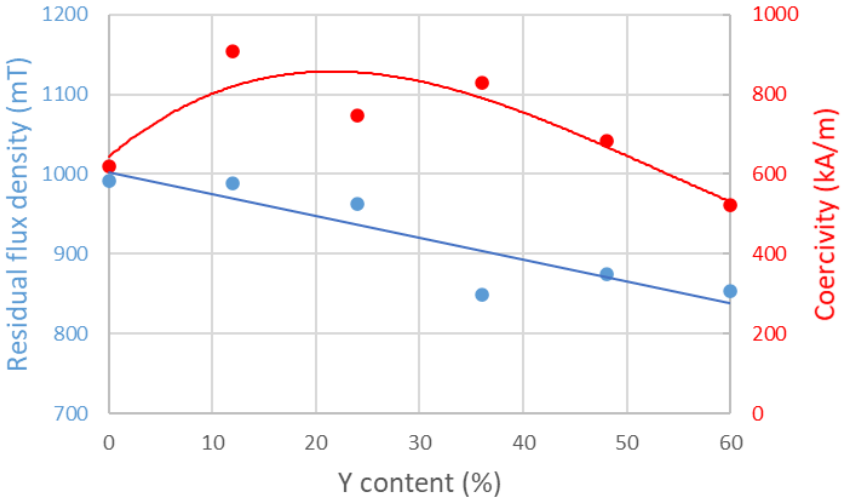

Figure 3-17 Residual flux density and coercivity as a function of Y concentration in rare earth elements (Y/Y+Nd) in molar ratio.

The residual magnetic flux density is comparatively lower than the bulk magnet, and maximum residual flux density is achieved to be 9916 mT for non-substituted Nd-Fe-B. The maximum residual flux density is lower than a typical value of commercial bulk Nd-Fe-B magnets (around 1450 mT), because the film composition is R-richer and the c-axis orientation is lower. All VSM measurements were done in directions perpendicular and in-plane to the film. The perpendicular curves indicated that the easy axis of magnetization is perpendicular to the film plane. However, in-plane curves showed a small hysteresis, because the orientations were not perfect.

From XRD measurement the major phase of these thin films was identified as $R_2Fe_{14}B$ with c-axis orientation. As Y content increased, the peak of (00l) shifted to higher angle. This suggests Y macroscopically substituted for Nd in $Nd_2Fe_{14}B$ crystal structure. The residual flux density gradually decreases as Y content increases. The decrease is reasonably explained since the saturation

magnetizations of $Nd_2Fe_{14}B$ and $Y_2Fe_{14}B$ are 1.6 and 1.42 T, respectively. The coercivity shows the maximum at a composition of 12 at% Y substituted thin film. The anisotropy fields of $Nd_2Fe_{14}B$ and $Y_2Fe_{14}B$ are 5.33 and 1.59 MA/m, respectively, however the coercivity did not decrease monotonically with the addition of Y.

From the STEM-HAADF observations of $(Nd, Y)_{18.5}Fe_{73.8}B_{7.7}$, the film showed layered structure of $Nd_2Fe_{14}B$ and $Y_2Fe_{14}B$ as shown in Figure 3-18.

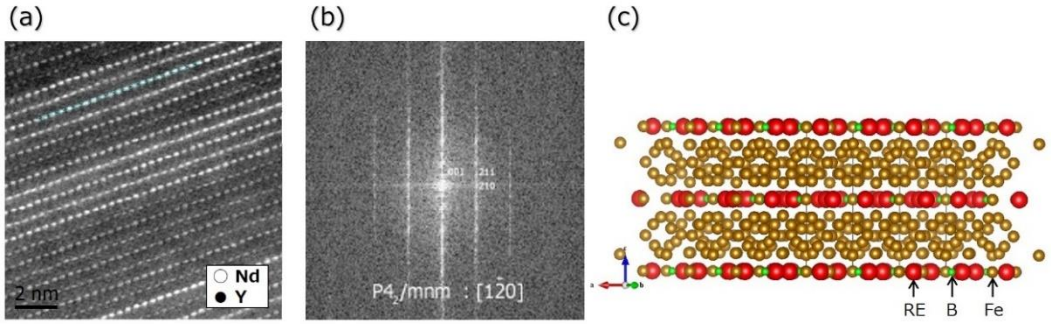

Figure 3-18 Detailed observation of (Nd, Y) $_2Fe_{14}B$ thin film: (a) STEM-HAADF image, (b) electron beam diffraction image and (c) atomic arrangement model from [1 -2 0] direction in $R_2Fe_{14}B$ structure.

It can be seen from Figure 3-18 (a) that a layer structure of a white contrast layer and a gray contrast layer is formed. From the result of the electron beam diffraction as shown in Figure 3-18 (b), it can be seen that Figure 3-18 (a) shows the observation result in the $R_2Fe_{14}B$ crystal structure from the [1 -2 0] direction. As shown in Figure 3-18 (c), when viewed from the [1 -2 0] direction, the layers of rare earth elements (R) are aligned. That is, atoms with white contrast show the overlap of Nd, and atoms with gray contrast show the overlap of Y. From these results, Figure 3-18 (a) shows that a layer structure of $Nd_2Fe_{14}B$ and $Y_2Fe_{14}B$ is

formed, and it is found that Nd and Y are not completely mixed. As shown in Figure 3-19, this thin film is deposited alternately by changing the thickness of Nd, Y and FeB, so it is considered that the layer structure remains unmixed by heating. The thickness of each deposit does not always exactly match the thickness of the layer structure actually formed, however it is considered that the structure at the time of film formation remains strong. It was predicted that this layer structure caused strain between $Nd_2Fe_{14}B$ and $Y_2Fe_{14}B$ layers, and that strain induced anisotropy was added to increase the coercivity [195]. Regarding the effect of strain-induced anisotropy, $Nd_2Fe_{14}B$ was formed on a $BaTiO_3$ film, and the effect of the phase transition of $BaTiO_3$ on $Nd_2Fe_{14}B$ was investigated separately, but it was not clarified clearly [196].

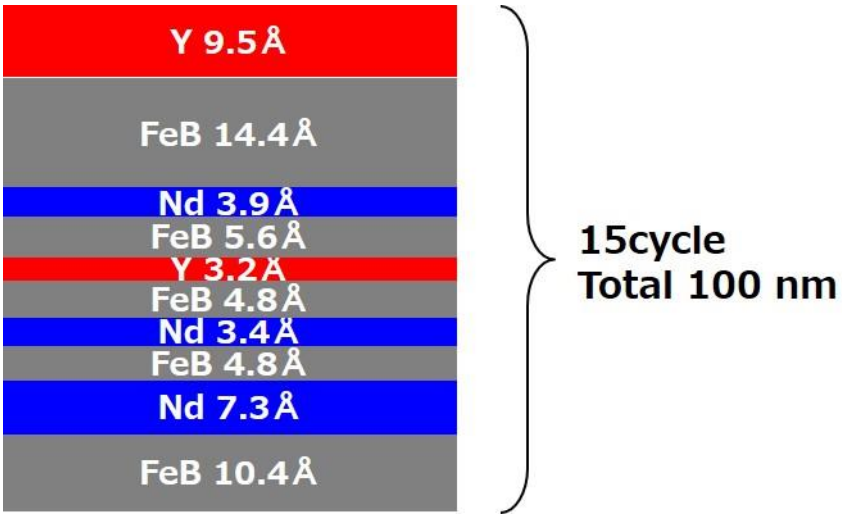

Figure 3-19 Deposition condition of $(Nd, Y)_{18.5}Fe_{73.8}B_{7.7}$ thin film.

Thin films with a composition of $(Nd, Ce)_{18.5}Fe_{73.8}B_{7.7}$ were prepared and their residual flux density and coercivity were measured as shown in Figure 3-20. The decrease of residual flux density is more clearly shown compared to Y substitution, which can be explained by low saturation magnetization of $Ce_2Fe_{14}B$ (1.17 T). The

coercivity also decreases gradually as Ce content increases since the anisotropy fields of $Ce_2Fe_{14}B$ is 2.39 MA/m, which is lower than $Nd_2Fe_{14}B$ [7], [9].

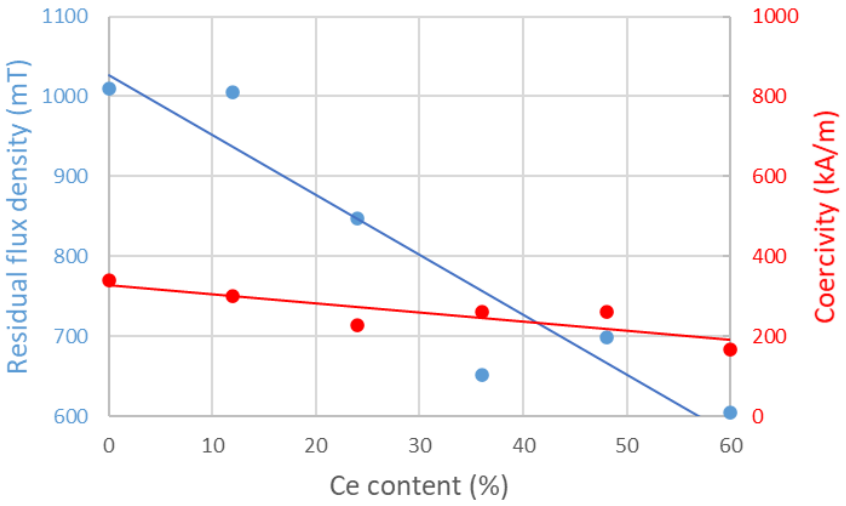

Figure 3-20 Residual flux density and coercivity as a function of Ce concentration in rare earth elements (Ce/Ce+Nd).

Thin films of $(Nd, Y\text{-}Ce)_{18.5}Fe_{73.8}B_{7.7}$ were prepared and their residual flux density and coercivity were measured as shown in Figure 3-21. The ratio of Y and Ce was 1:1 in molar ratio. The residual flux density decreased with the substitution while the coercivity shows maximum at around 40 % substitution. While Pathak et al. and other researchers reported a rapid increase in coercivity and a decrease in remanent magnetic flux density in the case of the Ce 20% substitution [135], [189], [197], [198]. In this experiment, although the Y-Ce 40% substitution (Ce 20% substitution) showed an increase in coercivity, no decrease in remanent magnetic flux density was observed; therefore, it is unlikely that phase separation had an effect [199], [200]. Thus the reason of high coercivity is still unclear. The layered structure described on $(Nd, Y)_{18.5}Fe_{73.8}B_{7.7}$ was not observed in Y-Ce substitution.

The grain size decreased as Y-Ce content slightly increased; the change of grain size is not considered to be a main factor of the change of coercivity. Thus, some interaction between Y and Ce is expected and further investigation is required.

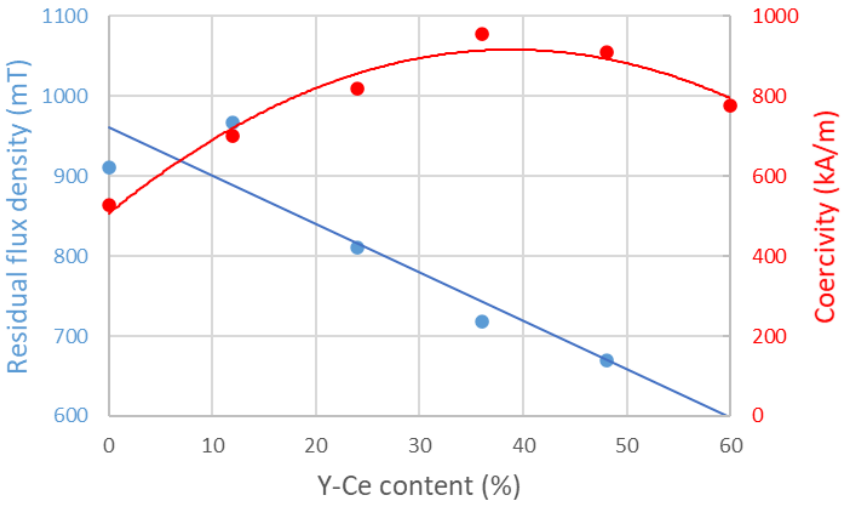

Figure 3-21 Residual flux density and coercivity as a function of Y+Ce concentration in rare earth elements (Y+Ce)/(Y+Ce+Nd).

Based on combinatorial chemistry of $R_{18.5}Fe_{73.8}B_{7.7}$ thin films, candidates for the composition to achieve both high magnetization and coercivity were investigated. Single substitution of Y and simultaneous substitution of Y and Ce showed positive results to achieve the purpose.

3.3.5 High $(BH)_{max}$ in R-Fe-B sintered magnet

Based on the results up to the previous section, the substitution of rare earth elements in sintered magnets was attempted. The residual flux density of a $R_2Fe_{14}B$-type magnet is closely related to the saturation magnetization. Among the

rare-earth elements, Nd exhibits the highest saturation magnetization of 1.60 T in the crystal structure of $R_2Fe_{14}B$ [201]. This means that the substitution of the Nd in $Nd_2Fe_{14}B$ would decrease the residual flux density. From the viewpoint of suppressing the decrease in the residual magnetic flux density, it is reasonable that Y is a candidate of a substitution element. This is because $Y_2Fe_{14}B$ has a relatively high saturation magnetization of 1.42 T compared with other rare earth elements. However, the anisotropy field of $Y_2Fe_{14}B$ (1.59 MA/m) is lower than that of $Nd_2Fe_{14}B$ (5.33 MA/m). In order to improve coercivity, it is reasonable that Ce, which has a high anisotropy field of 2.39 MA/m as $Ce_2Fe_{14}B$, was selected as an element to be added simultaneously with Y as an alternative to Nd. Y and Ce, which became candidate substituents by the thin film CC method as described in Section 3.3.4, are appropriate from the viewpoint of their intrinsic properties. In addition, it is expected that a coercivity increasing effect as shown in Figure 3-21 can be obtained, although the reason is unknown.

The simultaneous substitution of Y and Ce for Nd was performed to obtain a high maximum energy density, $(BH)_{max}$. A $R_2Fe_{14}B$ sintered magnet with a preparation composition of 14.4 at% TRE (Nd:Y:Ce = 50:25:25)-0.6 at% Co-5.7 at% B-M (M=Cu, Al, Zr) -Fe Bal. was prepared. The average particle size was 4.0 μm. The pressed specimen was fired at 1333 K and then annealed at 1173 and 953 K. The obtained demagnetization curve is shown in Figure 3-22. The maximum energy density of 355 kJ/m3 (44.6 MGOe) was achieved with a residual flux density of 1.38 T and a coercivity of 533 kA/m.

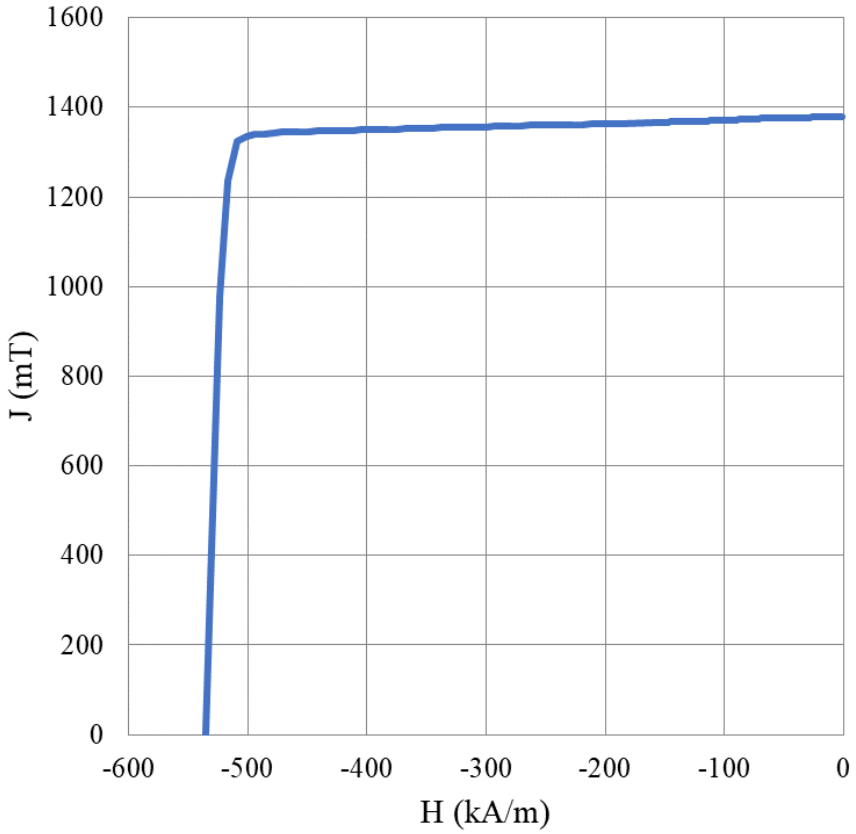

Figure 3-22 Demagnetization curve of 50 % Nd substituted $R_2Fe_{14}B$ sintered magnet.

The temperature coefficients of residual flux density and coercivity were α = -0.14 %/°C and β = -0.59 %/°C (23-120 °C), respectively, which are slightly smaller than those of typical Nd-Fe-B magnets. The σ-T curve of this magnet was measured by VSM. A fully magnetized sample was prepared, and magnetization from room temperature to 643 K. was measured while applying a magnetic field of 80 kA/m. Two Curie temperatures of 533 K and 563 K were present and were expected to be in a mixed phase state as shown in Figure 3-23. The Curie temperatures of $Nd_2Fe_{14}B$, $Y_2Fe_{14}B$ and $Ce_2Fe_{14}B$ are 586, 571 and 422 K, respectively, and the Curie temperature of the magnet is estimated to be 541 K from the simple mixing rule. There was no significant difference between the estimated and measured values. From the Curie point, it is expected that the

composition close to $Ce_2Fe_{14}B$ does not exist as a single phase, but becomes a mixed phase state of the composition close to $Nd_2Fe_{14}B$ and $Y_2Fe_{14}B$.

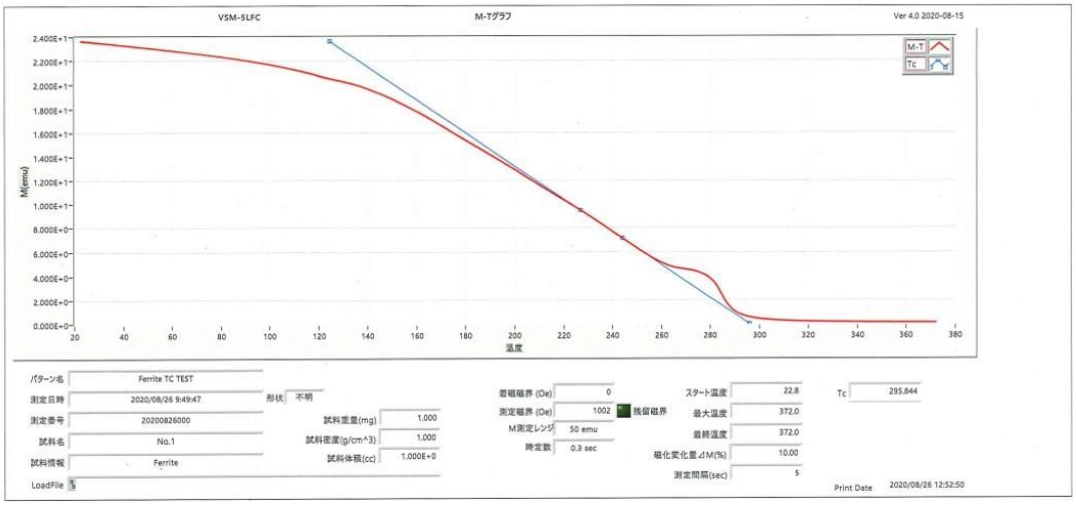

Figure 3-23 A σ-T curve of the developed specimen.

A cross-section of this sintered magnet is shown in Figure 3-24. The black areas are the $R_2Fe_{14}B$ grains. Both white and gray areas are observed in the image. With using EPMA, the former was identified as R-Fe (so-called R-rich phase), while the latter was the RFe_2 phase. They exist at grain boundary and triple junction.

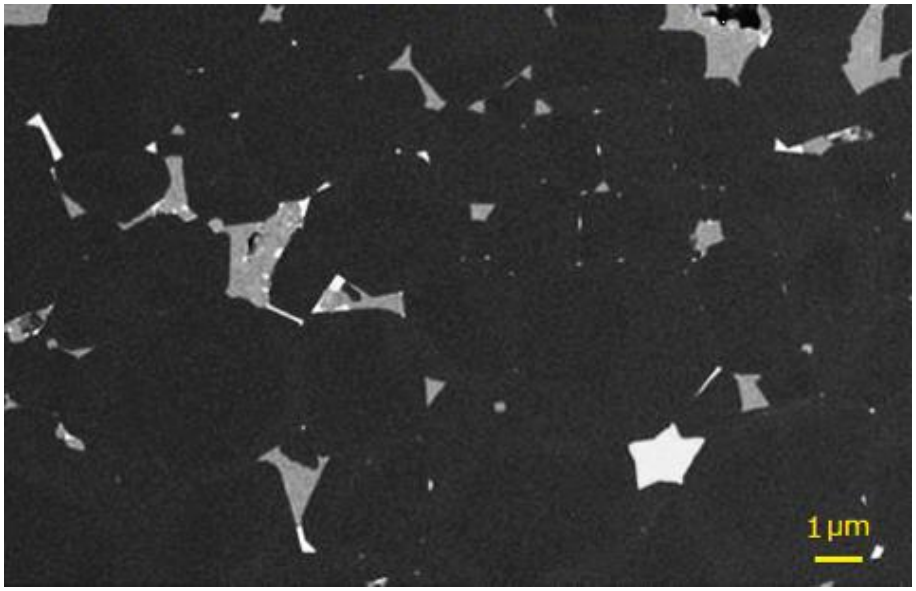

Figure 3-24 Cross-section of Nd 50 % substituted $R_2Fe_{14}B$ sintered magnet.

3.3.6 Introduction of $R_6Fe_{13}Ga$ phase into grain boundary

Given that the minimum coercivity of commercially available $Nd_2Fe_{14}B$ magnets is around 955–1114 kA/m, the coercivity of the Nd substituted magnet, 533 kA/m, is too low for practical use. To improve the coercivity, converting the RFe_2 phase, which is considered to reduce the coercivity [202], to $R_6Fe_{13}Ga$ was attempted which is described in Chapter 2. The addition of 0.6 at% Ga was attempted with a preparation composition of 17.6 at% TRE (Nd:Ce:Y=50:25:25)-0.6 at% Ga-0.6 at% Co-4.7 at% B-M (M=Cu, Al, Zr) -Fe Bal., which contains more TRE to ensure that the grain boundary phases are clearly formed. The average particle size was set to 2.0 μm to attain a higher coercivity. The sintering temperature was 1273 K. Figure 3-25 shows cross sections of specimen in which Ga was added to Nd-Fe-B and (Nd, Ce, Y)-Fe-B at 0.6 at% and the results of phases identification by EDS.

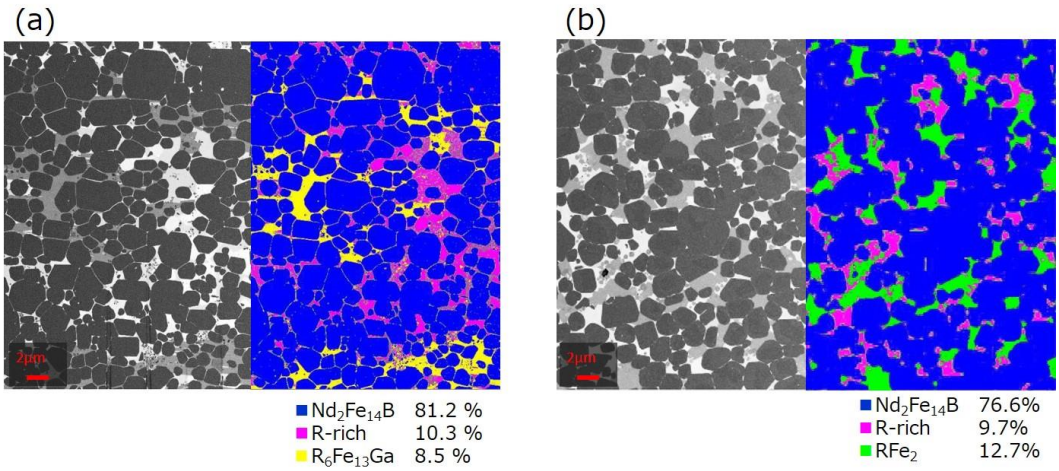

Figure 3-25 Cross section and EDS mapping of Ga added specimens;

(a) Nd-Fe-B and (b) (Nd, Ce, Y)-Fe-B.

Unlike Nd-Fe-B, $R_6Fe_{13}Ga$ was not formed in (Nd, Ce, Y)-Fe-B nevertheless the addition of 0.6 at% Ga is sufficient for forming the $R_6Fe_{13}Ga$ grain-boundary phase in a $Nd_2Fe_{14}B$ system [202], [203]. The RFe_2 phase was remarkably observed at the grain boundaries in (Nd, Ce, Y)-Fe-B.

The rare earth element composition of the RFe_2 phase was measured using STEM-EDS, which confirmed a value of 10.7 at% Nd-22.6 at% Ce-1.7 at% Y-Fe Bal. Unlike the preparation composition, the concentration of Ce was more than twice that of Nd, while the concentration of Y was very low. The phase diagrams reveal that the YFe_2 and $CeFe_2$ phases exist stably, but the $NdFe_2$ phase does not as shown in Figure 3-26. The melting points of YFe_2 and $CeFe_2$ are 1398 and 1198 K, respectively while that of YFe_2 is above the sintering temperature. First principles calculations also suggest that Y tends to enter the $R_2Fe_{14}B$ phase [199], [200]. Thus, Ce is easily enriched in the RFe_2 phase over this temperature range [204].

The RFe_2 phase is known as the Laves phase (AB_2 structure). The Laves phase is known to be stable at the atomic half-space ratio A: B = 1.225: 1 [205]. Among

Ce and Nd having close atomic numbers, the reason why Ce easily forms the Laves phase and Nd hardly forms is explained that the ionic radius becomes small because Ce takes a mixed valence state of trivalent and tetravalent [204], [206].

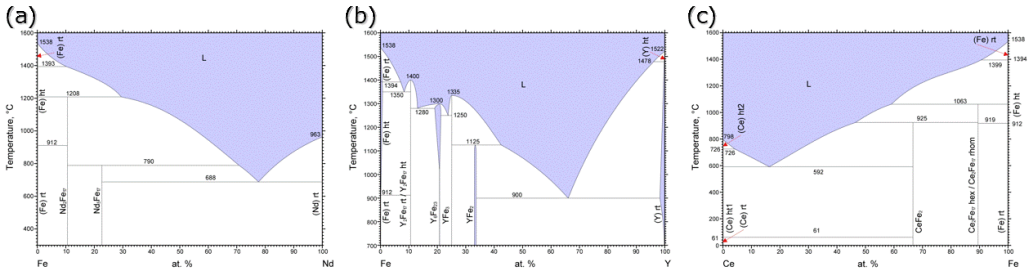

Figure 3-26 Phase diagrams of R-Fe; (a)Nd-Fe, (b)Y-Fe and (c)Ce-Fe.

To investigate the magnetization of RFe_2 phase, a STEM-Lorentz method was applied [202]; the magnetization of the phase can be estimated directly from the sintered magnet. The RFe_2 phase at the triple junction, which is shown as the gray area in Figure 3-24, was cut out by using FIB as shown in Figure 3-27 (a), and the magnetization intensity and directions of the small areas were calculated from the Lorentz polarization angle and the specimen thickness. The vector mapping of the magnetization is shown in Figure 3-27 (b). Based on the results, the magnetization of the RFe_2 phase was estimated to be 0.3–0.5 T. This magnetization is more than six times greater than that of the $Nd_6Fe_{13}Ga$ phase, that is, 0.05 T [202] and one third or fourth that of the $Nd_2Fe_{14}B$ grain, which is thought to not be small enough to ensure magnetic separation between the grains.

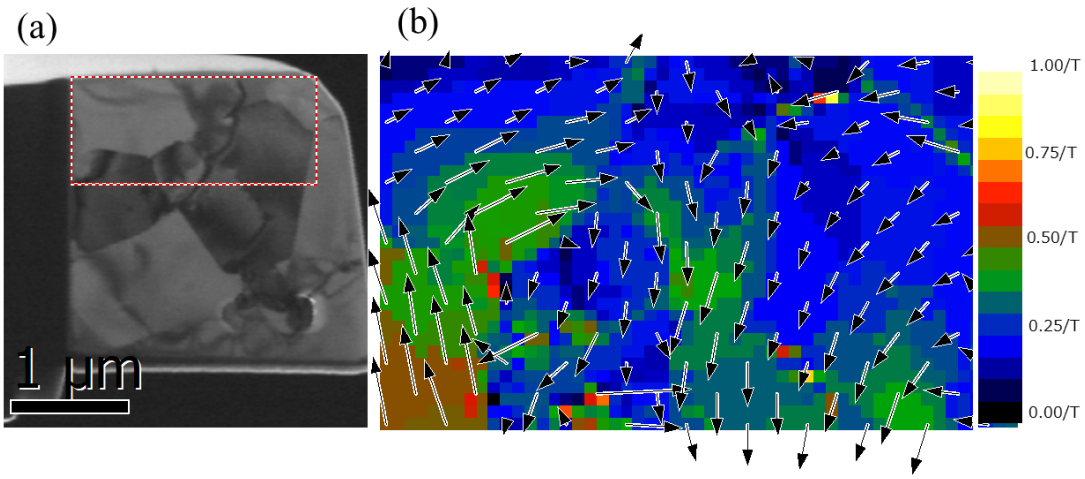

Figure 3-27 (a) TEM image of RFe_2 grain-boundary phase and (b) magnetization mapping in the image estimated using STEM-Lorentz method.

To form the $R_6Fe_{13}Ga$ phase at the grain boundary, further Ga was added. The 0.0–4.0 at% Ga addition was tried with the prepared composition of 17.0–17.5 at% TRE (Nd:Y:Ce=50:25:25)- 0.0 to 4.0 at% Ga-0.6 at% Co-4.6 to 4.7 at% B-M (M=Cu, Al, Zr) -Fe Bal. The average particle size was 2.0 μm.

The STEM-EDS mapping and electron diffraction patterns of the grain boundary phases in the specimen to which 2.0 at% Ga had been added are shown in Figure 3-28. Both the RFe_2 (Structure type: $MgCu_2$) and $R_6Fe_{13}Ga$ (Structure type: $La_6Co_9(Co_{0.5}Ga_{0.5})_4Ga$) phases are observed at the grain boundaries. The $R_6Fe_{13}Ga$ phase in Y- and Ce-substituted specimen exhibited the same crystal structure as that of the $Nd_6Fe_{13}Ga$ specimen.

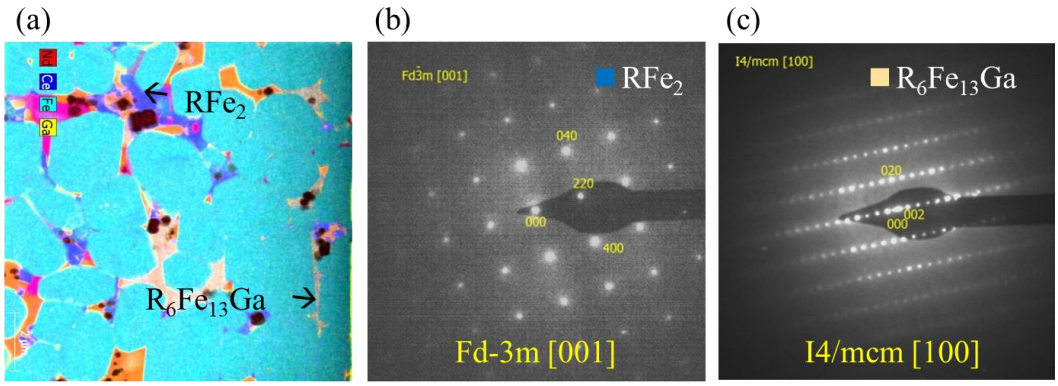

Figure 3-28 Grain-boundary phases in 2.0-at% Ga-added specimen; (a) STEM-EDS mapping, (b) electron-diffraction pattern of RFe_2 phase and (c) electron-diffraction pattern of R6Ga13Ga phase.

The coercivity is plotted as a function of the Ga content with the identified phase, as shown in Figure 3-29. The basic composition is 17.4 at.%TRE-0.6 at.% Co-4.7 at.% B-M-Bal. Fe (M = Ga, Cu, Al). The coercivity decreases monotonically with an increase in the Ga content. The $R_6Fe_{13}Ga$ phase appears between the specimens with a 1.0–3.0 at% Ga addition. Above 3.0 at%, it disappeared to form the R-Fe-Ga phase. As a result, the formation of the $R_6Fe_{13}Ga$ phase required more than 1 at% Ga to suppress the formation of the RFe_2 phase at the grain boundary. However, the $R_6Fe_{13}Ga$ formation did not improve the coercivity, contrary to expectations.

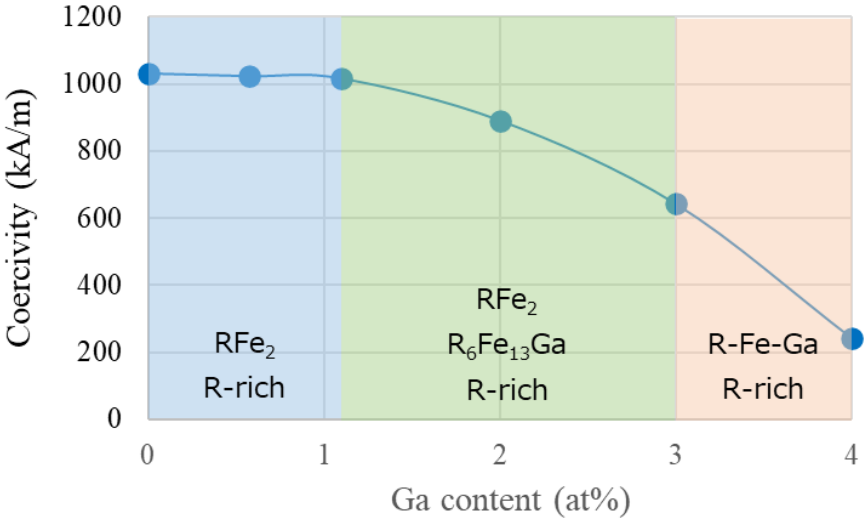

Figure 3-29 Relationship between Ga content and coercivity with existing grain boundary phases.

The composition and magnetization of the $R_6Fe_{13}Ga$ phase in the specimen to which 2.0 at% Ga had been added were measured. The rare earth element composition was 20.6 at% Nd-8.6 at% Ce-1.7 at% Y, which clearly showed the enrichment of Nd in the $R_6Fe_{13}Ga$ phase followed by Ce, but only a small amount of Y was contained. The magnetization of the phase estimated by the STEM-Lorentz method was 0.15 T, which was triple that of the $Nd_6Fe_{13}Ga$ phase (0.05 T), as shown in Figure 3-30. It is found that the substitution of Nd by Ce and Y increases the magnetization. This high magnetization in the grain boundary phase can negatively affect the magnetic separation, however, resulting in a lower coercivity.

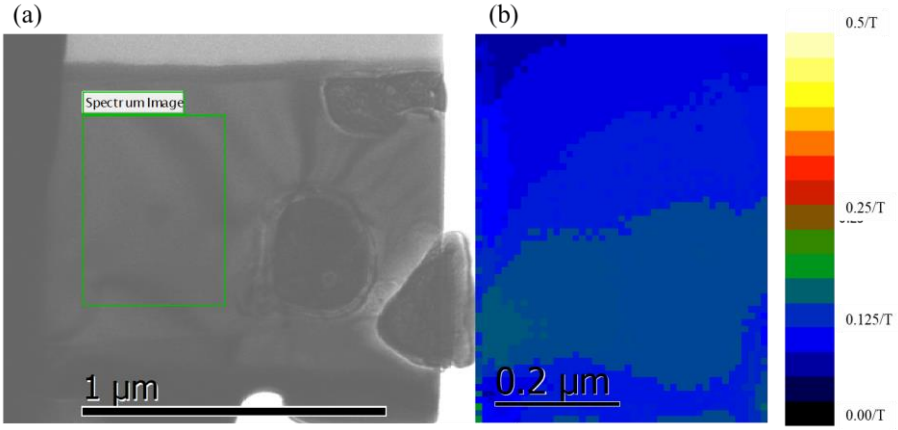

Figure 3-30 Magnetization of $R_6Fe_{13}Ga$ phase; (a) TEM image of $R_6Fe_{13}G$ grain-boundary phase and (b) STEM-Lorentz mapping of $R_6Fe_{13}G$ phase.

The relationship between the Ce or Y concentration and FM/AFM stability in the $R_6Fe_{13}Ga$ phase was evaluated by first-principles calculations. Tetragonal $Nd_6Fe_{13}Ga$ (space group: *I4/mcm*) was selected as a model for the calculation. There are two sites for Nd (Wyckoff position:$16l_1$ and 8f) and four sites for Fe ($16l_2$, $16l_3$, 16k, and 4d). The Nd 8f site was replaced by Y or Ce, resulting in the formation of $Nd_4R_2Fe_{13}Ga$ (R = Y or Ce). The FM and AFM phases were formed by varying the initial magnetic moment of Fe for the calculations. In this investigation, to attain the FM phase, the initial magnetic moments of all the Fe sites were placed parallel to one another. On the other hand, to attain the AFM phase, those of the Fe at $16l_2$ and $16l_3$ sites were placed antiparallel to the Fe at the 16k and 4d sites. Therefore, the magnetic moments of the Fe along the c-axis were set to be antiparallel. To obtain an energetically stable structure including the ionic positions and magnetic moments, the total energies were minimized in the calculation.

The calculated total energy of the $Nd_6Fe_{13}Ga$ in FM phase was 0.22 eV/atom larger than that of the AFM phase as shown in Figure 3-31. It indicate AFM is stable in $Nd_6Fe_{13}Ga$.

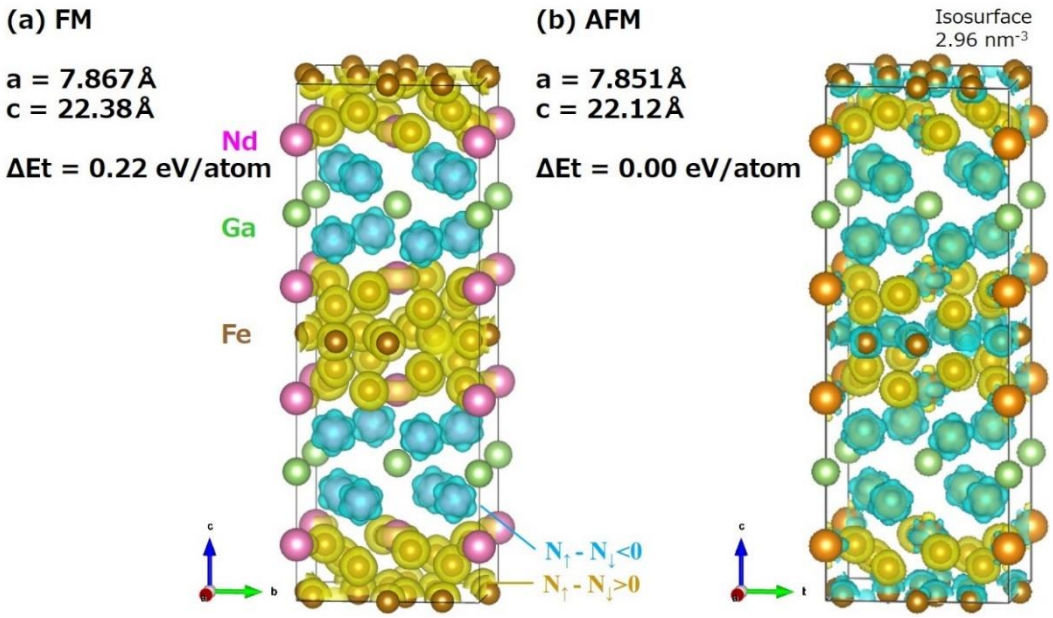

Figure 3-31 Spin difference charge density distribution in the $Nd_6Fe_{13}Ga$ phase; (a) ferromagnetic state and (b) anti-ferromagnetic state.

This figure shows the spin difference charge density distribution in the $Nd_6Fe_{13}Ga$ phase at an isosurface of 2.96 nm^{-3}. A cloud of electrons surrounds each atom, with yellow indicating more up spins and blue indicating more down spins. Therefore, if the color around the Fe atom is different for each Fe atom, it indicates that it is not ferromagnetic but antiferromagnetic (or ferrimagnetic).

The calculated total energy of the $Nd_4Y_2Fe_{13}Ga$ in the FM phase was 0.18 eV/atom larger than that of the AFM phase as shown in Figure 3-32. It indicates AFM is stable in $Nd_4Y_2Fe_{13}Ga$, as same as $Nd_6Fe_{13}Ga$.

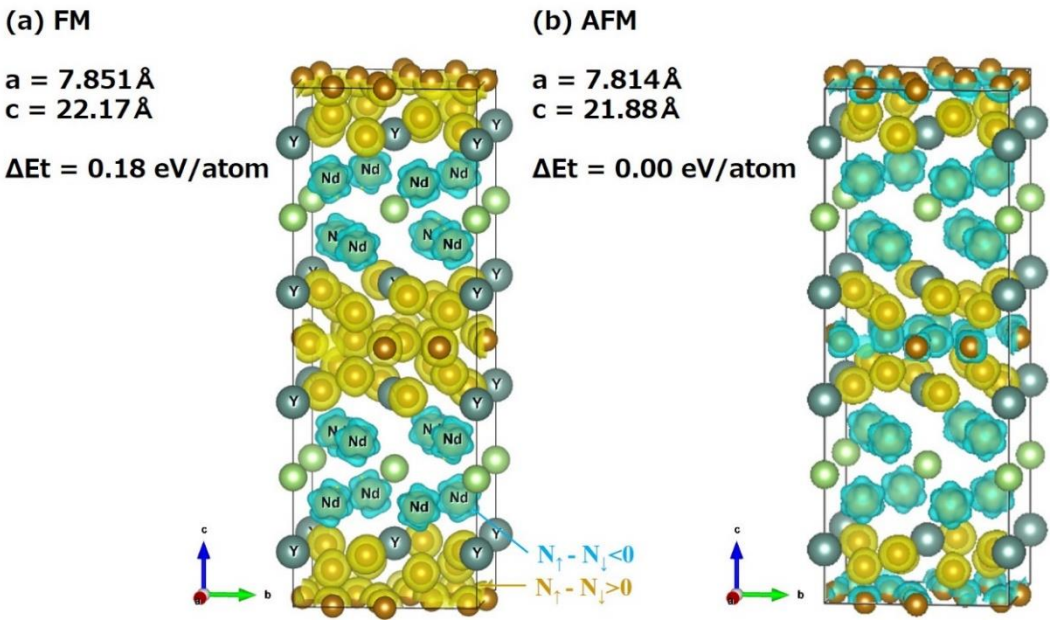

Figure 3-32 Spin difference charge density distribution in the $Nd_4Y_2Fe_{13}Ga$ phase; (a) ferromagnetic state and (b) anti-ferromagnetic state.

On the other hand, the calculated total energy of the $Nd_4Ce_2Fe_{13}Ga$ in FM phase was 0.12 eV/atom smaller than that of the AFM phase as shown in Figure 3-33. It indicates FM is stable in $Nd_4Ce_2Fe_{13}Ga$.

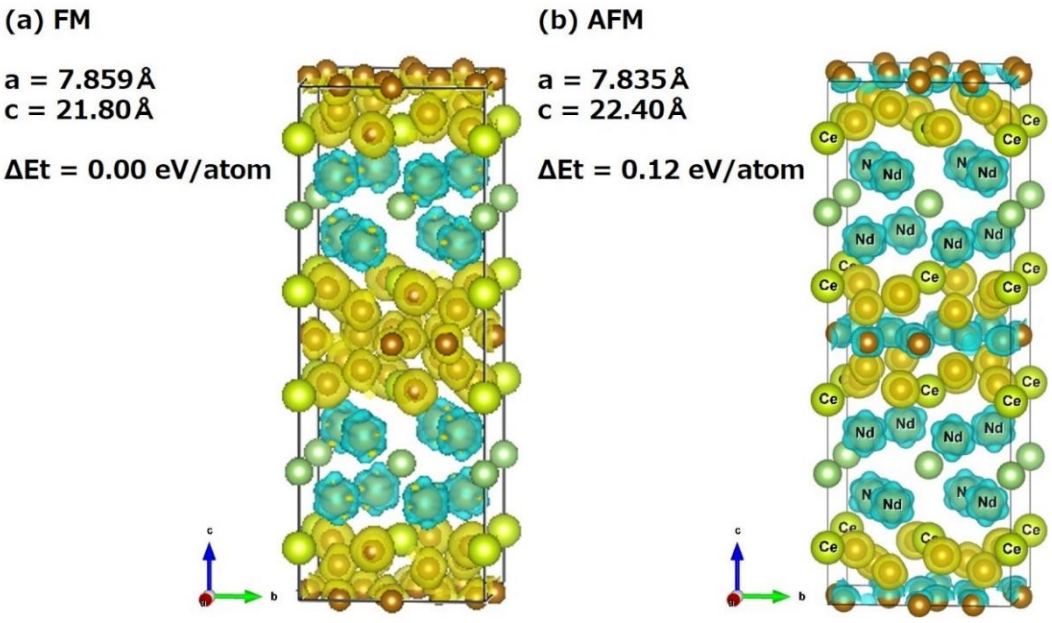

Figure 3-33 Spin difference charge density distribution in the $Nd_4Ce_2Fe_{13}Ga$ phase; (a) ferromagnetic state and (b) anti-ferromagnetic state.

These calculated results indicate that the magnetization of the $Nd_{6-x}Ce_xFe_{13}Ga$ can increase with x. Based on the composition of the $R_6Fe_{13}Ga$ phase, the effect of Ce is dominant compared to Y, such that the $R_6Fe_{13}Ga$ in this experiment could be considered to be the FM phase while the $Nd_6Fe_{13}Ga$ is AFM phase. In the $R_6Fe_{13}Ga$ phase of the 2.0 at% Ga added specimen, the rare earth element composition was 20.6 at% Nd-8.6 at% Ce-1.7 at% Y. Since this composition is rewritten as $Nd_4Ce_{1.7}Y_{0.3}Fe_{13}Ga$, it is clear that the substitution of Nd by Ce affects the stability of FM/AFM more than Y. Therefore, the results of FM/AFM stability in the simulation confirmed the increase in magnetization of $R_6Fe_{13}Ga$ due to Ce substitution.

3.3.7 Control of Ce concentration in RFe_2 phase

At room temperature, $CeFe_2$ is considered to be paramagnetic [202], [203], [207]–[211]. However, the effect of substituting Nd with other rare earth elements

on the magnetization of RFe_2 is not clear. The composition and magnetization of the RFe_2 phase were investigated in detail. The ingot of $CeFe_2$ was fabricated using an arc-melting method. The magnetization of the ingot was measured with the STEM-Lorentz method, being found to be about 0.05 T; this is regarded as being small enough for magnetic separation like the $Nd_6Fe_{13}Ga$ grain boundary phase in a $Nd_2Fe_{14}B$ sintered magnet [108].

The magnetization of the RFe_2 phase at room temperature was estimated using RFe_2 ingots with a composition of $(Nd_{1-x}Ce_x)Fe_2$. With using XRD, the phases in the ingots were found to be RFe_2, RO_x and a small amount of RFe_7 and R-rich phases. The area ratio of the RFe_2 phase was almost 80 % in all the specimens, as determined by SEM-EDS. The magnetization of the RFe_2 phase was estimated from the area ratio estimated from the cross sectional images and total magnetization, as measured by VSM, assuming that the magnetization of the small amount of RFe_7 and R-rich phase was constant, regardless of the Ce concentration.

The area ratio of each phase was calculated using SEM-EDS. The estimated magnetization of the RFe_2 phase as a function of the Ce concentration, after removing the effects of the magnetization of other phases, is shown in Figure 3-34. The magnetization of the RFe_2 phase decreases linearly with the Ce concentration. Thus, the coercivity can be improved by increasing the Ce concentration in the RFe_2 grain boundary phase.

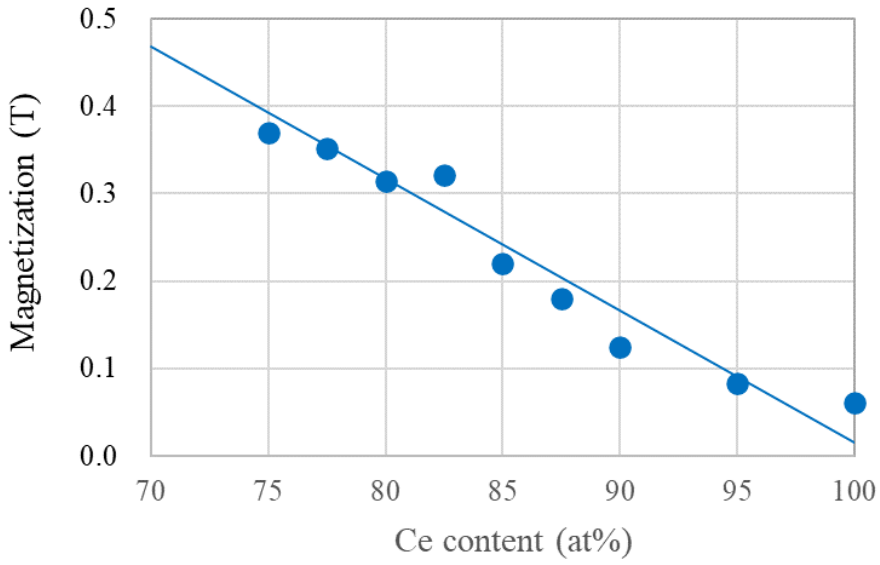

Figure 3-34 Estimated magnetization of $(Nd_{1-x}Ce_x)Fe_2$ phase.

Specimens were prepared by setting the concentration ratios of Nd, Y, and Ce to 50:25:25, 50:10:40, and 50:0:50 in molar ratio with the preparation composition of 16.0 at% TRE-0.6 at% Co-5.0 at% B-M (M = Cu, Al, Zr) -Fe Bal. The average particle size was 2.8 μm. The optimum sintering temperature for the highest coercivity decreased as the Ce concentration increased, being 1288, 1243, and 1228 K, respectively. The coercivity, residual flux density, coverage ratio, RFe_2 phase ratio, and Ce/TRE in the RFe_2 phase are listed in Table 3-1.

Table 3-1 Magnetic properties and microstructural feature points in 16.0 at% TRE-0.6 at% Co-5.0 at% B-M (M=Cu, Al, Zr) -Fe Bal. magnet.

Ce /TRE (%)	25	40	50
H_{cJ} (kA/m)	920	1063	1004
B_r (T)	1.27	1.22	1.18
$(BH)_{max}$ (kJ/m^3)	288	260	236
Coverage ratio (%)	53	65	62
RFe_2 phase ratio (%)	10	15	16
Ce/TRE in RFe_2 phase (%)	67	74	79

The maximum coercivity of 1063 kA/m (13.4 kOe) was achieved with a residual flux density of 1.22 T and a maximum energy density of 260 kJ/m^3 in a Ce/TRE ratio of 40 % specimen. The anisotropy field of the sample with Ce concentration of 40% is calculated to 3780 kA/m according to the mixing rule. Therefore, the value of the coercivity is 28% of the anisotropy field (H_{cJ}/H_A), which is much larger than the value of 15% of the conventional Nd-Fe-B magnet (The coercivity criterion is given in Appendix section).

The concentration of Ce in the RFe_2 grain boundary phase increased as the Ce content in TRE increased, as was expected. However, the coercivity did not increase. Since the maximum Ce concentration was 79 %, the magnetization is expected to be around 0.3 T, based on Figure 3-34, such that the magnetic separation is not enough to increase the coercivity. The coverage ratio was a maximum of 65% at a Ce/TRE ratio of 40 %. The coverage ratio indicates the degree of total grain isolation, which is responsible for the high coercivity. The specimen with a Ce/TRE ratio of 50 % was sintered at the lowest temperature applied to the three specimens, that is, 1228 K because above this temperature, abnormal grain growth occurred to lower the coercivity. Although the melting point

of the $CeFe_2$ phase is below the sintering temperature, 1198 K, it is thought that the melting point of RFe_2 is increased by the substitution. The low sintering temperature could lower the wettability between the grain boundary phase and grains, resulting in the lower coverage ratio. Since this coverage ratio is thought to be closely correlated to the coercivity, the highest coercivity was obtained at a Ce/TRE ratio of 40 %.

The coverage ratio of 65% is smaller than the value of more than 80% obtained for a Nd-Fe-B magnet without Dy and Tb which was described in Section 2.3.7. This is because RFe_2 consumes only Fe in the R-rich phase, unlike $Nd_6Fe_{13}Ga$, which decomposes $Nd_2Fe_{14}B$, the main phase, and forms RFe_2 by using Fe. Therefore, the formation of thin RFe_2 grain boundary phase can be less aggressive than that of the $Nd_6Fe_{13}Ga$ phase.

The (Nd, Ce)Fe_2 grain boundary phase did not have as low magnetization as $Nd_6Fe_{13}Ga$ described in Section 2.3.5, but had lower magnetization than the R-rich phase used in conventional Nd-Fe-B magnets, which may contribute to the magnetic isolation of the grains. Compared with the introduction of $Nd_6Fe_{13}Ga$, a higher coverage ratio was not obtained, which may be due to the fact that, unlike the formation of $Nd_6Fe_{13}Ga$, the (Nd, Ce)Fe_2 phase is formed by consuming Fe in the R-rich phase rather than Fe in the $R_2Fe_{14}B$ phase. This may be due to the fact that the (Nd, Ce)Fe_2 phase is very easy to form and no additional heat treatment is not required to form like $Nd_6Fe_{13}Ga$. As a result, the formation of grain boundary phase was not sufficient and the coverage rate was not sufficiently improved compared to more than 80 % at the introduction of $Nd_6Fe_{13}Ga$ grain boundary phase.

3.4 Conclusion

In order to reduce the use of Nd and Pr itself in Nd-Fe-B magnet, substituting Nd with more abundant rare earth elements was performed; a high-throughput composition search method was constructed, and a sintered magnet was made by combining a microstructure control technique. The combinatorial chemistry method was used as a composition search method to search for the composition of thin film magnets. The selected candidate compositions were then applied to the bulk magnets. The grain boundary phase composition and its magnetization were controlled in a sintered magnet.

Based on the concept of combinatorial chemistry, the formation of composition gradient thin film and evaluation methods of their magnetic properties were established. Magnetization was estimated from the leakage magnetic flux which was measured with a nano-MDS system and coercivity was measured by Kerr-rotation angle and VSM with using a matrix composition deposition method. A pseudo ternary R-Fe-B thin film was prepared with substituting Ce, La and Y for Nd as R element, the magnetic properties were evaluated. Simultaneous substitution of Y and Ce showed comparatively high magnetic properties [202].

Then the effects of the grain boundary phases in a 50 % Y- and Ce- substituted $R_2Fe_{14}B$ sintered magnet were investigated. The substitution of Y and Ce to achieve higher levels of magnetization and coercivity was performed, achieving a maximum energy density of 355 kJ/m3 (44.6 MGOe) with a residual flux density of 1.38 T and a coercivity of 533 kA/m. To improve the coercivity, the introduction of a $R_6Fe_{13}Ga$ grain boundary phase was attempted. With the addition of 0.6 at% Ga, the $R_6Fe_{13}Ga$ phase was not observed but the RFe_2 phase was found to be dominant in the grain boundary phase. By increasing the Ga content to 1 and 3 at%, the $R_6Fe_{13}Ga$ phase appeared, however the coercivity decreased due to the large magnetization of the phase.

The magnetization of (Nd, Ce)Fe_2 decreased with the increase in the Ce concentration, suggesting that the introduction of the phase may lead to magnetic separation between the grains. However, the change in the Ce concentration in the RFe_2 grain boundary phase of a 16.0 at% TRE-0.6 at% Co-5.0 at% B-M (M = Cu, Al, Zr) -Fe Bal. sintered magnet was small and rather the coverage ratio of the grains by the grain boundary phase influenced the coercivity in the Ce content dependence. The highest coercivity was achieved at a Ce/TRE ratio of 40 %, this being 1063 kA/m (13.4 kOe) with a residual flux density of 1.22 T. The obtained coercivity was much higher than our target value, 800 kA/m, and it can be said that 50% reduction of Nd and Pr was achieved.

* Some of the results in this chapter were summarized in papers [202], [203].

Chapter 4 Grain boundary protection in near-net shaping

4.1 Introduction

Granulation of Nd-Fe-B magnets is attempted. Since the reduction of R-rich phase by oxidation and carbonization of Nd-Fe-B magnet powder leads to the lowering of coercivity, the process was developed to minimize it. To facilitate supply of magnet powder to a mold having a narrow and long cavity by securing fluidity of granules, and to obtain high magnetic characteristics. As magnetic characteristics, coercivity and residual magnetic flux density of 99% or more were aimed in comparison with sintered magnets made from non-granulated powder.

In order to align the magnetization directions of each grains in sintered body during the regular magnet manufacturing procedure, net-shape pressing must be performed uniaxially under an external magnetic field [212]. Transverse pressing, in which the magnetic field is applied perpendicularly to the pressing force, produces magnets with higher residual flux densities than those obtained via axial pressing. The setup of transverse pressing is illustrated as shown in Figure 4-1. The magnetic powder is fed into the powder feeder, which vibrates in the forward and backward directions over the cavity, causing the magnetic powder to fall freely into the cavity. The narrower the opening of the die and the deeper the cavity, the more difficult it is to fill the cavity with magnetic powder.

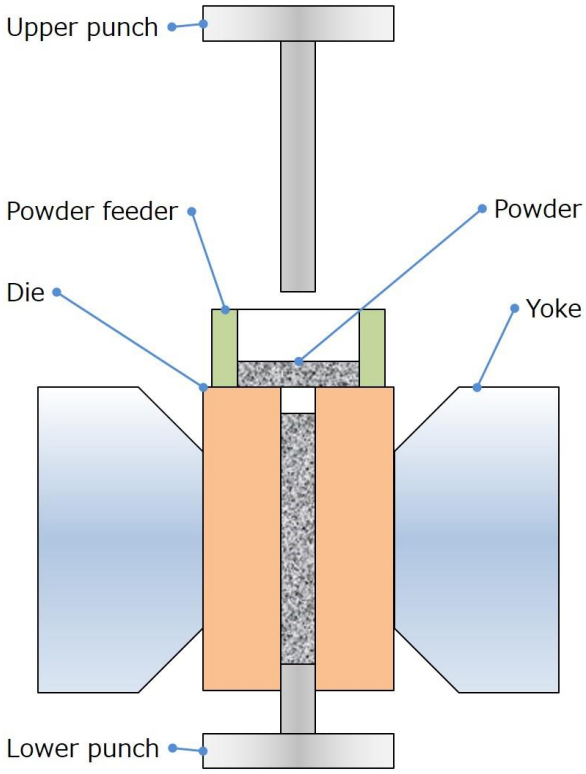

Figure 4-1 An illustration of transverse pressing in magnetic field.

The majority of the shapes utilized for fabricating high-performance magnets have shorter dimensions along the direction of the magnetic field; hence, the transverse pressing method is widely used for mass production, despite the limited number of processable shapes. Because the utilized die cavity has a relatively narrow opening and large depth, increasing the flowability of the magnetic powder is extremely important for meeting the requirements of high-performance magnetic products [171]–[174]. It also facilitates the filling of narrow cavities, increases the filling rate, and decreases the weight variations of the molded product. Note that it is extremely difficult to uniformly fill multiple cavities with the same weight of the magnetic powder characterized by low flowability. Furthermore, high pressure is applied only to a small number of cavities, which ultimately leads to mold breakage.

Binder-bound granules prepared by a spray drying method are widely used to manufacture the ceramic parts of electronic components [213]. Such granules represent secondary particles (aggregates of primary particles) with excellent flowability properties due to their relatively large sizes [173] and round shapes. However, because it is difficult to align each primary particle in a binder-bound granule along the easy axis direction, the granule pressing technique cannot be practically used for magnet manufacture. To apply the spray drying method, the bonding strength of each particle in the granule should be lower than the rotational force exerted by the magnetic field; otherwise, a sufficient degree of orientation cannot be achieved for an anisotropic magnet. The state of the powder in the ideal granule pressing process is shown in Figure 4-2. The granules to be applied to the magnetic powder should retain their granule shape until they are filled into the cavity (Figure 4-2 c)), and after filling the cavity, when a magnetic field is applied for orientation, the granule shape should disintegrate due to the rotational torque of the primary particles by the magnetic field (Figure 4-2 d)). Thus, after the state illustrated in Figure 4-2 d), traces of granules must be completely eliminated.

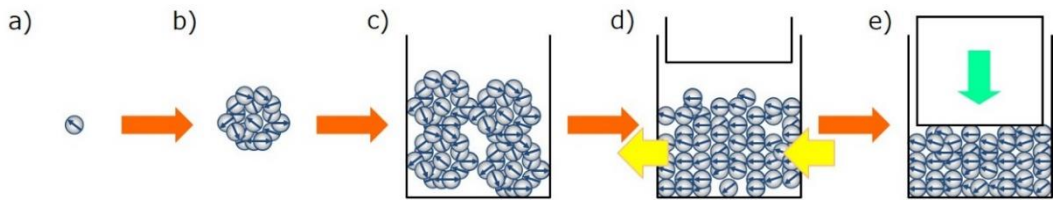

Figure 4-2 An illustration of granule molding; a) primary particles, b) secondary particles (granules), c) die filling, d) application of magnetic field, e) pressing.

As an example, a simple comparison is made with respect to the difference in the material yield by the processing means when the arcuate magnet is formed. Here, the magnet for 8-pole surface mounting permanent magnet motor (SPM) for electric power steering (EPS) was assumed. Create an arcuate magnet with an inner diameter of 35 mm and an outer diameter of 38 mm and a width of 26 mm and a height of 25 mm. This shape is shown in Figure 4-3. The parallel orientation direction is perpendicular to the center of the arc.

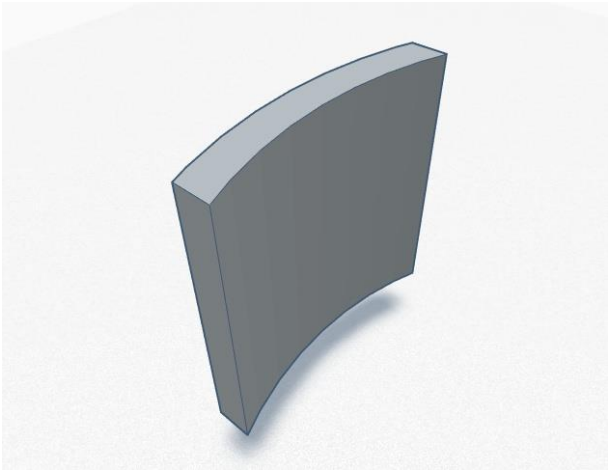

Figure 4-3 An illustration of arcuate magnet.

Since it is difficult to perform near-net pressing of this magnet, several arc-shaped magnets are usually machined out from a magnet block. Here, near-net pressing means that the shape is formed to be close to that of the final product, which in this case is a single arc-shaped magnet. So, assume that we are going to carve out four arc magnets from a single magnet block. This process is shown in Figure 4-4. Assume that the cutting allowance for making the magnet surface flat is 0.3 mm and the thickness of the cutting blade for cutting the magnets is 0.5 mm. First, a magnet block is hexahedronically machined and then this magnet is divided into

four parts by cutting blades. The arc-shaped magnet is ground out of the rectangular magnet. The volume of the four arc magnets total is calculated to45% of the original magnet block. In other words, the material yield is 45%. The next step is to calculate the material yield if near-net molding were possible. Suppose that a near-net pressing process is used to press and sinter a near-net magnet and the surface of the magnet is ground down to 0.3 mm. The volume of the arc-shaped magnet at this point is 79% of the volume before grinding. In other words, the material yield is 79%. These results mean that 34% of the magnets will not be lost if near-net pressing is possible.

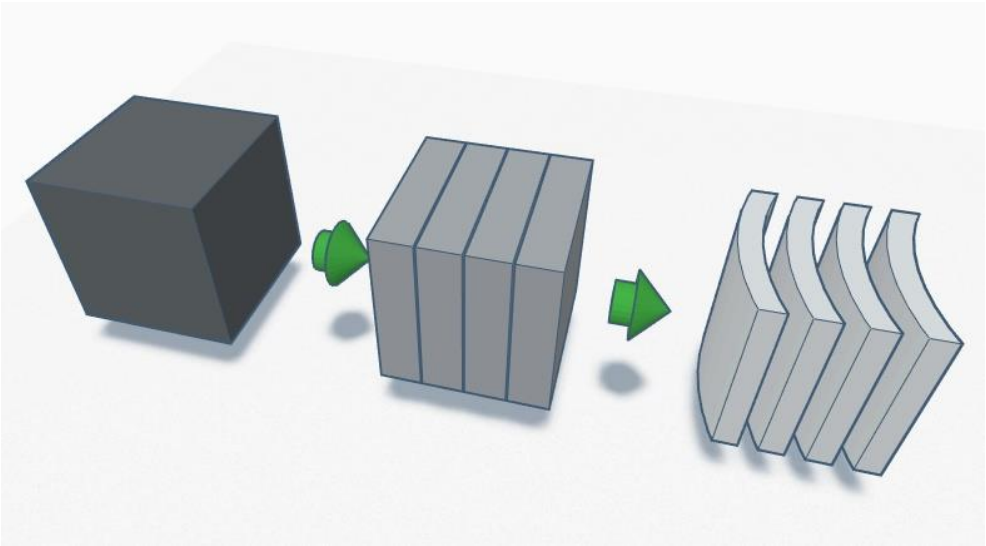

Figure 4-4 Machining process of arc magnets from a magnetic block.

As described, the actual amount of reduction depends on the magnet design. The smaller the number of magnet poles in motor design, the greater the arc angle and the greater the reduction in waste. For example, the motor design as explained above is a 8-pole rotor with the width of 26mm but in a 4-pole designed with a

width of 48mm and 2-pole designed with a width of 68 mm, the Nd, Pr, Dy and Tb waste is reduced by 57% and 68%, respectively.

4.2 Experimental procedure

4.2.1 Preparation of primary magnetic particles

Two different alloys with the compositions 12.1 at.% Nd–2.4 at.% Dy–0.5 at.% Co–6.0 at.% B–M-bal. Fe (M = Cu, Al) and 12.6 at.% Nd–1.8 at.% Dy–0.5 at.% Co–6.0 at.% B–M-bal. Fe (M = Cu, Al) were produced by a strip casting method. These alloys possessed different magnetization and coercivity properties due to the different contents of Nd and Dy. The raw alloys were coarsely pulverized by a hydrogen decrepitation method followed by fine pulverization via jet milling to obtain fine powders with an average particle diameter of 4.7 μm. The pulverization process was performed in an anaerobic atmosphere with an oxygen content of 3000 ppm and 0.1 wt% solid lubricant, fatty acid amide, was added to prevent fusion of milled particles.

4.2.2 Preparation of magnetic granules

Binder-bound granules

A slurry of magnetic particles was prepared from a primary magnetic powder, an organic binder, and a solvent without a dispersant. The primary particles obtained from one of the two above-mentioned alloys were used as the magnetic powder. PVA (PVA 217, Kuraray Co., Ltd.) with a saponification degree of 87–89% and polymerization degree of 1700, and polyvinyl butyral (PVB BH-3, Sekisui chemical co., Ltd.) with a polymerization degree of 1700 were utilized as the organic binders. Deionized water and ethanol were used as the solvents. First, an

organic binder was completely dissolved in a solvent followed by the addition of the magnetic powder and mixing by an agitator. Powder concentration in the slurry was 15 vol%.

The binder-bound granules were produced by spraying the slurry using a rotary-disk-type spray drier (CL-12, Ohkawara Kakohki, Co., Ltd.) under a nitrogen atmosphere to avoid high-temperature oxidation of the magnetic powder. The rotational speed of the rotary disk was 14000 rpm. The inlet and outlet temperatures of the drying chamber were 70–100 °C and 50–75 °C, respectively.

Liquid-bound granules

A tumbling granulator (RMO-2H, Dalton Co., Ltd.) was used to prepare the liquid-bound granules. The primary particles were placed inside the granulator chamber under a nitrogen gas flow. Chopper rotation speed was 4700 rpm. The binding liquid was sprayed after the chamber was completely filled with nitrogen, and the chopper rotation speed was changed to 2300 rpm for 1 min for leveling the granule size.

4.3 Characterization techniques

Scanning electron microscopy (SEM) and optical microscopy were used for observing the granule morphology. A static angle of repose [214] was measured as the powder flowability indicator by a ABD powder peculiarity measuring instrument (Tsutsui Scientific Instruments Co., Ltd.). Using a vibrating mesh, the granules were dropped from a funnel onto a sample table with a diameter of 60 mm to form a conical pile, and thereafter, the angle between the pile peak and the table surface was determined. This process was repeated three times, and the

average value of the measured angles of repose was calculated (generally, a low angle of repose indicates a higher powder flowability).

Primary or secondary particles (granules) were placed in a transverse magnetic field of 1600 kA/m to produce compacts by uniaxial pressing under a pressure of 137 MPa. To prepare binder-bound granules, the debinding process of heating at 400 °C for 1 h in a hydrogen atmosphere was performed prior to the sintering procedure. The obtained compacts were sintered in vacuum (10^{-3} Pa) for 4 h in a temperature range of 1060–1080 °C and then annealed for 1 h at 850 °C followed by annealing for 1 h at 560 °C. The compacting process was conducted in air. The magnetic properties of the resulting specimens were evaluated using a B–H curve tracer (Tamakawa Co., Ltd.).

4.4 Results and discussions

4.4.1 Binder-bound granules

Generally, in the ceramic industry, spray-dried granule is used for the improvement of flowability of powder. PVA (Poly vinyl alcohol), which is easily dissolved in water, is often used as a binder. Therefore, the effect of this combination on the magnetic properties of the magnet was investigated. That is, the effect of the increase of oxygen and carbon by the binder addition on the sintering was examined.

Nd-Fe-B magnet powders usually contain hundreds to several thousand ppm oxygen and several hundred ppm carbon. The Nd-Fe-B magnet is manufactured under an atmosphere in which oxygen is reduced, but it is impossible to completely prevent the mixing of a small amount of oxygen, and oxidation to some extent is unavoidable. Lubricant is added in order to prevent fusing of the fine powders

when the alloy is pulverized and to reduce friction between the fine powders so that the fine powders are easily oriented during magnetic field molding. This is because carbon contained in the lubricant remains in the sintered magnet.

These oxygen and carbon combine with Nd metal to form oxides and carbides. Therefore, in order to form an appropriate grain boundary phase, the amount of oxide and carbide to be formed in advance is estimated, and a larger amount of rare earth element is added. When the grain boundary phase is insufficient, the magnetic separation between particles is not sufficiently performed, and the desired coercivity cannot be developed.

The Nd-Fe-B magnet powder used in this experiment has a composition design that can form an R-rich phase of 3 vol% even if the maximum oxidation and carbonization in the process are assumed (It is assumed that Nd binds preferentially to oxygen and carbon and the rest forms the $R_2Fe_{14}B$ and R-rich phases.) and more than 92 vol% of main phase ($Nd_2Fe_{14}B$) is remained. The magnet powder and PVA aqueous solution were mixed in a mortar, the particles were adjusted and dried. The amount of solid PVA added is 0.8 wt% based on the Nd-Fe-B magnet powder. They were pressed in magnetic field and sintered under usual conditions. As a result, the Nd-Fe-B magnet added with PVA was hardly

densified. A photograph of the sintered sample is shown in Figure 4-5 along with the sample without PVA.

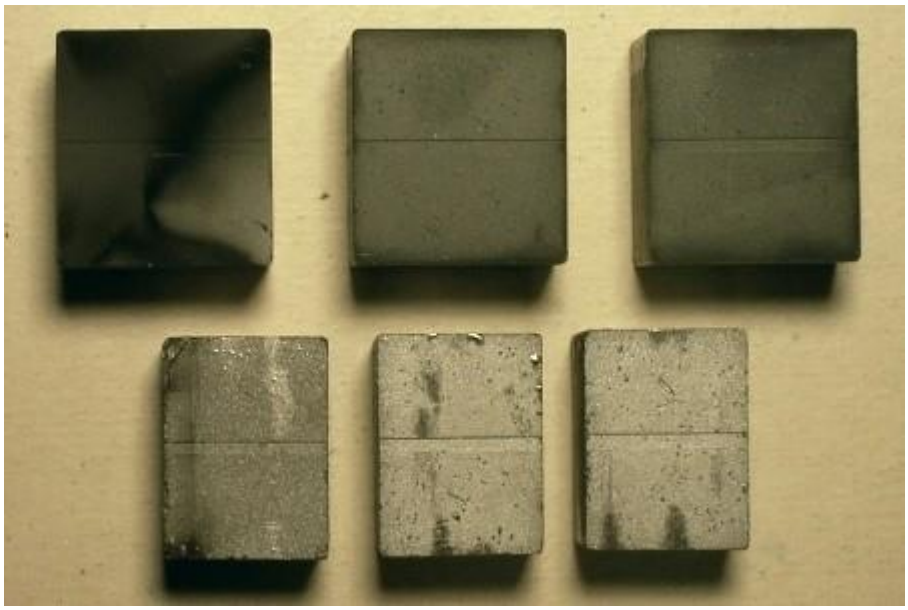

Figure 4-5 Image of sintered magnet prepared from magnet powder with (Upper) and without (Lower) PVA.

The size of the compact before sintering is almost the same. It can be seen that samples without PVA are densified by sintering, while samples with PVA are significantly inhibited from densification. The density of the compact and the sintered body, the amount of residual oxygen and carbon, and the magnetic

characteristics are shown in Table 4-1. As a comparison, Nd-Fe-B magnet powder without mixing PVA is also shown.

Table 4-1 Density, impurity content and magnetic properties of sintered materials from magnet powder with and without PVA.

	Density (g/cm^3)		Residual		B_r	H_{cJ}
	compact	sintered	O (ppm)	C (ppm)	(%)	(%)
PVA added	4.30	5.30	26540	3970	11.1	0.8
Non-added	4.36	7.63	4330	570	100	100

In the sample with PVA added, the amount of residual oxygen and carbon is obviously large, and the lowering of magnetic characteristics is remarkable. Based on these residual oxygen and carbon contents, the fraction of the forming phase was calculated. The results are listed in Table 4-2.

Table 4-2 Calculation results of the formation rate of each phase.

	Residual (ppm)		Phase (vol%)				
	O	C	Main phase	R-rich	Oxide	Carbide	others
PVA added	4330	570	91.0	4.7	3.2	0.6	0.5
Non-added	36540	3970	25.9	0.0	26.4	3.8	43.9

PVA added samples form large amounts of oxides and carbides, resulting in no R-rich phase formation. Therefore, it can be easily presumed that liquid phase sintering could not occur and sintering shortage occurred. Since the R-rich grain boundary phase does not form, the coercivity is hardly developed. Although the $Nd_2Fe_{14}B$ phase was formed by about 26%, it is presumed that the orientation of

the primary particles was hardly possible due to the strong bonding force by the binder. Since the residual magnetic flux density of the isotropic magnet is only half of that of the fully anisotropic magnet, the fact that the residual magnetic flux density of the PVA added sample is about 11% almost agrees with the calculation result.

In a series of papers published by Sumitomo Special Metals Co., Ltd. , the targets are 10,000 ppm of residual oxygen and 1000 pm of residual carbon [170], [171], [173]. If this amount of residual impurities is allowed and the amount of R-rich phase is maintained at the same level as that of the original design, the main phase ratio is reduced by about 5% [215]. That is, the residual magnetic flux density is also reduced by 5%. From this, it can be said that the increase in the amount of residual oxygen and carbon is unacceptable.

From these results, it was concluded that a process to remove oxygen and carbon was necessary in the binder-bound granules. First, it is necessary to select a dispersion medium that does not oxidize the Nd-Fe-B magnet powder, and then it is necessary to add a process for removing carbon. As the latter, the binder-bound granules were heated in a hydrogen atmosphere as a preliminary step thereafter. Because carbon is bonded to hydrogen by heat treatment, it can be removed from the system as methane gas.

In this procedure, ensuring proper dispersion medium selection is critical because the magnetic properties of the Nd-Fe-B magnetic powder deteriorate due to oxidation. Therefore, 3 g of the pulverized powder, which is shown in Figure 4-6,

was added to 8 cm^3 of various dispersion medium for 8 h; the resulting mixtures were kept uncovered and vacuum dried at a room temperature of 20 °C.

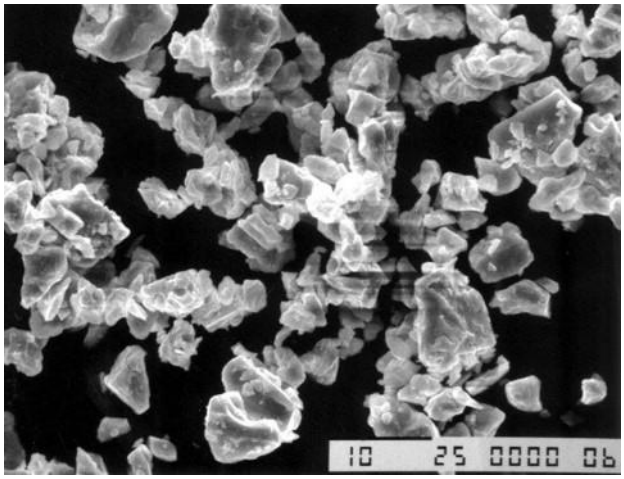

Figure 4-6 Typical primary powder of Nd-Fe-B magnet.

The oxygen contents in the solvent-treated and non-treated powders are listed in Table 4-3. Significant powder oxidation was observed after the treatment with deionized water [170]. Because toluene is less compatible with water than with ethanol, a lower degree of oxidation was expected for the toluene-treated powder. However, the degrees of oxidation obtained for the magnetic powders soaked in

toluene and ethanol were almost identical. Hence, ethanol was used as the organic solvent for the binder due to its lower cost.

Table 4-3 Oxygen contents in the magnetic powders immersed in various solvents.

	Non-immersed	Deionized water	Ethanol	Toluene
Oxygen (ppm)	3960	13130	5210	5160

Two types of the spray dried granules with a binder content of 0.8 wt.% were prepared: PVA in deionized water and PVB in ethanol. SEM images of these granules are shown in Figure 4-7. Their surfaces are not smooth due to the large size of the primary particles; however, no significant differences between the shapes of the two granules are observed. The average diameters of both granules are approximately 40 μm.

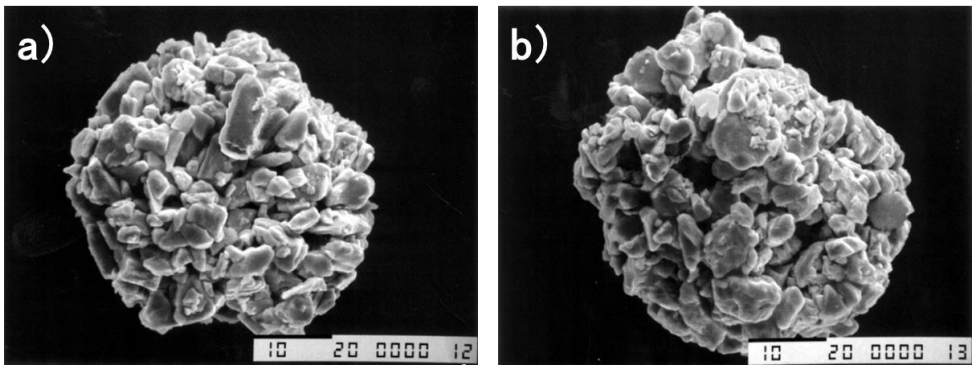

Figure 4-7 SEM images of a) PVA and b) PVB granules.

Despite the existence of several powder flowability indicators, including the Carr flowability index [214], [216], [217], the angle of repose is the most suitable

metric for estimating the flowability range of the primary and secondary particles in a magnet. The angles of repose of the spray dried granules and magnetic properties of the sintered magnets prepared from these granules are listed in Table 4-4 (here, the non-granulated powder is used as the reference). As described above, all the compacts were decarbonized by heat treatment in hydrogen before sintering. Both granule types have much smaller angles of repose than that of the non-granulated powder, indicating higher flowabilities; however, their magnetic properties, namely residual flux density and coercivity, are significantly degraded.

Table 4-4 Angles of repose of the spray dried granules and magnetic properties of the sintered magnets prepared from these granules.

	Angle of repose (°)	*Br* (%)	H_{cJ} (%)
Non-granulated	63	100	100
PVA+DIW	36.7	49.8	7.7
PVB+Ethanol	30.0	64.1	100.6

The PVA granules were not sufficiently densified and exhibited large deformation after sintering; as a result, their sintered density could not be measured. In contrast, the PVB granules were densified to a value exceeding 95% of their theoretical density. The particle oxidization in the PVA granules reduced the content of the R-rich phase and prevented sintering of the liquid phase [215]; it can also explain their low magnetic coercivity. Both granule types possessed extremely low values of the residual flux density, which was proportional to the relative density (ratio of actual to theoretical density) and degree of orientation. The PVB granules with high sintered density also exhibited a low residual magnetic flux density, which was likely caused by the low degree of orientation because the

particle bonding by the organic binder prevented the rotation of the primary particles against the applied magnetic field during pressing [218].

To increase the granule residual flux density, the binder content in the PVB granules was decreased to weaken the binding strength of each particle. The obtained relationship between the angle of repose and the relative residual flux density of the granules with PVB contents of 0.0 (non-granulated), 0.1, 0.3, 0.5, and 0.8 wt.% is presented in Figure 4-8, while the SEM images of these granules are displayed in Figure 4-9. According to Figure 4-8, the angle of repose decreases with increasing binder content, and the SEM observations show that the primary and secondary particles coexist in the granules with low PVB contents. From these results, it has been concluded that some granules collapse during the spray-drying process and that it is difficult to maintain the granular state at an organic binder concentration of 0.1 wt.% or less. The binding force of the organic binder cannot withstand external forces (such as the centrifugal and impact ones), which are applied to the granules during the spray drying process. The primary particles may easily rotate during the magnetic field pressing to achieve a higher residual flux density; however, the rotation of the secondary particles is hindered. Therefore, the residual magnetic flux density increased as the fraction of the primary particles increased.

To achieve the optimal residual flux density and flowability of the granules, the latter should be granulated by the relatively weak external forces. Furthermore, because the debinding heat treatment of the organic binder conducted under the

hydrogen atmosphere considerably increases the production cost, granules should be preferably densified under normal sintering conditions.

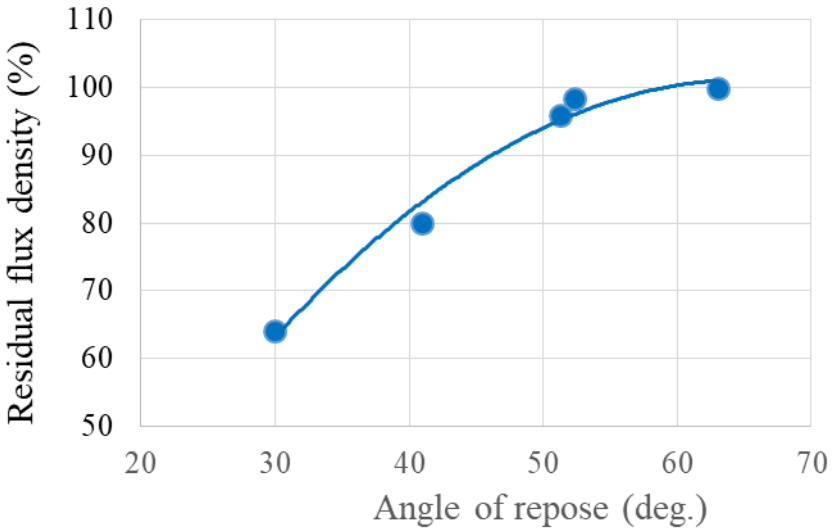

Figure 4-8 Relationship between the angle of repose and the relative residual flux density of the prepared granules.

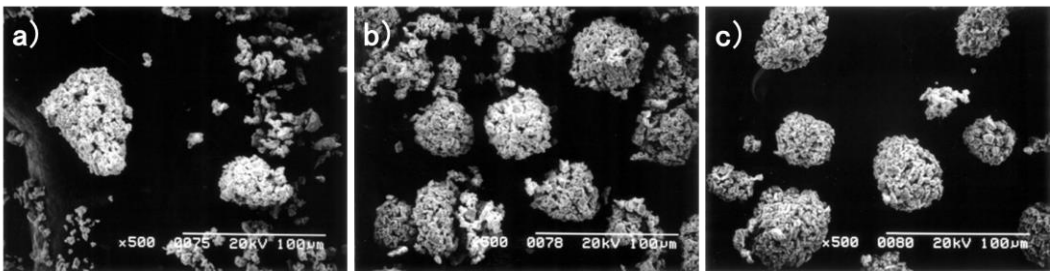

Figure 4-9 SEM images of the PVB granules with PVB contents of a) 0.10 wt.%, b) 0.30 wt.%, and c) 0.50 wt.%.

4.4.2 Liquid-bound granules

Because the primary particles must be bound to each other by a bonding force that is weaker than that of the organic binder, a liquid bridge force was used for this purpose [219]–[222]. Three liquids (ethanol, toluene, and terpineol) were selected based on their vapor pressures, which allowed them to easily debind during the sintering process; otherwise, the produced residual carbon might decrease the granule coercivity. The primary particles (100 g) and specific amounts of the liquid were mixed manually using a mortar to form granules. For uniform mixing, 12.5 wt.% of ethanol, 12.5 wt.% of toluene, and 6.25 wt.% of terpineol were added to the magnetic powder. Terpineol undergoes limited volatization during mixing; therefore, its content was much lower than those of ethanol and toluene. During mixing, the primary particles adsorbed the liquid and formed lumps through tumbling agglomeration [223]–[227], which were subsequently granulated. Since granule size affects flowability [228]–[232], a systematic comparison should be made by keeping the granule size at the same level for a systematic comparison to be made with readings of the same level of granule size. The obtained granules were sieved through 300 μm and 180 μm mesh sieves to select granules with intermediate sizes.

Table 4-5 lists the vapor pressures of all the liquids at 20 °C, concentrations of the residual oxygen and carbon elements, and angles of repose of the granules prepared from different liquids (the non-granulated powder was used as the reference).

Table 4-5 Vapor pressures of the utilized liquids at 20 °C, concentrations of the residual oxygen and carbon, and angles of repose of granules prepared from the corresponding liquids.

	Vapor pressure (mmHg)	O (ppm)	C (ppm)	Angle of repose (°)
Non-granulated	-	4360	790	63
Ethanol	44	5030	850	54
Toluene	22	4690	880	54
Terpineol	0.04	10940	2730	43

The granules prepared from ethanol and toluene contained low contents of carbon and oxygen residues, which likely resulted from the volatilization of the organic liquids. Further, these granules had smaller angles of repose than the non-granulated powder. In contrast, the granules prepared with terpineol had larger amounts of residual carbon and oxygen and a much smaller angle of repose than the non-granulated powder.

The granules were pressed in the presence of a magnetic field and sintered, after which the concentrations of the residual oxygen and carbon were measured, and the magnetic properties of the granules were determined. No special debinding procedure, such as heating under a hydrogen atmosphere, was performed for the spray dried granules.

The concentrations of residual elements and magnetic properties of the granules are listed in Table 4-6. The contents of the residual oxygen and carbon in each specimen were relatively low, indicating effective debinding of these species in the sintering process. This is very important to maintain high coercivity because it means that excess oxide and carbide which decrease the quantity of R-rich phase did not formed. The terpineol granules possessed a slightly higher carbon content, which reduced the granule and residual flux densities; however, no apparent

decrease in the magnetic coercivity was observed. Hence, the liquid-bound granules prepared using terpineol were most suitable for magnet fabrication in terms of flowability and magnetic properties.

Table 4-6 Residual oxygen and carbon contents, and magnetic properties of sintered magnets obtained from the granules treated with various liquids.

Mixed liquid	O (ppm)	C (ppm)	Density (g/cm^3)	B_r (%)	H_{cJ} (%)
Non-granulated	4360	580	7.59	100	100
Ethanol	4530	640	7.59	99.3	99.2
Toluene	4760	610	7.59	99.9	99.8
Terpineol	4680	690	7.56	97.5	99.7

Furthermore, to scale up the production of liquid-bound granules, the tumbling granulator specified in 4.2.2 was utilized (the spray drying method could not be applied to the liquid-bound granules because it would disintegrate them due to the weakness of the liquid bridge force). This apparatus contained a cylindrical chamber oriented in the horizontal direction, a mixing blade, two choppers, and a two-fluid nozzle inside the chamber. The powder placed in the chamber was scraped with the mixing blade and then dispersed and shredded with the two choppers to ensure uniform mixing with a low degree of segregation. The liquid was sprayed through the two-fluid nozzle using nitrogen gas. When its amount was too small, the liquid and the powder could not be uniformly mixed. Even using the granulator, it was still difficult to homogeneously mix the powder and the granulate with a terpineol content less than 6.25 wt.% (≈35 vol.%) because of its inability to reach the pendular state [224], [233]. However, the terpineol concentration of 6.25 wt.% was too high to obtain a high residual magnetic flux density. To achieve both the uniform mixing and high residual flux density, the

tumbling granulation process was performed by jetting a mixture of two liquids with different vapor pressures. Thereafter, only the liquid with the high vapor pressure was evaporated and removed from the liquid-bound granule in a vacuum dryer. By applying this method, the amount of terpineol required for achieving good magnetic properties of the liquid-bound granules can be accurately controlled while adding the required liquid amount.

The liquid-bound granules were prepared in the granulator by adding 2.0 wt.% of terpineol and 6.75 wt.% of ethanol to the magnetic powder at a jetting rate of 50 g/min. The vapor pressures of terpineol and ethanol differed by three orders of magnitude around room temperature as shown in Figure 4-10, and therefore, were suitable for the selective removal of the liquids through vacuum evaporation.

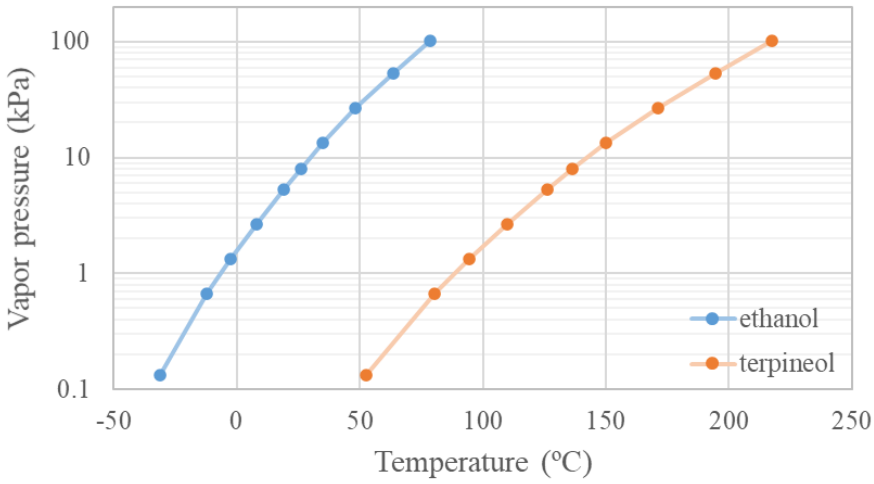

Figure 4-10 Vapor pressure of ethanol and terpineol as a function of temperature.

Granules larger than 425 μm were overcut using an automatic sieve. All granules size was reduced to 425 μm or less using tapping balls and passed through a sieve. The undercut was not performed. By this, all Nd-Fe-B magnet

powder was granulated, eliminating the need for disposal and recycling. Moreover, only ethanol was removed by vacuum drying and collected through a cold trap for further reuse in manufacturing liquid-bound granules. The angle of repose and photograph of the sieved liquid-bound granules obtained using the non-granulated powder as the reference are shown in Figure 4-11. Thus, liquid-bound granules were successfully granulated by utilizing the tumbling granulator and the automatic sieving machine as well as by manual mixing in a mortar.

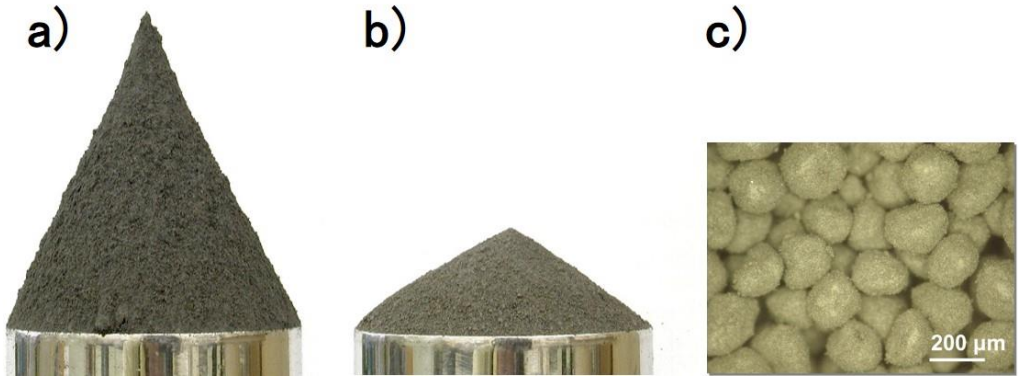

Figure 4-11 Angles of repose of the (a) original magnetic powder and (b) liquid-bound granule. (c) An optical image of the liquid-bound granule containing 2.0 wt.% of terpineol.

The granule size distributions obtained before and after sieving are shown in Figure 4-12. The sieved liquid-bound granules clearly exhibit a lower angle of repose than the non-sieved granules. During automatic sieving, more intense tumbling was applied to the granules because of the vibration of the sieve; as a result, fine granules with sizes <180 µm merged with the coarser granules, thus improving the size distribution.

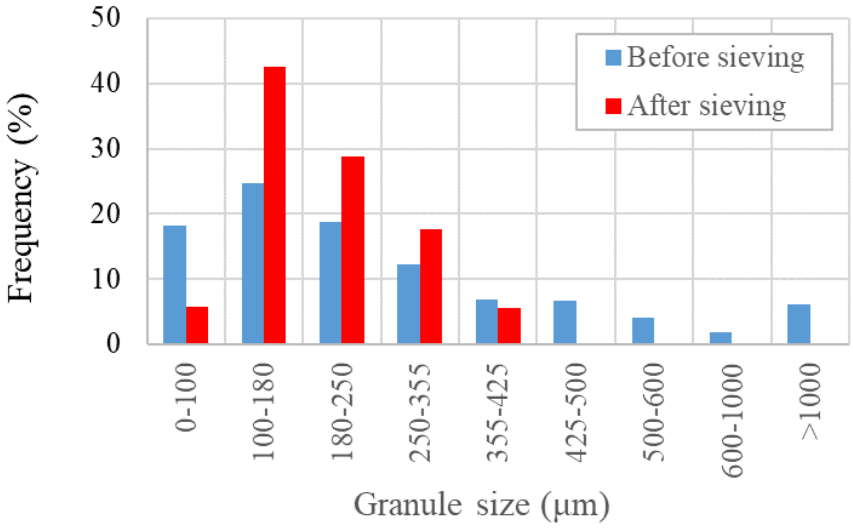

Figure 4-12 Granule size distributions obtained before and after sieving.

The angles of repose of the granules measured before and after sieving as well as the magnetic properties of the sintered magnets obtained from these granules are listed in Table 4-7. These results indicate that the angle of repose of the granules evidently decreased after sieving; however, a small reduction in the residual flux density was observed for the sintered magnets fabricated from these granules. This phenomenon was likely caused by the decrease in the number of the primary magnetic particles, which were easily rotated during magnetic field pressing. Furthermore, because the weight loss during sintering was approximately 2 wt.%, only ethanol species were effectively removed by the vacuum evaporation process.

Table 4-7 Angles of repose of granules obtained before and after sieving, and magnetic properties of the sintered magnets prepared from these granules.

	Angle of repose (°)	B_r (%)	H_{cJ} (%)
Non-granulated	63	100	100
Before sieving	52.3	98.6	99.4
After sieving	44.8	97.8	98.2

To increase the residual flux density of the sintered magnets, the terpinol concentration was decreased. A high jetting rate of the liquid was used (70 g/min) according to the results of previous studies, because for a higher jetting rate of the liquid, larger granule diameters were obtained, which increased the particle flowability. Automatic sieving was performed to overcut the granules with sizes larger than 450 µm. The angles of repose of the liquid-bound granules measured at different terpineol concentrations and the magnetic properties of the sintered magnets fabricated from these granules are listed in Table 4-8. Although the flowability of the granules and their residual flux density exhibit a reciprocal relationship, a higher residual magnetic flux density was obtained at a smaller angle of repose than that of the binder-bound granules. In the specified terpineol addition range, no changes in the coercivity of the sintered magnets were observed. At a terpineol concentration of approximately 0.25 wt.% (≈2.0 vol.%), both the high flowability and residual flux density (compared with those of the spray dried granules) were achieved. A 0.7% reduction in the residual magnetic flux density corresponds to 9 mT, which represents the grade of magnetic properties employed for the non-granulated material.

Table 4-8 Angles of repose of the terpineol-bound granules measured at different terpineol concentrations, and magnetic properties of the sintered magnets prepared from these granules.

Terpineol (wt%)	Angle of repose (°)	B_r (%)	H_{cJ} (%)
Non-granulated	63	100	100
0.125	44.2	99.6	98.5
0.25	44.2	99.3	99.3
0.5	42.7	98.8	99.7
1.0	42.2	98.6	99.0

Assuming that the primary particles are spheres having a diameter of 4 μm and that 0.25 wt% of terpineol is uniformly adhered to the surface of the primary particles, the thickness of the terpineol is calculated to be 0.0134 μm. This amount seems to be absolutely insufficient for liquid bridging. However, since the ethanol is evaporated after the mixed solution of terpineol and ethanol is added as described above and both are compatible, there is a high possibility that terpineol condenses at the contact point between the primary particles when the ethanol is evaporated. The amount of terpineol adhered to the primary particles having a diameter of 4 μm is 0.68 μm^3, and assuming that the terpineol have a sphere, the diameter of the terpineol is 1.16 μm, which is sufficiently large. The contact points between the particles are not considered to be one, but there is a possibility of sufficient liquid cross-linking. This suggests that the two-liquid mixing and one-liquid evaporation techniques help to effectively place terpineol.

The relationship between the angle of repose and the residual magnetic flux density of the sintered bodies prepared from them for liquid-bound granules and various binder-bound granules prepared from them is shown in Figure 4-13. It can be seen that liquid-bound granules have both higher levels of flowability and magnetic properties than binder-bound granules. The use of liquid-bound granules

instead of binder-bound granules is required to achieve the magnetic properties required for practical magnets.

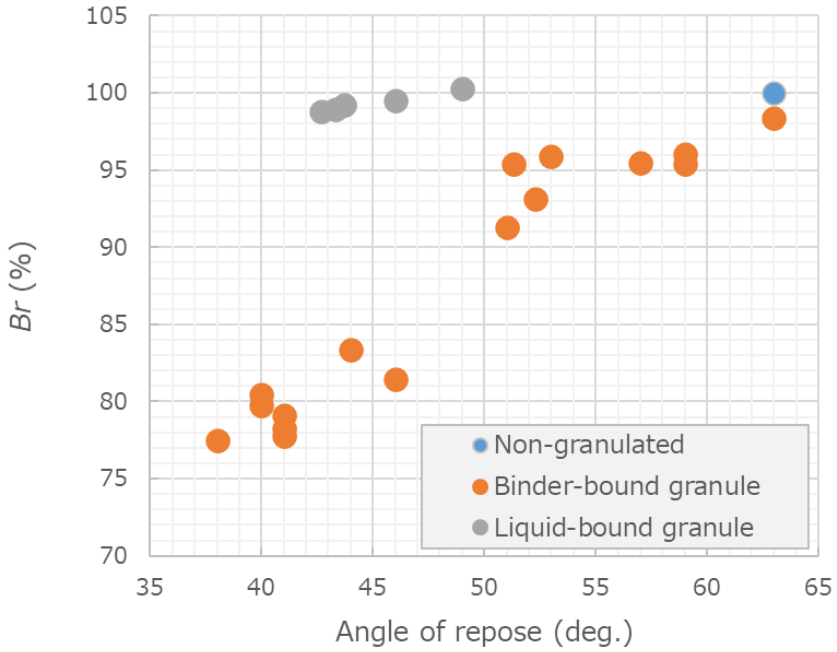

Figure 4-13 Relationship between angle of repose in various granules and residual magnetic flux density of sintered magnets prepared from them.

3.3 Flowability evaluation on a mass production line

Using a mass production uniaxial pressing machine, weight variations of the pressed powder fraction were investigated. During the mass production process, the powder filling rate must be sufficiently high, while the weight variations of the filled part should be small. Filling a constant volume requires a constant bulk density of the powder. The utilized die contained two cavities with opening dimensions of 5 mm × 14 mm and filling depth of approximately 60 mm.

A powder feeder box was moved back and forth above the cavity, causing the powder to fall naturally onto its top. The time required for powder filling was determined, and pressing was performed 50 times under the same conditions. The variation σ and average avg of the weight for the two compacts in the two cavities were obtained and the ratio of the variation to the average σ/avg was calculated every pressing. The ratio σ/avg was averaged for 50 pressings to obtain the intra-pressure weight variation in a single pressing. The standard deviation and mean of the average weight avg for the two compacts in one pressing were calculated from 50 pressing and the ratio of the standard deviation to the mean was calculated to evaluate the inter-pressing weight variation in a number of pressing. Table 4-9 lists the average of the weight variations for the two cavities over 50 measurements. The liquid-bound granules exhibited smaller feed times and weight variations than those of the non-granulated powder. Thus, the high flowability of the granules facilitated the narrow cavity filling.

Table 4-9 Feed times and weight variations of the pressed part.

		Variation: δ/avg. (%)	
	Feed time (s)	Intra-pressing	Inter-pressing
Non-granulated	34	4.55	5.79
Tumble granulated	7	0.82	1.08

The magnet having the shape shown in Figure 4-14 (a) was manufactured by a mass production process using granules. The orientation field was 1.2 T. The filling depth was as deep as 70 mm or more, and insufficient orientation of the lower part of the sample due to its own weight was a concern. Therefore, the orientation state was confirmed using electron backscatter diffraction (EBSD). The C-plane was observed on the upper, central, and lower portions of the sample

shown in Figure 4-14 (b). The observation position is the center in the width direction of the sample, and is 5 mm from the top, the center of the sample, and 5 mm from the bottom with respect to the filling depth direction, respectively.

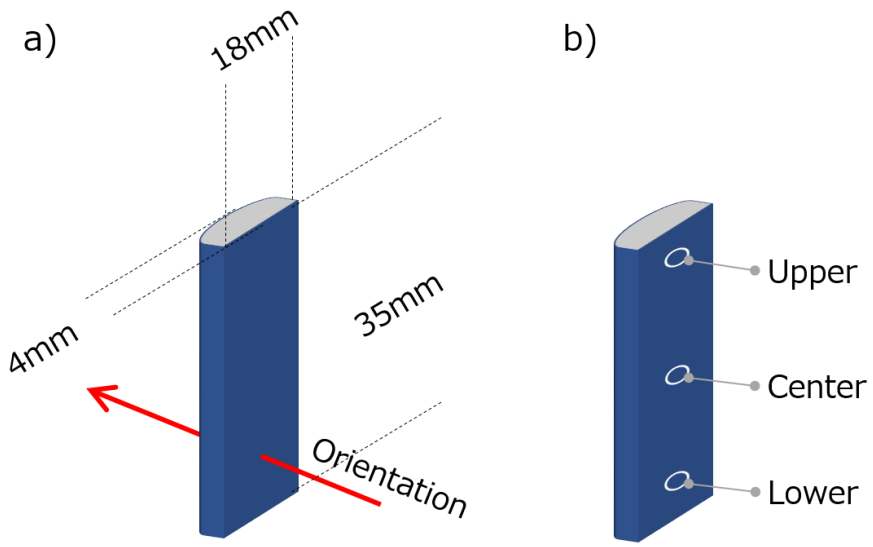

Figure 4-14 EBSD measurement sample:

a) sample shape and dimension, b) measurement position.

The results are shown in Figure 4-15. The size of one observation region is 240 × 240 μm. The deviation to the (001) direction which is the C axis is visualized. It can be seen that, regardless of the observation position of the sample, the crystal maintains the same degree of orientation. When cosines in the direction of the C-axis were calculated from the mean deviation angle of the orientation, they were 96.2, 96.8, and 95.9% in the upper part, the center part, and the lower part of the sample, respectively, with an error within 1%. Although the molding was carried out under a relatively low magnetic field of 1.2 T, it can be said that the degree of orientation is kept high as an absolute value.

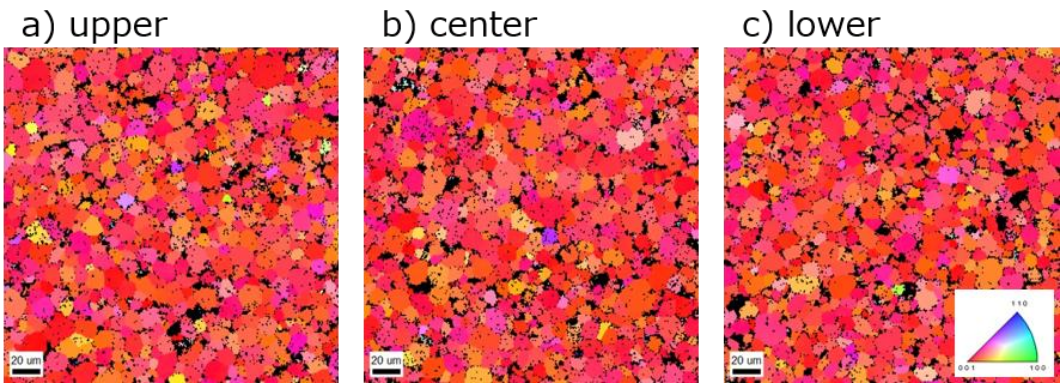

Figure 4-15 Orientation of sintered magnets made from granules.

In summary, liquid-bound granules were formed by the weak bonding force called the liquid bridge force, and the bonds between their particles were easily broken by the magnetic field applied during magnetic field pressing. The utilization of these liquid-bound granules in the mass production of magnets facilitated the stable filling of small cavities with magnetic materials, thus reducing the amount of rare-earth material waste.

4.5 Conclusion

In order to reduce the amount of rare earth elements, such as Nd, Pr, Dy and Tb, discarded by processing during the manufacture of sintered magnets, the realization of granules with high flowability that can withstand near-net shaping was investigated. It is necessary to secure flowability by granulating the magnet powder, and to have high magnetic properties, that is, high coercivity and high residual magnetic flux density, of the sintered magnet produced by using the granules.

First, binder-bound granule was prepared. In order to form the R-rich phase which sufficiently develops the coercivity, the slurry composition which avoids

oxidation and the step of removing the binder were indispensable. Then binder-bound granules were prepared by the spray drying method using ethanol as the solvent and PVB as the binder, and before sintering PVB was debound by heating in hydrogen atmosphere. The low concentrations of PVB increased the angle of repose serving as the flowability index, while increasing the powder flowability in the binder-bound granules negatively affected their residual magnetic flux density.

Thereafter, the liquid-bound granules based on the liquid bridge force were prepared. In this process, terpineol was used as the liquid due to its low volatility at room temperature and ability to be easily debind during sintering without hydrogen debinding process. Increasing the terpineol content in the prepared liquid-bound granules noticeably increased their flowability. A negative correlation between the flowability and residual magnetic flux density was also observed for these granules; however, they exhibited much higher residual flux densities and lower angles of repose than the binder-bound granules. The liquid-bound granules containing 0.25 wt.% terpineol had a repose angle of 44.2° and relative coercivity and residual magnetic flux density equal to 99.3 % of the value obtained for the non-granulated powder.

During the mass production of these granules using a narrow deep die, a high filling rate and low granule weight variations were achieved. As a result, near-net shape forming is possible without deterioration of magnetic characteristics. Depending on the shape of the magnet, 34% to 68% reduction of Nd, Pr, Dy and Tb waste is possible in the arc type magnet.

Chapter 5 General conclusions

An attempt was made to extrinsically improve the coercivity by controlling the microstructure, i.e., the grain boundary phases. Conventionally, the coercivity of the Nd-Fe-B magnet has been able to exhibit only 20% or less (typically 15%) of the anisotropy field. The introduction of new grain boundary phases was effective for the improvement of coercivity, and the formation mechanism, magnetic properties, and effect mechanism on coercivity of these grain boundary phases were clarified. By improving coercivity, the use of rare earth elements Nd, Pr, Dy and Tb, which have been inevitably used in large quantities, can be reduced as a result. The results of this study are summarized below;

In the study of the reduction of Dy and Tb, the introduction of $Nd_6Fe_{13}Ga$ grain boundary phase by Ga addition was tried. The formation of $Nd_6Fe_{13}Ga$ grain boundary phase was confirmed not only at the triple junction but also at the thin grain boundary phase, and how this phase was formed during heat treatment was clarified. Since the $Nd_6Fe_{13}Ga$ phase was formed by consuming Fe contained in the main phase and R-rich grain boundary phase, this phase was easily formed as a thin grain boundary phase. The magnetization of this phase was investigated and found for the first time to be 0.05 T, which is much lower than that of $Nd_2Fe_{14}B$ particles. The formation of the $Nd_6Fe_{13}Ga$ grain boundary phase promoted the penetration of the R-rich phase into grain boundary, and also played the important role of lowering the magnetization of the R-rich phase itself. The main reason for the enhancement of coercivity was that the low-magnetization grain boundary phase enveloped the grains, creating magnetic isolation between each grain. As a result, a coercivity of 1998 kA/m was achieved in the Nd-Fe-B magnet without Dy and Tb. This value corresponds to 35% of the anisotropy field, and the potential of

the Nd-Fe-B magnet was successfully improved by the extrinsic method of grain boundary control. The reduction effect of Dy and Tb by this is worth 75%.

In the reduction study of Nd and Pr, the introduction of $R_6Fe_{13}Ga$ grain boundary phase by Ga addition was tried in R-Fe-B sintered magnets substituted with Ce. (where R is a plurality of rare earths including those other than Nd, Pr, Dy and Tb) When less than 1 wt% of Ga was added, the $R_6Fe_{13}Ga$ phase was not formed, and the RFe_2 phase and the R-rich phase were formed. When more than 1 wt% of Ga was added, the $R_6Fe_{13}Ga$ phase was successfully formed, but the coercivity decreased. The high magnetization of 0.15T of the $R_6Fe_{13}Ga$ phase, which was 3 times higher than that of $Nd_6Fe_{13}Ga$ and low coverage rate of grain by grain boundary, suggested that this high magnetization did not contribute to the sufficient magnetic separation between grains. It was found that the magnetization of the RFe_2 phase decreases with increasing Ce concentration, an attempt was made to increase the Ce concentration in the RFe_2 phase. However, an increase in the Ce concentration caused a decrease in the sintering temperature and an enhancement of abnormal grain growth, indicating that there is a suitable concentration range. As a result of the examination, the optimum magnetic isolation condition of the grain was produced in the concentration range where the coverage of the grain can be highest, and it succeeded in obtaining the coercivity of 1063 kA/m. This value corresponds to 28% of the anisotropy field, and the potential of the R-Fe-B magnet was successfully improved by the extrinsic method of grain boundary control. The reduction effect of Nd and Pr by this process is more than 50%.

A new near-net shaping method was introduced to reduce the amount of cutting and polishing waste discarded in the magnet manufacturing process. An unprecedented granulation technique has been established to prevent oxidation and carbonization of grain boundary phases, which is also applicable to the above

new grain boundary phases introduced magnet. A new concept of liquid bound granules using the liquid cross-linking ability of liquids was introduced, and a process to achieve this was established. Thus, oxidation and carbonization of the granules are prevented, and the sintered magnet is successfully obtained without damaging the grain boundary phase. The reduction effect of Nd, Pr, Dy and Tb due to this depends on the shape of the magnet, however reaches 34-68 % in the assumed SPM magnet. Further reduction effect is obtained by combining this technique with a Ga-added magnet or a Ce-added magnet.

References

[1] Yogoro Kato and Takeshi Takei, “亜鉄酸亜鉛の組成化学的性質及び磁性に関する研究,” 日本鑛業會誌, vol. 539, pp. 167–176, 1930.

[2] Y. Tawara and K. Strnat, “Rare earth-cobalt permanent magnets near the 2–17 composition,” *IEEE Transactions on Magnetics*, vol. 12, no. 6, pp. 954–958, 1976, doi: 10.1109/TMAG.1976.1059138.

[3] K. Ohashi, “Present and future of Sm_2Co_{17} magnets,” *The journal of the Japan Institute of Metals and Materials*, vol. 76, no. 1, pp. 97–106, 2012.

[4] T. Yoneyama, T. Hori, and T. Ojima, “Development of high performance precipitation hardened rare earth cobalt magnets,” 日本金属学会会報, vol. 26, no. 5, pp. 428–430, 1987.

[5] J. J. Croat, J. F. Herbst, R. W. Lee, and F. E. Pinkerton, “High-energy product Nd-Fe-B permanent magnets,” *Applied Physics Letters*, vol. 44, no. 1, pp. 148–149, 1984, doi: 10.1063/1.94584.

[6] J. J. Croat, J. F. Herbst, R. W. Lee, and F. E. Pinkerton, “Pr-Fe and Nd-Fe-based materials: A new class of high-performance permanent magnets (invited),” *Journal of Applied Physics*, vol. 55, no. 6, pp. 2078–2082, 1984, doi: 10.1063/1.333571.

[7] M. Sagawa, K. Hiraga, H. Yamamoto, and Y. Matsuura, “Permanent magnet materials based on the rare earth-iron-boron tetragonal compounds,” *IEEE Transactions on Magnetics*, vol. 20, no. 5, pp. 1584–1589, 1984, doi: 10.1109/TMAG.1984.1063214.

[8] Y. Matsuura, S. Hirosawa, H. Yamamoto, S. Fujimura, and M. Sagawa, “Magnetic properties of the $Nd_2(Fe_{1-x}Co_x)14B$ system,” *Applied Physics Letters*, vol. 46, no. 3, pp. 308–310, 1985, doi: 10.1063/1.95668.

[9] Masato Sagawa, Satoshi Hirosawa, Hitoshi Yamamoto, Setsuo Fujimura, and Yutaka Matsuura, “Nd-Fe-B Permanent Magnet Materials,” *Japanese Journal of Applied Physics*, vol. 26, pp. 785–800, 1987.

[10] M. Sagawa and H. Nagata, “Novel Processing Technology for Permanent Magnets,” *IEEE Transactions on Magnetics*, vol. 29, no. 6, pp. 2747–2751, 1993.

[11] K. Yamamoto and R. Murakami, “Microstructure formation on NdFeB ternary alloy system for magnet by strip casting method,” *The journal of the Japan Institute of Metals and Materials*, vol. 80, no. 1, pp. 1–6, 2016, doi: 10.2320/jinstmet.JB201501.

[12] A. G. Popov *et al.*, “Effect of additions of zinc stearate on the properties of sintered Nd-Fe-B magnets,” *Physics of Metals and Metallography*, vol. 114, no. 4, pp. 285–294, Apr. 2013, doi: 10.1134/S0031918X13040066.

[13] J. F. Herbst, “$R_2Fe_{14}B$ materials Intrinsic properties and technological aspects,” *Reviews of Modern Physics*, vol. 63, no. 4, pp. 819–898, 1991.

[14] R. Skomski and J.M.D. Coey, *Permanent Magnetism*. Bristol, U.K.: Institute of Physics, 1999.

[15] Y. Matsuura, “Recent development of Nd-Fe-B sintered magnets and their applications,” *Journal of Magnetism and Magnetic Materials*, vol. 303, no. 2 SPEC. ISS., pp. 344–347, 2006, doi: 10.1016/j.jmmm.2006.01.171.

[16] H. Kato, “Nd-Fe-B Role of Rare-Earth Elements in Permanent Magnet Materials,” 電機製鋼, vol. 73, no. 4, pp. 255–262, 2002.

[17] H. F. Schmidts, G. Martinek, and H. Kronmfiller, “Recent progress in the interpretation of nucleation fields of hard magnetic particles,” *Journal of Magnetism and Magnetic Materials*, vol. 104, pp. 1119–1120, 1992.

[18] K. Hono, T. Ohkubo, and H. Sepehri-Amin, “Microstructure-Coercivity Relationships of Nd-Fe-B Base Permanent Magnets,” 日本金属学会誌, vol. 76, no. 1, pp. 2–11, 2012.

[19] X. B. Liu and Z. Altounian, “The partitioning of Dy and Tb in NdFeB magnets: A first-principles study,” *Journal of Applied Physics*, vol. 111, no. 7, pp. 07A701-1-07A701-3, Apr. 2012, doi: 10.1063/1.3670054.

[20] M. v. Reimer, H. Y. Schenk-Mathes, M. F. Hoffmann, and T. Elwert, “Recycling decisions in 2020, 2030, and 2040 -when can substantial NdFeB extraction be expected in the EU?,” *Metals*, vol. 8, no. 11, Nov. 2018, doi: 10.3390/met8110867.

[21] Shinichiro Morimoto and Yuna Seo, “Current Trend of Medium - Long Term Rare Earth Demand Forecast,” *Journal of the Mining and Materials Processing Institute of Japan*, vol. 130, pp. 219–224, 2014.

[22] M. Schmid, “Rare Earths in the Trade Dispute Between the US and China: A Déjà Vu,” *Intereconomics*, vol. 54, no. 6, pp. 378–384, Nov. 2019, doi: 10.1007/s10272-019-0856-6.

[23] Ishihara Shunso and Murakami Hiroyasu, “Ore deposit types for rare earth element resources,” *Chishitsu News*, vol. 624, pp. 10–29, 2006.

[24] M. Ohashi, “The present and the future of rare earth resources predicted from its supply and demand,” *IEEJ Transactions on Fundamentals and Materials*, vol. 136, no. 8, pp. 491–494, 2016, doi: 10.1541/ieejfms.136.491.

[25] H. Paulick and E. Machacek, “The global rare earth element exploration boom: An analysis of resources outside of China and discussion of development perspectives,” *Resources Policy*, vol. 52, pp. 134–153, Jun. 2017, doi: 10.1016/j.resourpol.2017.02.002.

[26] T. Takagi, “Present states and issues on the development of rare earths resources,” *The Clay Science Society of Japan*, vol. 50, no. 3, pp. 123–127, 2012.

[27] P. C. Dent, “Rare earth elements and permanent magnets,” *Journal of Applied Physics*, vol. 111, no. 7, pp. 07A721-1-07A721-7, Apr. 2012, doi: 10.1063/1.3676616.

[28] Masaharu Kamitani, “Rare-Earth resources of the world,” *Mining Geology*, vol. 39, no. 2, pp. 140–148, 1989.

[29] M. A. Müller, D. Schweizer, and V. Seiler, “Wealth Effects of Rare Earth Prices and China’s Rare Earth Elements Policy,” *Journal of Business Ethics*, vol. 138, no. 4, pp. 627–648, Nov. 2016, doi: 10.1007/s10551-015-2773-3.

[30] M. S. Jaroni, B. Friedrich, and P. Letmathe, “Economical feasibility of rare earth mining outside China,” *Minerals*, vol. 9, no. 10, Oct. 2019, doi: 10.3390/min9100576.

[31] Yosuke Kawata, “Rare earth resources development and its NORM radiation protection,” *Japanese Journal of Health Physics*, vol. 49, no. 2, pp. 88–97, 2014.

[32] J. Kobayashi, H. Seto, and T. Mori, “The separation and Purification of Rare-Earth Elements,” *Resources Processing*, vol. 37, no. 3, pp. 157–164, 1990.

[33] K. Fukuda, H. Hara, K. Nawata, and B. Assistant, “The Relationship between Changes in China’s Export Policy and Rare Earth Prices,” *Journal of the Mining and Materials Processing Institute of Japan*, vol. 126, no. 6, pp. 8–19, 2010.

[34] Y. Yang *et al.*, “REE Recovery from End-of-Life NdFeB Permanent Magnet Scrap: A Critical Review,” *Journal of Sustainable Metallurgy*, vol. 3, no. 1. Springer, pp. 122–149, Mar. 01, 2017, doi: 10.1007/s40831-016-0090-4.

[35] Y. Zhang, F. Gu, Z. Su, S. Liu, C. Anderson, and T. Jiang, “Hydrometallurgical recovery of rare earth elements from ndfeb permanent magnet scrap: A review,” *Metals*, vol. 10, no. 6. MDPI AG, pp. 1–34, Jun. 01, 2020, doi: 10.3390/met10060841.

[36] M. Humphries, “CRS Report for Congress Rare Earth Elements: The Global Supply Chain Rare Earth Elements: The Global Supply Chain Congressional Research Service,” 2013. [Online]. Available: www.crs.gov.

[37] J. M. D. Coey, “Perspective and Prospects for Rare Earth Permanent Magnets,” *Engineering*, vol. 6, no. 2, pp. 119–131, Feb. 2020, doi: 10.1016/j.eng.2018.11.034.

[38] J. Geng, H. Hao, X. Sun, D. Xun, Z. Liu, and F. Zhao, “Static material flow analysis of neodymium in China,” *Journal of Industrial Ecology*, pp. 1–11, 2020, doi: 10.1111/jiec.13058.

[39] R. Skomski and J. M. D. Coey, “Magnetic anisotropy - How much is enough for a permanent magnet?,” *Scripta Materialia*, vol. 112, pp. 3–8, Feb. 2016, doi: 10.1016/j.scriptamat.2015.09.021.

[40] R. Ramesh, G. Thomas, and B. M. Ma, “Magnetization reversal in nucleation controlled magnets. II. Effect of grain size and size distribution on intrinsic coercivity of Fe-Nd-B magnets,” *Journal of Applied Physics*, vol. 64, no. 11, pp. 6416–6423, 1988, doi: 10.1063/1.342055.

[41] D. W. Scott, B. M. Ma, Y. L. Liang, and C. O. Bounds, “Microstructural control of NdFeB cast ingots for achieving 50 MGOe sintered magnets,” *Journal of Applied Physics*, vol. 79, no. 8 PART 2A, pp. 4830–4832, Apr. 1996, doi: 10.1063/1.361622.

[42] K. Uestuener, M. Katter, and W. Rodewald, “Dependence of the Mean Grain Size and Coercivity of Sintered Nd-Fe-B Magnets on the Initial Powder Particle Size,” *IEEE Transactions on Magnetics*, vol. 42, no. 10, pp. 2897–2899, 2006, doi: 10.1109/TMAG.2006.879889.

[43] W. F. Li, T. Ohkubo, K. Hono, and M. Sagawa, “The origin of coercivity decrease in fine grained Nd-Fe-B sintered magnets,” *Journal of Magnetism and Magnetic Materials*, vol. 321, pp. 1100–1105, Apr. 2009, doi: 10.1016/j.jmmm.2008.10.032.

[44] Yasuhiro Une and Masato Sagawa, “Enhancement of Coercivity of Nd-Fe-B Sintered Magnets by Grain Size Reduction,” *Journal of the Japan Institute of Metals and Materials*, vol. 76, no. 1, pp. 12–16, 2012.

[45] T. T. Sasaki, T. Ohkubo, Y. Une, H. Kubo, M. Sagawa, and K. Hono, “Effect of carbon on the coercivity and microstructure in fine-grained Nd-Fe-B sintered magnet,” *Acta Materialia*, vol. 84, pp. 506–514, Feb. 2015, doi: 10.1016/j.actamat.2014.10.047.

[46] T. T. Sasaki *et al.*, “Formation of non-ferromagnetic grain boundary phase in a Ga-doped Nd-rich Nd-Fe-B sintered magnet,” *Scripta Materialia*, vol. 113, pp. 218–221, 2016, doi: 10.1016/j.scriptamat.2015.10.042.

[47] X. D. Xu *et al.*, “Origin of the coercivity difference in Nd-Fe-B sintered magnets processed from hydrogenation-disproportionation-desorption- recombination powder and jet-milled powder,” *Acta Materialia*, vol. 151, pp. 293–300, Jun. 2018, doi: 10.1016/j.actamat.2018.03.062.

[48] G. Herzer, “Grain size dependence of coercivity and permeability in nanocrystalline ferromagnets,” *IEEE TRANSACTIONS ON MAGNETICS*, vol. 26, no. 5, pp. 1397–1402, 1990.

[49] K. Kobayashi, “Mechanism of Magnetization Reversal in Permanent Magnets,” *Materia Japan*, vol. 42, no. 5, pp. 405–412, 2003.

[50] T. Ohkubo, H. Sepehri-Amin, and K. Hono, “Micromagnetic Simulations of Magnetization Reversals in Nd-Fe-B Based Permanent Magnets,” *Journal of the Japan Institute of Metals*, vol. 81, no. 1, pp. 11–18, 2017, doi: 10.2320/jinstmet.JA201602.

[51] R. Ramesh and K. Srikrishna, “Magnetization reversal in nucleation controlled magnets. I. Theory,” *Journal of Applied Physics*, vol. 64, no. 11, pp. 6406–6415, 1988, doi: 10.1063/1.342054.

[52] T. T. Sasaki *et al.*, “Formation of non-ferromagnetic grain boundary phase in a Ga-doped Nd-rich Nd-Fe-B sintered magnet,” *Scripta Materialia*, vol. 113, pp. 218–221, 2016, doi: 10.1016/j.scriptamat.2015.10.042.

[53] R. Goto, M. Matsuura, S. Sugimoto, N. Tezuka, Y. Une, and M. Sagawa, “Microstructure evaluation for Dy-free Nd-Fe-B sintered magnets with high coercivity,” *Journal of Applied Physics* , vol. 111, no. 7, pp. 07A739-1-07A739-3, Apr. 2012, doi: 10.1063/1.3680190.

[54] Y. Une *et al.*, “Grain Size Refinement of Ga-doped Nd-Fe-B Magnet,” 2017.

[55] Toshihiko Shakouchi, “粉粒体のジェット粉砕と分級,” ターボ機械, vol. 24, no. 13, pp. 13–18, 1996.

[56] Mitsuhiko Satoh, Siichi Kaneko, Mutuwo Tomita, Shinji Doki, and Shigeru Okuma, “Development of IPM motors for compressors of air-conditioners,” 愛知電機技報, vol. 30, pp. 28–33, 2009.

[57] Y. Ogawa, H. Tokoro, and S. Tanigawa, “Recent Development of Sintered R-Fe-B Permanent Magnets for Motor Applications,” *J. Jpn. Soc. Powder Powder Metallurgy*, vol. 50, no. 11, pp. 894–898, 2003.

[58] H. Sepehri-Amin, Y. Une, T. Ohkubo, K. Hono, and M. Sagawa, “Microstructure of fine-grained Nd-Fe-B sintered magnets with high coercivity,” *Scripta Materialia*, vol. 65, pp. 396–399, Sep. 2011, doi: 10.1016/j.scriptamat.2011.05.006.

[59] K. Hono and H. Sepehri-Amin, “Strategy for high-coercivity Nd-Fe-B magnets,” *Scripta Materialia*, vol. 67, pp. 530–535, Sep. 2012, doi: 10.1016/j.scriptamat.2012.06.038.

[60] S. Bance, J. Fischbacher, and T. Schrefl, “Thermally activated coercivity in core-shell permanent magnets,” *Journal of Applied Physics*, vol. 117, no. 17, pp. 17A733-1-17A733-4, May 2015, doi: 10.1063/1.4916542.

[61] S. Sugimoto, “Development of High Coerecive NdFeB Sintered Magnets without Dy Addition,” *J. Japan Inst. Metals*, vol. 71, no. 10, pp. 850–852, 2007.

[62] M. Honshima and K. Ohashi, “High-Energy NdFeB Magnets and Their Applications,” *Journal of Materials Engineering and Performance*, vol. 3, no. 2, pp. 218–222, 1994.

[63] Satoshi Sugimoto, “永久磁石材料の最近の研究,” *Materia Japan*, vol. 56, no. 3, pp. 181–185, 2017.

[64] M. Nakamura, “Rare Metal Problems, their background and some technologies for countermeasure against them,” 精密工学会春季大会学術講演会講演論文集, pp. 353–354, 2011.

[65] K. Hirota, H. Nakamura, T. Minowa, and M. Honshima, “Coercivity Enhancement by the Grain Boundary Diffusion Process to Nd-Fe-B Sintered Magnets,” *IEEE Transactions on Magnetics*, vol. 42, no. 10, pp. 2909–2911, 2006, doi: 10.1109/TMAG.2006.879906.

[66] T. Oikawa, H. Yokota, T. Ohkubo, and K. Hono, “Large-scale micromagnetic simulation of Nd-Fe-B sintered magnets with Dy-rich shell structures,” *AIP Advances*, vol. 6, no. 5, May 2016, doi: 10.1063/1.4943058.

[67] T. H. Kim *et al.*, “Formation mechanism of Tb-rich shell in grain boundary diffusion processed Nd–Fe–B sintered magnets,” *Scripta Materialia*, vol. 178, pp. 4333–437, Mar. 2020, doi: 10.1016/j.scriptamat.2019.12.002.

[68] W. Tang, K. W. Dennis, M. J. Kramer, I. E. Anderson, and R. W. McCallum, “Studies of sintered MRE-Fe-B magnets by DyF_3 addition or diffusion treatment (MRE=Nd+Y+Dy),” in *Journal of Applied Physics*, Apr. 2012, vol. 111, no. 7, doi: 10.1063/1.3679465.

[69] H. Nakamura, K. Hirota, T. Minowa, and M. Honshima, “Coercivity of Nd-Fe-B sintered magnets produced by the grain boundary diffusion process with various rare-earth compounds,” *Journal of the Magnetics Society of Japan*, vol. 31, pp. 6–11, 2007.

[70] L. ZHOU, J. LI, X. CHENG, T. LIU, X. YU, and B. LI, “Dy gradient and coercivity in grain boundary diffusion processed Nd-Fe-B magnet,” *Journal of Rare Earths*, vol. 35, no. 6, pp. 559–566, Jun. 2017, doi: 10.1016/S1002-0721(17)60948-7.

[71] H. Sepehri-Amin, T. Ohkubo, and K. Hono, “Grain boundary structure and chemistry of Dy-diffusion processed Nd–Fe–B sintered magnets,” *Journal of Applied Physics*, vol. 107, no. 9, pp. 09A745-1-09A745-3, May 2010, doi: 10.1063/1.3351247.

[72] H. Sepehri-Amin, T. Ohkubo, and K. Hono, “The mechanism of coercivity enhancement by the grain boundary diffusion process of Nd-Fe-B sintered magnets,” *Acta Materialia*, vol. 61, no. 6, pp. 1982–1990, Apr. 2013, doi: 10.1016/j.actamat.2012.12.018.

[73] R. S. Mottram, A. J. Williams, and I. R. Harris, “The effects of blending additions of copper and cobalt to $Nd_{16}Fe_{76}B_8$ milled powder to produce sintered magnets,” *Journal of Magnetism and Magnetic Materials*, vol. 234, pp. 80–89, 2001.

[74] W. F. Li, T. Ohkubo, and K. Hono, “Effect of post-sinter annealing on the coercivity and microstructure of Nd-Fe-B permanent magnets,” *Acta Materialia*, vol. 57, pp. 1337–1346, Mar. 2009, doi: 10.1016/j.actamat.2008.11.019.

[75] F. Vial, F. Joly, E. Nevalainen, M. Sagawa, K. Hiraga, and K. T. Park, “Improvement of coercivity of sintered NdFeB permanent magnets by heat treatment,” *Journal of Magnetism and Magnetic Materials*, vol. 242, pp. 1329–1334, 2002.

[76] H. Sepehri-Amin, T. Ohkubo, T. Shima, and K. Hono, “Grain boundary and interface chemistry of an Nd-Fe-B-based sintered magnet,” *Acta Materialia*, vol. 60, no. 3, pp. 819–830, Feb. 2012, doi: 10.1016/j.actamat.2011.10.043.

[77] T. T. Sasaki, T. Ohkubo, and K. Hono, “Microstructure of NdFeB Sintered Magnets Structure of Grain Boundaries and Interface,” 日本金属学会誌, vol. 81, no. 1, pp. 2–10, 2017.

[78] T. Nakamura *et al.*, “Direct observation of ferromagnetism in grain boundary phase of Nd-Fe-B sintered magnet using soft x-ray magnetic circular dichroism,” *Applied Physics Letters*, vol. 105, no. 20, pp. 202404-1-202404–4, Nov. 2014, doi: 10.1063/1.4902329.

[79] Takeshi Nishiuchi, Teruo Kohashi, Isao Kitagawa, Akira Sugawara, and Hiroyuki Yamamoto, “Influence of Intergranular Grain Boundary Phases on Coercivity in NdFeB based Magnets,” *Hitachi Metals technical review*, vol. 32, pp. 36–43, 2016.

[80] Masaaki Tokunaga, Minoru Endoh, and Hideki Harada, “Nd-Fe-B sintered magnets with Ga addition,” *Journal of the Japan Society of Powder and Powder Metallurgy*, vol. 34, no. 9, pp. 464-undefined, 1987.

[81] W. F. Li, T. Ohkubo, T. Akiya, H. Kato, and K. Hono, “The role of Cu addition in the coercivity ehhancement of sintered Nd-Fe-B permanent magnets,” *Journal of Materials Research*, vol. 24, no. 2, pp. 413–420, 2009.

[82] T. Akiya, H. Kato, M. Sagawa, K. Koyama, and T. Miyazaki, “High-magnetic-field annealing and coercivity in sintered Nd-Dy-Fe-B-Type magnets,” *Journal of the Magnetics Society of Japan*, vol. 30, pp. 447–454, 2006.

[83] M. M. Carnasciali, G. A. Costa, and E. A. Franceschi, “PHASE EQUILIBRIA IN THE Nd-Cu SYSTEM,” *Journal of the Less-Common Metals*, vol. 92, pp. 97–103, 1983.

[84] Margin Leonowicz, “Effect of minor alloying substituents (Ga, Nb, Cr, Zr, Sn, Bi) on magnetic properties of Nd-Fe-B materials,” *Archives of Metallurgy*, vol. 34, no. 1, pp. 85–91, 1989.

[85] X.C. Kou, X. K. Sun, and Y. C. Chuang, “Exchange interaction and magnetic anisotropy in $Nd_2(Fe_{13}M)B$ Compunds (M=Ga, Si, Al),” *Journal of Magnetism and Magnetic Materials*, vol. 82, pp. 327–334, 1989.

[86] Minoru Endoh and Masaaki Tokunaga, “Magnetic properties and thermal stabilityities of Nd-Fe-Co-B and Nd-Dy-Fe-Co-B magnets with Ga added,” 日立金属技報, vol. 4, pp. 19–26, 1988.

[87] R. Nakayama, T. Takeshita, M. Itakura, N. Kuwano, and K. Oki, “Microstructures and crystallographic orientation of crystalline grains in anisotropic Nd-Fe-Co-B-(Ga or Zr) magnet powders produced by the hydrogenation-decomposition-desorption-recombination process,” *Journal of Applied Physics*, vol. 76, no. 1, pp. 412–417, 1994, doi: 10.1063/1.357091.

[88] I. Ahmad, H. A. Davies, and R. A. Buckley, “Ultra high coercivity Nd-Fe-B permanent magnet alloy with small addition of Ga,” *Materials Letters*, vol. 20, pp. 139–142, 1994.

[89] S. Hirosawa, H. Kanekiyo, and M. Uehara, “High-coercivity iron-rich rare-earth permanent magnet material based on $(Fe, Co)_3B$-Nd-M (M=Al, Si, Cu, Ga, Ag, Au),” *Journal of Applied Physics*, vol. 73, no. 10, pp. 6488–6490, 1993, doi: 10.1063/1.352589.

[90] I. Armad, M. A. Al-Khafaji, H. A. Davies, W. M. Rainforth, and R. A. Buckley, “Microstructure study of high coercivity Ga containing Nd-Fe-B permanent magnets,” *Journal of Magnetism and Magnetic Materials*, vol. 145, pp. L19–L22, 1995.

[91] Johannes Bernardi and Josef Fidler, “Preparation and TEM-study of sintered $Nd_{18}Fe_{74}B_6Ga_1Nb_1$ magnets,” *IEEE Transactions on magnetics*, vol. 29, no. 6, pp. 2773–2775, 1993.

[92] A. M. Gabay, Y. Zhang, and G. C. Hadjipanayis, “Effect of very small additions on the coercivity of Dy-free Nd-Fe-(Co)-B-sintered magnets,” *Journal of Magnetism and Magnetic Materials*, vol. 238, pp. 226–232, 2002.

[93] A. Kowalczyk, “Magnetic and Crystallographic Properties of Substituted $Pr_2Fe_{14-x}M_xB$ Compounds (M=Si, Ga, Cr and Cu),” *Journal of Magnetism and Magnetic Materials*, vol. 82, pp. L1–L4, 1989.

[94] H. Kanekiyo, M. Uehara, and S. Hirosawa, “Microstructure and magnetic properties of high-remanence $Nd_5Fe_{71.5}Co_5B_{18.5}M$ (M=Al, Si, Ga, Ag, Au) rapidly solidified and crystallized alloys for resin-bonded magnets,” *IEEE Transactions on Magnetics*, vol. 29, no. 6, pp. 2863–2865, 1993.

[95] Koichiro Inomata, Tetsuhiko Mizoguchi, Akihiko Tsutai, and Isao Sakai, “Nd-Fe-B system magnets with high Curie temperature,” *Journal of the Japan Society of Powder and Powder Metallurgy*, vol. 34, no. 9, pp. 103–107, 1987.

[96] K. G. Knoch, A. le Calvez, Q. Qi, A. Leithe-Jasper, and J. M. D. Coey, “Structure and magnetic properties of Nd6Fe13Cu,” *Journal of Applied Physics*, vol. 73, no. 10, pp. 5878–5880, 1993, doi: 10.1063/1.353508.

[97] K. G. Knoch, B. Grieb, E. -Th. Henig, H. Kronmuller, and G. Petzow, “Upgraded Nd-Fe-B-AD (AD=Al, Ga) magnets: wettability and microstructure,” *IEEE Transactions on Magnetics*, vol. 26, no. 5, pp. 1951–1953, 1990.

[98] M. Seeger and H. Kronmuller, “Magnetic properties and microstructural analysis of rapidly quenched FeNdBGaNb permanent magnets,” *Journal of Magnetism and Magnetic Materials*, vol. 139, pp. 323–334, 1995.

[99] M. Seeger, J. Bauer, H. Kronmuller, J. Bernardi, and J. Fidler, “Magnetic and microstructural properties of sintered FeNdB-based magnets with Ga and Nb additions,” *Journal of Magnetism and Magnetic Materials*, vol. 138, pp. 294–300, 1994.

[100] M. Katter, L. Zapf, R. Blank, and W. Rodewald, “Corrosion Mechanism of RE-Fe-Co-Cu-Ga-Al-B Magnets,” *IEEE Transactions on Magnetics*, vol. 37, no. 4, pp. 2474–2476, 2001.

[101] J. Fidler, C. Groiss, and M. Tokunaga, “The influence of Ga-substitution on the coercivity of Nd-(Fe,Co)-B sintered permanent magnets,” *IEEE Transactions on Magnetics*, vol. 26, no. 5, pp. 1948–1950, 1990.

[102] N. Watanabe, M. Itakura, and M. Nishida, “Microstructure of high coercivity Nd-Fe-Co-Ga-B hot-deformed magnet improved by the Dy diffusion treatment,” *Journal of Alloys and Compounds*, vol. 557, pp. 1–4, Apr. 2013, doi: 10.1016/j.jallcom.2012.12.084.

[103] 山﨑貴司, 須藤翔太朗, 堀北雅揮, 村岡亮史, 中島健一朗, and 長谷川寛, “RE-T-M相を粒界に含む高保磁力NdFeB焼結磁石及び磁石合金の開発とその微細構造,” in 日本金属学会春期講演退会, 2014, vol. S7-21, pp. S7-21-undefined.

[104] P. Schobinger-Papamantellos, C. Ritter, and K. Buschow, “On the magnetic ordering of $Nd_6Fe_{13-x}Al_{1+x}$ (x=1-3) and $La_6Fe_{11}Al_3$ compounds,” *Journal of Magnetism and Magnetic Materials*, vol. 260, pp. 156–172, 2003.

[105] Chikara Ishizaka, Hiroaki Nishio, Eiji Kato, and Akira Fukuno, “Temperature Dependence of Magnetic Domain Structure in Nd-Fe-B Sintered Magnets,” in *Proceedings of the Sixteenth International Workshop on Rare-Earth Magnets and Their Applications*, 2000, pp. 237–246.

[106] 山崎貴志, 村岡亮史, 中島健一朗, and 長谷川寛, “Dyフリー1600超kA/m NdFeB焼結磁石及び合金の開発と量産,” in *Autumn Meeting of the Japan Society of Powder and Powder Metallurgy*, 2013, pp. 79-undefined.

[107] Akihiko Saguchi, Mitsuharu Yonemura, and Kenji Higashi, “Study of Microscopic structure of Ga added neodymium magnet alloy,” *Journal of Japan Society of Powder and Powder Metallurgy*, vol. 61, no. 4, pp. 186–192, 2014.

[108] Y. Enokido, M. Miwa, S. Goto, and Y. Fujikawa, "Effects of grain boundary phase on coercivity of dysprosium-free rare earth magnet," *Materials Transactions*, vol. 57, no. 11, pp. 1960–1965, 2016, doi: 10.2320/matertrans.M2016160.

[109] Y. Enokido, Y. Nagamine, M. Miwa, Y. Fujikawa, C. Moriyoshi, and Y. Kuroiwa, "Heavy rare-earth-free Neodymium magnets for automobiles," in *REPM 2016, Darmstadt, Germany*, 2016, pp. 75–79.

[110] K. Niitsu *et al.*, "Magnetization measurements for grain boundary phases in Ga-doped Nd-Fe-B sintered magnet," *Journal of Alloys and Compounds*, vol. 752, pp. 220–230, Jul. 2018, doi: 10.1016/j.jallcom.2018.04.055.

[111] E. J. Skoug, M. S. Meyer, F. E. Pinkerton, M. M. Tessema, D. Haddad, and J. F. Herbst, "Crystal structure and magnetic properties of $Ce_2Fe_{14-x}Co_xB$ alloys," *Journal of Alloys and Compounds*, vol. 574, pp. 552–555, 2013, doi: 10.1016/j.jallcom.2013.05.101.

[112] Z. Li *et al.*, "Effects of CE substitution on the microstructures and intrinsic magnetic properties of Nd-Fe-B alloy," *Journal of Magnetism and Magnetic Materials*, vol. 393, pp. 551–554, Jun. 2015, doi: 10.1016/j.jmmm.2015.06.028.

[113] C. Yan, S. Guo, R. Chen, D. Lee, and A. Yan, "Enhanced magnetic properties of sintered Ce-Fe-B-based magnets by optimizing the microstructure of strip-casting alloys," *IEEE Transactions on Magnetics*, vol. 50, no. 11, Nov. 2014, doi: 10.1109/TMAG.2014.2325404.

[114] L. Z. Zhao *et al.*, "Phase and Hyperfine Structures of Melt-spun Nanocrystalline $(Ce_{1-x}Nd_x)_{16}Fe_{78}B_6$ Alloys," *IEEE Transactions on Magnetics*, vol. 53, no. 11, Nov. 2017, doi: 10.1109/TMAG.2017.2695533.

[115] X. Yu, M. Yue, W. Liu, Z. Li, M. Zhu, and S. Dong, "Structure and intrinsic magnetic properties of $MM_2Fe_{14}B$ (MM=La, Ce, Pr, Nd) alloys," *Journal of Rare Earths*, vol. 34, no. 6, pp. 614–617, Jun. 2016, doi: 10.1016/S1002-0721(16)60069-8.

[116] C. D. Fuerst, T. W. Capehart, F. E. Pinkerton, and J. F. Herbst, "Preparation and characterization of $La_{2-x}Ce_xFe_{14}B$ compounds," *Journal of magnetism magnetic materials* , vol. 139, pp. 359–363, 1995.

[117] A. Alam, M. Khan, R. W. McCallum, and D. D. Johnson, "Site-preference and valency for rare-earth sites in $(R\text{-}Ce)_2Fe_{14}B$ magnets," *Applied Physics Letters*, vol. 102, pp. 042402-1-042402–4, Jan. 2013, doi: 10.1063/1.4789527.

[118] C. Yan, S. Guo, R. Chen, D. Lee, and A. Yan, "Effect of Ce on the Magnetic Properties and Microstructure of Sintered Didymium-Fe-B Magnets," *IEEE Transactions on Magnetics*, vol. 50, no. 10, Oct. 2014, doi: 10.1109/TMAG.2014.2322823.

[119] E. Niu *et al.*, "Achievement of high coercivity in sintered R-Fe-B magnets based on misch-metal by dual alloy method," *Journal of Applied Physics*, vol. 115, no. 11, Mar. 2014, doi: 10.1063/1.4869202.

[120] A. Alam and D. D. Johnson, "Mixed valency and site-preference chemistry for cerium and its compounds: A predictive density-functional theory study," *Physical Review B - Condensed Matter and Materials Physics*, vol. 89, no. 23, Jun. 2014, doi: 10.1103/PhysRevB.89.235126.

[121] J. Jin, Y. Zhang, T. Ma, and M. Yan, "Mechanical Properties of La-Ce-Substituted Nd-Fe-B Magnets," *IEEE Transactions on Magnetics*, vol. 52, no. 7, Jul. 2016, doi: 10.1109/TMAG.2016.2524019.

[122] J. Jin *et al.*, "Manipulating Ce Valence in $RE_2Fe_{14}B$ Tetragonal Compounds by La-Ce Co-doping: Resultant Crystallographic and Magnetic Anomaly," *Scientific Reports*, vol. 6, Jul. 2016, doi: 10.1038/srep30194.

[123] K. Pei, X. Zhang, M. Lin, and A. Yan, "Effects of Ce-substitution on magnetic properties and microstructure of Nd-Pr-Fe-B melt-spun powders," *Journal of Magnetism and Magnetic Materials*, vol. 398. Elsevier B.V., pp. 96–100, Jan. 15, 2016, doi: 10.1016/j.jmmm.2015.09.027.

[124] A. K. Pathak, K. A. Gschneidner, M. Khan, R. W. McCallum, and V. K. Pecharsky, "High performance Nd-Fe-B permanent magnets without critical elements," *Journal of Alloys and Compounds*, vol. 668, pp. 80–86, May 2016, doi: 10.1016/j.jallcom.2016.01.194.

[125] J. F. Herbst, M. S. Meyer, and F. E. Pinkerton, "Magnetic hardening of $Ce_2Fe_{14}B$," in *Journal of Applied Physics*, Apr. 2012, vol. 111, no. 7, doi: 10.1063/1.3675175.

[126] A. K. Pathak *et al.*, "Magnetic properties of bulk, and rapidly solidified nanostructured $(Nd_{1-x}Ce_x)_2Fe_{14-y}CoyB$ ribbons," *Acta Materialia*, vol. 103, pp. 211–216, Jan. 2016, doi: 10.1016/j.actamat.2015.09.049.

[127] Z. Chen, Y. K. Lim, and D. Brown, "Substitution of Ce for (Nd,Pr) in Melt-Spun (Nd,Pr)-Fe-B Powders," *IEEE Transactions on Magnetics*, vol. 51, no. 11, Nov. 2015, doi: 10.1109/TMAG.2015.2437376.

[128] Z. B. Li, M. Zhang, B. G. Shen, F. X. Hu, and J. R. Sun, "Variations of phase constitution and magnetic properties with Ce content in Ce-Fe-B permanent magnets," *Materials Letters*, vol. 172, pp. 102–104, Jun. 2016, doi: 10.1016/j.matlet.2016.02.149.

[129] H. Ren *et al.*, "Magnetic hardening of Nd-Ce-Fe-B films with high Ce concentration," *Scientific Reports*, vol. 8, no. 1, Dec. 2018, doi: 10.1038/s41598-018-29907-4.

[130] B. Chen *et al.*, "Coercivity enhancement of hot-deformed (Ce,Nd,Pr)-Fe-B magnets by grain boundary diffusion of Pr-Cu alloy," *Journal of Magnetism and Magnetic Materials*, vol. 497, Mar. 2020, doi: 10.1016/j.jmmm.2019.166002.

[131] X. Tang *et al.*, "Coercivity enhancement of hot-deformed Ce-Fe-B magnets by grain boundary infiltration of Nd-Cu eutectic alloy," *Acta Materialia*, vol. 144, pp. 884–895, Feb. 2018, doi: 10.1016/j.actamat.2017.10.071.

[132] X. Tang *et al.*, "Coercivity enhancement of hot-deformed Ce-Fe-B magnets by grain boundary infiltration of Nd-Cu eutectic alloy," *Acta Materialia*, vol. 144, pp. 884–895, Feb. 2018, doi: 10.1016/j.actamat.2017.10.071.

[133] I. Poenaru *et al.*, "Ce and La as substitutes for Nd in $Nd_2Fe_{14}B$-based melt-spun alloys and hot-deformed magnets: a comparison of structural and magnetic properties," *Journal of Magnetism and Magnetic Materials*, vol. 478, pp. 198–205, May 2019, doi: 10.1016/j.jmmm.2019.01.095.

[134] D. Hinz, A. Kirchner, D. N. Brown, B.-M. Ma, and O. Gutfleisch, "Near net shape production of radially oriented NdFeB ring magnets by backward extrusion," *Journal of Materials Processing Technology*, vol. 135, pp. 358–365, 2003.

[135] Y. Zhang *et al.*, "Effects of $REFe_2$ on microstructure and magnetic properties of Nd-Ce-Fe-B sintered magnets," *Acta Materialia*, vol. 128, pp. 22–30, Apr. 2017, doi: 10.1016/j.actamat.2017.02.002.

[136] A. Li, Y. Zhang, W. Li, H. Feng, Y. Zhao, and M. Zhu, "Influence of Ce Content on the Mechanical Properties of Sintered (Ce, Nd)-Fe-B Magnets," *IEEE Transactions on Magnetics*, vol. 53, no. 11, Nov. 2017, doi: 10.1109/TMAG.2017.2706750.

[137] W. Li, A. Li, H. Feng, S. Huang, J. Wang, and M. Zhu, "The Study on Grain-Boundary Microstructure of Sintered (Ce, Nd)-Fe-B Magnets," *IEEE Transactions on Magnetics*, vol. 51, no. 11, Nov. 2015, doi: 10.1109/TMAG.2015.2440476.

[138] H. Feng, Y. Zhang, A. Li, Y. Zhao, and W. Li, "Microstructure and Magnetic Properties of Recycled Nd-Fe-B Magnets with Blending of Ce-Rich Alloy," *IEEE Transactions on Magnetics*, vol. 53, no. 11, Nov. 2017, doi: 10.1109/TMAG.2017.2704091.

[139] K. CHEN *et al.*, "Coercivity enhancement of Ce-Fe-B sintered magnets by low-melting point intergranular additive," *Journal of Rare Earths*, vol. 35, no. 2, pp. 158–163, Feb. 2017, doi: 10.1016/S1002-0721(17)60894-9.

[140] X. Fan *et al.*, "Core-shell Y-substituted Nd-Ce-Fe-B sintered magnets with enhanced coercivity and good thermal stability," *Applied Physics Letters*, vol. 110, pp. 172405-1-172405–4, Apr. 2017, doi: 10.1063/1.4982679.

[141] X. Fan *et al.*, "Tuning Ce distribution for high performanced Nd-Ce-Fe-B sintered magnets," *Journal of Magnetism and Magnetic Materials*, vol. 419, pp. 394–399, Dec. 2016, doi: 10.1016/j.jmmm.2016.06.048.

[142] Y. Zhang *et al.*, "Squareness factors of demagnetization curves for multi-main-phase Nd-Ce-Fe-B magnets with different Ce contents," *Journal of Magnetism and Magnetic Materials*, vol. 487, Oct. 2019, doi: 10.1016/j.jmmm.2019.165355.

[143] M. Hussain, L. Z. Zhao, C. Zhang, D. L. Jiao, X. C. Zhong, and Z. W. Liu, "Composition-dependent magnetic properties of melt-spun la or/and Ce substituted nanocomposite NdFeB alloys," *Physica B: Condensed Matter*, vol. 483, pp. 69–74, Feb. 2016, doi: 10.1016/j.physb.2015.12.033.

[144] J. Jin *et al.*, "Crucial role of the $REFe_2$ intergranular phase on corrosion resistance of Nd-La-Ce-Fe-B sintered magnets," *Journal of Alloys and Compounds*, vol. 735, pp. 2225–2235, Feb. 2018, doi: 10.1016/j.jallcom.2017.11.372.

[145] R. K. Chouhan, A. K. Pathak, D. Paudyal, and V. K. Pecharsky, "High performance magnetic material with Ce and La: an alternative to Nd-Fe-B magnet," *arXiv*, vol. 1806.01990, 2018.

[146] R. Li *et al.*, "Magnetic properties of (misch metal, Nd)-Fe-B melt-spun magnets," *AIP Advances*, vol. 7, no. 5, May 2017, doi: 10.1063/1.4973846.

[147] J. Jin, Z. Wang, G. Bai, B. Peng, Y. Liu, and M. Yan, "Microstructure and magnetic properties of core-shell Nd-La-Fe-B sintered magnets," *Journal of Alloys and Compounds*, vol. 749, pp. 580–585, Jun. 2018, doi: 10.1016/j.jallcom.2018.03.291.

[148] Q. Zhou, R. Tang, F. Xiao, and Z. Liu, "Coercivity enhancement of Nd-Ce-Fe-B sintered magnets by the grain boundary diffusion process using Nd-Al-Cu alloy," *IEEE Transactions on Magnetics*, vol. 54, no. 11, Nov. 2018, doi: 10.1109/TMAG.2018.2835841.

[149] B. Peng, T. Ma, Y. Zhang, J. Jin, and M. Yan, "Improved thermal stability of Nd-Ce-Fe-B sintered magnets by Y substitution," *Scripta Materialia*, vol. 131, pp. 11–14, Apr. 2017, doi: 10.1016/j.scriptamat.2016.12.013.

[150] Takahiko Akiya, Keiko Hioki, Atsushi Hattori, Tadakatsu Ohkubo, and Kazuhiro Hono, "Expansion phenomena by infiltration of low eutectic temperature alloy in hot deformed NdFeB magnets," 電機製鋼, vol. 86, no. 2, pp. 93–100, 2016.

[151] M. Tang *et al.*, "Microstructure modification and coercivity enhancement of Nd-Ce-Fe-B sintered magnets by grain boundary diffusing Nd-Dy-Al alloy," *Journal of Magnetism and Magnetic Materials*, vol. 442, pp. 338–342, Nov. 2017, doi: 10.1016/j.jmmm.2017.06.116.

[152] H. J. Park, M. S. Lim, and C. S. Lee, "Magnet shape design and verification for SPMSM of EPS system using cycloid curve," *IEEE Access*, vol. 7, pp. 137207–137216, 2019, doi: 10.1109/ACCESS.2019.2942038.

[153] Hidetoshi Kotera, Fujio Tsumori, Ikkou Iritani, Tomoharu Watanabe, and Susumu Shima, "Improving NdFeB magnet fabrication In situ observation of powder flow," *International Journal of Powder Metallurgy*, vol. 40, no. 1, pp. 33–40, 2004.

[154] E. R. Rice and J. Tengzelius, "Die filling characteristics of metal powders," *Powder Metallurgy*, vol. 29, no. 3, pp. 183–194, Jan. 1986, doi: 10.1179/pom.1986.29.3.183.

[155] N. W. Page, M. Yousuff, and C. J. Wauchope, "Interparticle Friction in Granular Ceramic Materials," *KONA Powder and Particle Journal*, vol. 11, pp. 147–155, 1993.

[156] H. C. Hamaker, "The London-Van Der Waals attraction between spherical particles," *Physica IV*, vol. 10, pp. 1058–1072, 1937.

[157] Hiroaki Masuda, "Adhesion of Powder ParticIes," 電子写真学会誌, vol. 36, no. 3, pp. 169–174, 1997.

[158] D. Brown, B.-M. Ma, and Z. Chen, "Topical review Developments in the processing and properties of NdFeb-type permanent magnets," 2002.

[159] M. Takahashi, K. Uchida, F. Taniguchi, and T. Mikamoto, "High performance Nd-Fe-B sintered magnets made by the wet process," *Journal of Applied Physics*, vol. 83, no. 11, pp. 6402–6404, 1998, doi: 10.1063/1.367524.

[160] H. Tokoro and K. Uchida, "High Energy Product Nd-Fe-B Sintered Magnets Produced by Wet Compacting Process," 2001.

[161] L. Ulian Lopes, T. Hartwig, and P. A. P. Wendhausen, "Evaluation of process variables in the alignment factor of Nd-Fe-B magnets made by metal injection molding," *IEEE Transactions on Magnetics*, vol. 49, no. 8, pp. 4618–4621, 2013, doi: 10.1109/TMAG.2013.2259802.

[162] T. Hartwig, L. Lopes, P. Wendhausen, and N. Ünal, "Metal Injection Molding (MIM) of NdFeB Magnets; Metal Injection Molding (MIM) of NdFeB Magnets," 2013, doi: 10.1051/C.

[163] L. U. Lopes, M. A. Carvalho, R. S. Chaves, M. P. Trevisan, P. A. P. Wendhausen, and H. Takiishi, "Study of carbon influence on magnetic properties of metal injection molding Nd-Fe-B based magnets," in *Materials Science Forum*, 2012, vol. 727–728, pp. 124–129, doi: 10.4028/www.scientific.net/MSF.727-728.124.

[164] Nkkolaus Urban, Alexander Kuhl, Markus Glauche, and Jorg Franke, "Additive manufacturing of neodymium iron boron permanent magnet," *2018 8th International Electric Drives Production Conference (EDPC)*, 2018.

[165] L. Li, B. Post, V. Kunc, A. M. Elliott, and M. P. Paranthaman, "Additive manufacturing of near-net-shape bonded magnets: Prospects and challenges," *Scripta Materialia*, vol. 135, pp. 100–104, Jul. 2017, doi: 10.1016/j.scriptamat.2016.12.035.

[166] L. Li *et al.*, "Fabrication of highly dense isotropic Nd-Fe-B nylon bonded magnets via extrusion-based additive manufacturing," *Additive Manufacturing*, vol. 21, pp. 495–500, May 2018, doi: 10.1016/j.addma.2018.04.001.

[167] M. P. Paranthaman *et al.*, "Binder Jetting: A Novel NdFeB Bonded Magnet Fabrication Process," *The Journal of The Minerals, Metals & Materials Society*, vol. 68, no. 7, pp. 1978–1982, Jul. 2016, doi: 10.1007/s11837-016-1883-4.

[168] Yoshihisa Kishimoto, Masami Ueda, and Osamu Yamashita, "Magnetic Properties of Sendust Alloys Sintered Using Granulated Powders by Spray Drying Method (1)," *Journal of the Japan Society of Powder and Powder Metallurgy*, vol. 45, no. 11, pp. 1036–1041, 1998.

[169] Masami Ueda, Osamu Yamashita, Yoshihisa Kishimoto, and Ken Makita, "Magnetic Properties of Sendust Alloys Sintered Using Granulated Powders by Spray Drying Method (2)," *Journal of the Japan Society of Powder and Powder Metallurgy*, vol. 46, no. 4, pp. 653–658, 1999.

[170] O. Yamashita and Y. Kishimoto, "Magnetic Properties of Nd-Fe-B Magnets Sintered Using Granulated Powders by Spray Drying Method," *Journal of the Japan Society of Powder and Powder Metallurgy*, vol. 43, no. 2, pp. 249–255, 1996.

[171] Y. Kishimoto and O. Yamashita, "Magnetic Properties of Nd-Fe-B Magnets Sintered Using Granulated Powders by Spray Drying Method (III)," *Journal of the Japan Society of Powder and Powder Metallurgy*, vol. 44, no. 8, pp. 775–780, 1997.

[172] Y. Kishimoto and O. Yamashita, "Magnetic Properties of Nd-Fe-B Magnets Sintered Using Granulated Powders by Spray Drying Method (IV)," *Journal of the Japan Society of Powder and Powder Metallurgy*, vol. 44, no. 10, pp. 951–957, 1997.

[173] O. Yamashita and Y. Kishimoto, "Magnetic Properties of Nd-Fe-B Magnets Sintered Using Granulated Powders by Spray Drying Method (II)," *Journal of the Japan Society of Powder and Powder Metallurgy*, vol. 43, no. 5, pp. 675–681, 1996.

[174] Yoshihisa Kishimoto and Osamu Yamashita, "Magnetic Properties of NdFeB Magnets Sintered Using Spray Dried Powders with Nonaqueous Binder," *Journal of the Japan Society of Powder and Powder Metallurgy*, vol. 45, no. 4, pp. 373–378, 1998.

[175] Ken Makita, Osamu Yamashita, and Tetsuya Senda, "Thermal Decomposition Behavior of PVA as Organic Binder of Spray Dried NdFeB System Powder," *Journal of the Japan Society of Powder and Powder Metallurgy*, vol. 457, pp. 646–651, 1998.

[176] B. Science, S. J. Lloyd, J. C. Loudon, and P. A. Midgley, "Measurement of magnetic domain wall width using energy-filtered Fresnel images," *Journal of Microscopy*, vol. 207, pp. 118–128, 2002.

[177] Young-Gil Park, Daisuke Shindo, and Masuo Okada, "Magnetic domain structures of NdFeB based permanent magnets studied by electron holography and lorentz microscopy," *Matetrials Transactions, JIM*, vol. 41, no. 9, pp. 1132–1135, 2000.

[178] C. Yang, W. Lee, S. Choi, and Y. Jeong, "Phase transition and magnetic properties of rapidly solidified Nd-Fe alloys," *Materials Letters*, vol. 12, pp. 233–241, 1991.

[179] C.-J. Yang, W.-Y. Lee, and S.-D. Choi, "Magnetic phase transition in rapidly solidified Nd-Fe alloy," *Journal of Magnetism and Magnetic Materials*, vol. 114, pp. 18–26, 1992.

[180] Katarzyna Pawlik, Jerzy J. Wystocki, Jacek Olszewski, Oksana I. Bodak, and Piotr Pawlik, “Phase composition investigations of the Nd-Fe alloys processed by various methods,” *NUKLEONIKA*, vol. 49, pp. S27–S31, 2004.

[181] Yoshitomo Tanaka, Tadakatsu Ohkubo, and Kazuhiro Hono, “STEM Lorentz法による磁気構造解析手法の開発,” in 日本金属学会春期講演退会, 2015, pp. S1-27-undefined.

[182] Toshiro Suenaga, “Combinatorial Chemistry,” *Journal of the Mass Spectrometry Society of Japan*, vol. 45, no. 3, pp. 265–288, 1997.

[183] X. Xiang *et al.*, “Physicists make tiny fingers for tiny jobs,” *Science*, vol. 268, pp. 1738–1740, 1995.

[184] Nobuyuki Okajima, “創薬におけるコンビナトリアルケミストリーの利用,” 日本農業学会誌, vol. 28, pp. 86–93, 2003.

[185] A. D. Collord, H. Xin, and H. W. Hillhouse, “Combinatorial exploration of the effects of intrinsic and extrinsic defects in $Cu_2ZnSn(S,Se)_4$,” *IEEE Journal of Photovoltaics*, vol. 5, no. 1, pp. 288–298, Jan. 2015, doi: 10.1109/JPHOTOV.2014.2361053.

[186] K. S. Chang, M. L. Green, P. K. Schenck, I. Levin, and E. Venkatasubramanian, “High-Throughput Screening of Amorphous Y_2O_3-TiO_2/SiO_2 Higher κ Gate Dielectric Layers,” *IEEE Transactions on Electron Devices*, vol. 59, no. 12, pp. 3212–3216, 2012, doi: 10.1109/TED.2012.2216533.

[187] T. Takahashi, A. Abdulkadhim, D. Music, and J. M. Schneider, “Spontaneous formation of in-whiskers on YIn_3 thin films deposited by combinatorial magnetron sputtering,” *IEEE Transactions on Nanotechnology*, vol. 10, no. 5, pp. 1202–1208, Sep. 2011, doi: 10.1109/TNANO.2011.2129527.

[188] H. Koinuma, H. N. Aiyer, and Y. Matsumoto, “Combinatorial solid state materials science and technology,” *Science and Technology of Advanced Materials*, vol. 1, no. 1, pp. 1–10, Mar. 2000, doi: 10.1016/S1468-6996(00)00003-6.

[189] Y. Iwasaki, A. G. Kusne, and I. Takeuchi, “Comparison of dissimilarity measures for cluster analysis of X-ray diffraction data from combinatorial libraries,” *npj Computational Materials*, vol. 3, no. 1, Dec. 2017, doi: 10.1038/s41524-017-0006-2.

[190] T. Chikamatsu, A. Ogawa, and T. Mizuno, “nano-MDS ; Magnetic Domain Scope for wide area with nano order resolution,” *Magnetics Japan*, vol. 6, no. 6, pp. 357-undefined, 2011.

[191] K. Akahane, T. Kimura, and Y. Otani, “Development of High Sensitive Micro-Kerr Magnetometer,” *Journal of Magnetics Society of Japan*, vol. 28, pp. 122–127, 2004.

[192] P. E. Blochl, “Projector augmented-wave method,” *PHYSICAL REVIEW B VOLUME*, vol. 50, no. 24, pp. 17953–17979, 1994.

[193] G. Kresse and J. Furthmü, “Efficient iterative schemes for ab initio total-energy calculations using a plane-wave basis set,” 1996.

[194] J. P. Perdew, K. Burke, and M. Ernzerhof, “Generalized Gradient Approximation Made Simple,” *Physical Review Letters*, vol. 77, no. 18, pp. 3865–3868, 1996.

[195] R. Hashimoto, K. Suzuki, Y. Enokido, and K.-K. Choi, “Magnetic properties of (Nd,Y)-Fe-B layered thin film magnets,” in 第*40*回 日本磁気学会学術講演概要集, 2016, pp. 6aD-11-undefined.

[196] R. Hashimoto *et al.*, “Effect of Strain on Magnetic Properties of Nd-Fe-B Thin Film Magnets on $BaTiO_3$,” *J. Jpn. Soc. Powder Powder Metallurgy*, vol. 65, no. 5, pp. 265–268, 2018.

[197] A. K. Pathak *et al.*, “Cerium: An unlikely replacement of dysprosium in high performance Nd-Fe-B permanent magnets,” *Advanced Materials*, vol. 27, no. 16, pp. 2663–2667, Apr. 2015, doi: 10.1002/adma.201404892.

[198] Changjiang Yan, Shuai Guo, Renjie Chen, Don. Lee, and Aru Yan, “Fabrication and microstructural analysis of sintered Didymium-Fe-B magnet with various Ce additions,” in *2014 International Conferences on NdFeB Magnets: Supply Chain, Critical Properties, & Applications*, 2014, pp. 86–91.

[199] K H J Buschow, “Intermetallic compounds of rare-earth and 3d transition metals,” *Reports on Progress in Physics*, vol. 40, pp. 1179–1256, 1977.

[200] C C Tang *et al.*, “The effect of substitution by cerium on the structure and magnetic properties of the compound NdFe2,” *Journal of Physics D: Applied Physics*, vol. 31, pp. 2426–2430, 1998.

[201] X. B. Liu, Z. Altounian, M. Huang, Q. Zhang, and J. P. Liu, “The partitioning of la and y in Nd-Fe-B magnets: A first-principles study,” *Journal of Alloys and Compounds*, vol. 549, pp. 366–369, Feb. 2013, doi: 10.1016/j.jallcom.2012.10.056.

[202] Y. Enokido, R. Hashimoto, T. Kitamura, K. Suzuki, K. K. Choi, and Y. Kitamoto, “High-Throughput Screening Method for Thin-Film $R_2Fe_{14}B$ Magnet,” *IEEE Transactions on Magnetics*, vol. 56, no. 4, Apr. 2020, doi: 10.1109/TMAG.2019.2962015.

[203] Y. Enokido, A. Koda, Y. Umeda, D. Tanaka, and Y. Kitamoto, “Effect of grain-boundary phases in Y- and Ce-substituted $R_2Fe_{14}B$ sintered magnets,” *Journal of Magnetism and Magnetic Materials*, vol. 517, pp. 1–6, Jan. 2021, doi: 10.1016/j.jmmm.2020.167406.

[204] L. Z. Zhao, J. S. Zhang, G. Ahmed, X. F. Liao, Z. W. Liu, and J. M. Greneche, “Understanding the element segregation and phase separation in the Ce-substituted Nd-(Fe,Co)-B based alloys,” *Scientific Reports*, vol. 8, no. 1, pp. 1–8, Dec. 2018, doi: 10.1038/s41598-018-25230-0.

[205] Takuro Nakamichi, “Laves相化合物の磁性,” 日本金属学会会報, vol. 2, pp. 63–72, 1968, doi: https://doi.org/10.2320/materia1962.7.63.

[206] Tanabe Teruo, Kubota Takeshi, and Asaki Zenjiro, “Formation Kinetics of Light Rare Earth (Ce, Sm)-Fe Intermetallic Compounds,” 資源と素材, vol. 110, pp. 137–142, 1994.

[207] X. Zhang and N. Ali, “Effects of Co and Y substitution on magnetic properties of $CeFe_2$,” *Journal of Applied Physics*, vol. 75, no. 10, pp. 7128–7130, 1994, doi: 10.1063/1.356700.

[208] S. B. Roy and B. R. Coles, “Magnetic behavior of $CeFe_2$: Effects of ruthenium substitution,” *Journal of Applied Physics*, vol. 63, no. 8, pp. 4094–4095, 1988, doi: 10.1063/1.340560.

[209] K. Buschow, R. van Stapele, J. Buschow’, and R. P. van Stapele, “Magnetic properties of the intermetallic compounds RFe_2,” *Journal de Physique Colloques*, vol. 32, no. C1, 1971, doi: 10.1051/jphyscol:19711234ï.

[210] S B Roy and B R Coles, “On the instability of ferromagnetism in $CeFe_2$: effects of alloying with Al, Mn, Y and U,” *Journal of Physics*, vol. Condensed Matter 1, pp. 419–430, 1989.

[211] L. Z. Zhao *et al.*, “Structure, magnetic properties and Mössbauer study of melt-spun nanocrystalline Ce-rich ternary Ce-Fe-B alloy,” *Journal of Alloys and Compounds*, vol. 715, pp. 60–64, 2017, doi: 10.1016/j.jallcom.2017.04.320.

[212] H. Kotera, W. Kitahara, A. Onoyama, and S. Shima, “Behaviour of Magnetic Particles in Compaction,” *IEEE Transactions on Magnetics*, vol. 3, no. 2, 1997.

[213] W. J. Walker, J. S. Reed, and S. K. Verma, “Influence of Slurry Parameters on the Characteristics of Spray-Dried Granules,” *Journal of American Ceramic Society*, vol. 82, no. 7, pp. 1711–1719, 1999.

[214] CARR and R. L., “Evaluating Flow Properties of Solids,” *Chem. Eng.*, vol. 18, pp. 163–168, 1965, Accessed: Nov. 14, 2020. [Online]. Available: http://ci.nii.ac.jp/naid/10026547688/ja/.

[215] T. Minowa, M. Sbimao, and M. Honshima, “Microstructure of Nd-rich phase in Nd-Fe-B magnet containing oxygen and carbon impurities,” 1991.

[216] Hiroaki Masuda, Hideto Yoshida, and Koichi Iinoya, “Statistical analysis of Carr’s Flowability Index,” 粉体工学研究会誌, vol. 12, no. 4, pp. 13–20, 1975.

[217] S. Matsusaka, “Measurements of Powder Flowability,” *The imaging Society of Japan*, vol. 46, pp. 472–477, 2007.

[218] Y. Sun, R. W. Gao, G. B. Han, G. Bai, T. Liu, and B. Wang, “Effects of powder flowability on the alignment degree and magnetic properties for NdFeB sintermagnets,” *Journal of Magnetism and Magnetic Materials*, vol. 299, no. 1, pp. 82–86, Apr. 2006, doi: 10.1016/j.jmmm.2005.03.086.

[219] Guoping Lian, Colin Thornton, and Michael J. Adams, “A Theoretical Study of the Liquid Bridge Forces between Two Rigid Spherical Bodies,” *Journal of Colloid and Interface Science*, vol. 161, pp. 138–147, 1993.

[220] Y. I. Rabinovich, M. S. Esayanur, and B. M. Moudgil, “Capillary forces between two spheres with a fixed volume liquid bridge: Theory and experiment,” *Langmuir*, vol. 21, no. 24, pp. 10992–10997, Nov. 2005, doi: 10.1021/la0517639.

[221] Yoshiyuki Endo, Yasuo Kousaka, and Yasunobu Nishie, “Analysis of adhesion force arising from a liquid bridge formed between two particles,” 化学工学論文集, vol. 19, no. 1, pp. 55–61, 1993.

[222] Yoshiyuki Endo, Yasuo Kousaka, and Mayumi Ishii, “Analysis of liquid bridge formation and adhesion force between two particles of different sizes,” 化学工学論文集, vol. 19, no. 6, pp. 1128-undefined, 1993.

[223] C. E. Capes, R. J. Germain, and R. D. Coleman, “Binding Liquid Requirements for Agglomeration by Tumbling,” *Industrial & Engineering Chemistry Process Design and Development*, vol. 16, no. 4, pp. 517–518, 1977, [Online]. Available: https://pubs.acs.org/sharingguidelines.

[224] A. Goldszal and J. Bousquet, “Wet agglomeration of powders: from physics toward process optimization,” 2001. [Online]. Available: www.elsevier.comrlocaterpowtec.

[225] Norio Ouchiyama and Tatsuo Tanaka, “Kinetic approach to granulation mechanism,” 粉体工学研究会誌, vol. 14, no. 6, pp. 342–345, 1977.

[226] Nagayoshi Myo, “Mechanism of Particle Growth on Granulation and Coating Process,” *Journal of the Japan Society of Colour Material*, vol. 78, no. 1, pp. 17–22, 2005.

[227] Masaaki Matsuda and Masaru Kamoda, “Preparation of Spherical Poly(vinyl chloride) by Tumbling Granulation,” 日本化学会誌, vol. 11, pp. 1308–1314, 1990.

[228] W. A. Beverloo, H. A. Leniger, and J. van de Velde, “The flow of granular solids through orifices,” *Chemical Engineering Science*, vol. 15, pp. 260–269, 1961.

[229] A. Choudhary, P. Ramavath, P. Biswas, N. Ravi, and R. Johnson, “Experimental Investigation on Flowability and Compaction Behavior of Spray Granulated Submicron Alumina Granules,” *ISRN Ceramics*, vol. 2013, pp. 1–6, 2013, doi: 10.1155/2013/264194.

[230] F. C. Franklin and L. N. Johanson, “Flow of granular material through a circular orifice,” *Chemical Engineering Scinence*, vol. 4, pp. 119–129, 1955.

[231] P. Ramavath, M. Swathi, M. Buchi Suresh, and R. Johnson, “Flow properties of spray dried alumina granules using powder flow analysis technique,” *Advanced Powder Technology*, vol. 24, no. 3, pp. 667–673, May 2013, doi: 10.1016/j.apt.2012.12.006.

[232] Norio Ouchiyama and Tatsuo Tanaka, “Mathematical model in the kinetics of granulation,” *Industrial & Engineering Chemistry Process Design and Development*, vol. 13, no. 4, pp. 383–389, 1974, [Online]. Available: https://pubs.acs.org/sharingguidelines.

[233] F. M. Orr, L. E. Scriven, and A. P. Rivas, “Pendular rings between solids: Meniscus properties and capillary force,” *Journal of Fluid Mechanics*, vol. 67, no. 4, pp. 723–742, Feb. 1975, doi: 10.1017/S0022112075000572.

Appendix

Reference values for numerical targets of coercivity

Regarding the reduction of the amount of rare earths, the basic numerical concept was as follows. According to the results of the "Rare Metal Substitute Materials Development Project" released in 2010[3] by the New Energy and Industrial Technology Development Organization (NEDO), a coercivity of 800 kA/m is assumed for magnets that do not contain Dy, and a coercivity of 2400 kA/m is assumed for magnets that contain 10 wt% of Dy. Coercivity of about 2400 kA/m is assumed for main motor and generator for EV/HEV applications [214]. In other words, if a coercivity of 1600 kA/m is achieved without using heavy rare earth elements, it is equivalent to reducing rare earth elements by 50% in these magnets. Due to the evolution of motor design including cooling system, EVs/HEVs often use magnets with lower coercivity such as less than 1990 kA/m nowadays, but targets were set based on the above values. Similarly, when Nd and Pr are reduced by half and a coercivity of 800 kA/m is obtained without using heavy rare earth elements such as Dy and Tb, it is equivalent to reducing Nd and Pr by 50% from a Nd-Fe-B magnet. These magnets cannot be used in the main motors and generators of electrified vehicles due to their low coercivity, but can be used in a variety of other automotive auxiliary motors.

[3] https://www.nedo.go.jp/news/press/ZZ_0515A.html

Unit conversions for magnetic properties

This paper is basically described using the SI system of units. Since the magnet industry has traditionally preferred the CGS system of units, the CGS system of units is sometimes used together in this paper. See below for conversion.

Table. Unit conversion for magnetic properties

	SI unit	cgs unit
Magnetic flux density	1 T	10 kG
	0.1 T	1 kG
Magnetic field	1 kA/m	12.57 Oe
	79.577 kA/m	1 kOe
Maximum energy product	1 MJ/m3	125.66 MGOe
	7.96 kJ/m3	1 MGOe

Acknowledgement

I would like to extend my sincerest gratitude to my supervisor, Professor Yoshitaka Kitamoto who has been encouraging me with inspiration, excellent guidance and continuous supports for whole of my study.

I wish to acknowledge the examination of the doctoral degree with a deep gratitude to Professor Hideki Hosoda, Professor Takumi Sannomiya, Professor Masato Sone, Professor Tadahiko Shinshi, and Professor Satoshi Sugimoto of Tohoku University. Discussions with professors helped me to re-examine my research and rebuild its value.

I would like to highly appreciate to all members of Kitamoto laboratory for their kind helps during my days at Tokyo Institute of Technology. I am very indebted for their active cooperation and warmest support.

I am deeply grateful to my colleagues, members of magnet materials development section in Materials Development Center of TDK Corporation. This research would not have been possible without my time with them.

I am grateful to Dr. Choi Kyung-Ku and Dr. Dai Matsuoka. Without Dr. Choi's words, I would have given up trying to get a Ph.D. and could not continue without Dr. Matsuoka's support.

At last, I wish to express my thanks especially to my wife Megumi and daughter Aoi in all aspects of my student life.

Accomplishments

Journal Publications

- Y. Enokido, M. Miwa, S. Goto, and Y. Fujikawa, “Effects of grain boundary phase on coercivity of dysprosium-free rare earth magnet,” *Materials Transactions*, vol. 57, no. 11, pp. 1960–1965, 2016.
- Y. Enokido, R. Hashimoto, T. Kitamura, K. Suzuki, K. K. Choi, and Y. Kitamoto, “High-Throughput Screening Method for Thin-Film $R_2Fe_{14}B$ Magnet,” *IEEE Transactions on Magnetics*, vol. 56, no. 4, Apr. 2020.
- Y. Enokido, A. Koda, Y. Umeda, D. Tanaka, and Y. Kitamoto, “Effect of grain-boundary phases in Y- and Ce-substituted $R_2Fe_{14}B$ sintered magnets,” *Journal of Magnetism and Magnetic Materials*, vol. 517, pp. 1–6, Jan. 2021.
- Y. Enokido, F. Baba, Y. Kitamoto, “Magnetic Properties and Particle Flowability of Neodymium Magnetic Granules”, *Materials Transactions*, submitted.

International Conferences

- Y. Enokido, Challenges on the development of rare-earth less and free magnets, Materials Science and Technology 2014 (MS&T14), October 12-16, 2014, Pittsburgh, Pennsylvania, USA, [Oral]
- Y. Enokido, Y. Nagamine, M. Miwa, Y. Fujikawa, C. Moriyoshi, Y. Kuroiwa, Heavy rare earth free neodymium magnets for automobile, The 24th International Workshop on Rare-Earth and Future Permanent Magnets and Their Applications (REPM 16), August 28-September 01, 2016, Darmstadt, Germany, [Oral]

- R. Hashimoto, T. Sato, Y. Umeda, K. Suzuki, Y. Enokido, T. Taniyama, Effect of distortion on magnetic properties of Nd-Fe-B thin film magnets on $BaTiO_3$, JSPM International Conference on Powder and Powder Metallurgy (JSPMI 2017), November 06-09, 2017, Kyoto, Japan, [Oral]
- K. Suzuki, R. Hashimoto, D. Tanaka, Y. Enokido, K. K. Choi, Fabrication and magnetic properties of (Nd,Y)-Fe-B layered thin film magnets, the 2018 Rare Earth Permanent Magnets and Advanced Magnetic Materials and Their Applications (REPM 2018), August 26-30, 2018, Beijing, China, [Oral]
- Y. Enokido, A. Koda, Y. Umeda, D. Tanaka, Y. Kitamoto, Magnetic Properties of $R_2Fe_{14}B$ Sintered Magnets Substituted 50% of Nd with Y and Ce, The 2020 Magnetism and Magnetic Materials Conference (MMM 2020), November 02-09, Virtual Conference, [Oral]

Domestic Conferences

- 榎戸 靖, Dy 削減磁石および希土類削減磁石に関する研究, 第 148 回電子セラミック・プロセス研究会 秋季講演会, 2014 年 10 月 08 日, 横浜, 神奈川, [Oral]
- 榎戸 靖, 希少希土類元素削減磁石, 日本セラミックス協会 2015 年年会, 2015 年 03 月 18 日, 岡山, [Oral]
- 榎戸 靖, 三輪将史, 岩佐拓郎, 石山保, 藤川佳則, 田中美知, 自動車向け Dy フリー NdFeB 焼結磁石, 電気学会マグネティックス研究会, 2015 年 12 月 01 日, 芝浦, 東京 [Oral]
- 榎戸 靖, 三輪将史, 岩佐拓郎, 石山保, 藤川佳則, 重希土類元素フリーNdFeB 焼結磁石の開発, The 23rd ESICMM Seminar, 2015 年 12 月 16 日, つくば, [Oral]

- 橋本龍司、鈴木健一、榎戸靖、崔京九, Fabrication and magnetic properties of (Nd,Y)-Fe-B layered thin film magnets, 第 40 回 日本磁気学会学術講演会, 2016 年 09 月 05 日, 金沢, [Oral]
- 榎戸 靖, 三輪 将史, 永峰佑起, 藤川 佳則, HREE-free NdFeB 焼結磁石, 未踏科学技術協会 磁性材料研究会 21 希土類磁石とその応用探究分科会 第 4 回シンポジウム, 2017 年 01 月 10 日, 新橋, 東京, [Oral]

Patents

5188674, 4506973, 4057561, 4282013, 4057562, 4057563, 4282015, 4282017, 4282025, 4666145, 4282016, 3914557, 4539288, 4543940, 4753024, 4609644, 4561432, 4636240, 4662046, 4506976, 5000882, 4407834, 4687895, 5141868, 5141869, 5464289, 6361089, 6330254, 6269279, 6278192, 6380738, 6424664

Awards and other achievements

- Richard M. Fulrath Award, 2014, American Ceramic Society
- 粉末冶金協会 平成 30 年度 論文賞, 2019 年 06 月 04 日.